Hans Borge

Fault controlled pressure modelling in sedimentary basins

A thesis presented for the degree of
Doktor Ingeniør of the
Norwegian University of Science and Technology
Department of Mathematical Sciences

February 2000

Preface

This dr.ing. thesis is a part of the research project Secondary Migration in Faults and Fractures (SMIFF) which is a joint study by Institute for Energy Technology (IFE), Norwegian Geotechnical Institute (NGI) and SINTEF Petroleum Research. SMIFF is sponsored by the Research Council of Norway (NFR) and the following eight oil companies:

- A/S Norske Shell
- BP Amoco Norge AS
- Elf Petroleum Norge A/S
- Mobil Exploration Norway Inc.
- Norsk Agip
- Norsk Hydro ASA
- Norske Conoco A/S
- Statoil

Associate Professor Harald Hanche-Olsen at the mathematical department at the Norwegian University of Science and Technology (NTNU) has been the supervisor for this thesis. I would like to thank Øyvind Sylta (SINTEF Petroleum Research) for initiating this work and his considerable contributions. Without his help, scientific advises, inspiration and technical support it would have been impossible to carry out the work presented. In addition, I want to address a few words of thanks to the people listed below for providing good ideas, data and constructive comments that have improved the quality of this thesis.

Per Arne Bjørkum (Statoil)
Gunnar E Fladmark (Norsk Hydro ASA)
Martin Hamborg (SINTEF Petroleum Research)
John Ivar Haugland (Geoprobe Technology)
Stephen Lippard (NTNU)
Philip Ringrose (Statoil)
Ulrich Ritter (SINTEF Petroleum Research)
Hanneke Verweij (University of Utrecht)
Eirik Vik (Statoil)
Olav Walderhaug (Statoil)
Kjell Øygard (BP Amoco Norge AS)

Thanks to my family for their great support and patience.

Summary

The starting point for this Dr. Ing. thesis was the requirement for models describing basin scale overpressure for use in basin modelling studies. It is necessary to identify, understand and describe both the generating mechanisms and the fluid flow in sedimentary basins in order to meet this requirement.

All of the models developed are based upon a study area consisting of fault bounded pressure compartments. A reservoir simulator has applied a lateral cross fault transmissibility model and by defining the overpressure history in some of the pressure compartments it has been possible to model the overpressure through geological time. A simpler model estimating the present day overpressure distribution based upon the same fault transmissibility model is developed. This model is able to provide a snapshot of the main present day pressure trends. This model has further been developed to a full pseudo 3D-pressure simulator including generation and dissipation of pressure through time. Due to the quantification of generation and dissipation of overpressure it is possible to model hydraulic fracturing and leakage through the overlying seals. In addition to the models describing the overpressure, an algorithm that converts the pressure compartments into a quadrangle grid system is developed.

The main part of the work in this thesis deals with quantifying basin scale generation and dissipation of overpressure. Different models are developed based upon the available literature and knowledge achieved during this work. All the models used are thoroughly described. The pressure simulator PRESSIM is developed in order to test, improve and reject different models. Several simulations of the overpressure history in the North Viking Graben and the Haltenbanken area offshore Norway are presented. The modelled overpressures are calibrated to the observed pressures revealed by exploration wells. In general, the results are very satisfactory due to relatively small deviations between the modelled and observed overpressures. The simulations provide an increased knowledge of the mechanisms generating and dissipating the overpressure and form a good basis for discussing the nature of the overpressure. In addition, the results suggest which mechanisms are the most important in the different parts of the basin. The pressure simulator PRESSIM can be used to test and verify alternative pressure generation models and flow descriptions in a basin. It is possible to model the position and timing of the hydraulic fracturing because the pressure simulations are based upon a water budget for each pressure compartment.

Contents

1. Introduction 5
2. 3D modelling of fault bounded pressure compartments in the North Viking Graben 10
3. Stationary overpressure distribution 37
3.1 Application to a simple test system 40
3.2 Application to the North Viking Graben 41
4. Modelling in a regular grid 51
4.1 The Rectangular Grid Transmissibility Model (RGTM) 51
4.2 The RGTM-model applied to the NVG 53
5. Fluid dynamics in sedimentary basins 57
5.1 Vertical fluid flow model 60
5.2 Generation of overpressure 70
5.3 A numerical model describing pressure dissipation 84
6. Pressure simulation case studies 87
6.1 Pressure simulation in the North Viking Graben 87
6.2 Pressure simulation in the Haltenbanken area 113
7. Discussion and conclusions 137
Bibliography 146
Appendix A : The SEMI secondary migration program 149
Appendix B : The PRESSIM pressure simulator 150
Appendix C : Estimation of overpressure 151
Appendix D : Mathematical deductions 152
D.1 Effective drainage depths 152
D.2 Estimating shale permeabilities from accumulating efficiencies 154
D.3 Shale compaction and pressure generation 156

1. Introduction

In the search for oil and gas it is very important to increase the understanding of oil and gas migration. Predicting overpressure is one of the biggest challenges facing the oil industry, in particular as exploration moves into deep waters areas (Swarbrick and Schneider, 1999). It is of great importance to quantify the effect of water flow since pressure (potential) controls the hydrocarbon migration together with the buoyancy forces. High overpressure may prevent hydrocarbons from migrating into a prospect and thus create an alternative flow path. Consequently, prospects that initially were considered as promising may show up to be dry and traps that are located in a migration shadow based upon a buoyancy analysis may thus contain hydrocarbons. The definition of a petroleum system often needs a full understanding of the pressure history because preservation of petroleum reserves in traps as well as their migration timing and direction are all influenced by pressure (Swarbrick and Schneider, 1999). The impact from overpressure on prospect appraisal is much less well known than the problem it may cause for safety and well design. (Giles et al., 1997).

It is necessary to pay attention to several features trying to quantify the overpressure on a basin scale. Firstly, it is of vital importance to identify the geological mechanisms and processes that generate overpressure through geological time. Secondly, it is necessary to model the dissipation of the generated overpressure. There exist two conceptual models for abnormal pressures (Neuzil, 1995), a static model which claims that the overpressures are relics preserved by the absence of fluid flow through geological time and a dynamic model suggesting that overpressure is a phenomena where fluid flow plays an important role. By modelling fluid flow on a basin scale through geological time it may be possible to quantify the rate of dissipation and to judge which of the two conceptual models describe the nature of overpressure. In order to run numerical simulations that describe generation and dissipation of overpressure it is necessary to find a simple and realistic three-dimensional representation of the geology. Describing all the geologic details in a basin that influence the flow of formation water is more or less impossible due to the amount of work and lack of available data. Although it is possible to test the impact of lateral flow on the dissipation of the overpressure along a 2D line (e.g. Yardley, 1998) the fluid flow in a sedimentary basin seldom or probably never can be characterised along a line. The pore fluids flow through the entire formations and do not follow certain stringers that can be modelled along a line. Thus a 2D analysis may not provide a sufficient description of the fluid flow to draw conclusions about the prevailing mechanisms generating and dissipating the overpressure in the basin.

Which mechanism or mechanisms may have generated the observed overpressures is highly debated. The most probable geological processes are undercompaction of sediments, diagenesis, hydrocarbon generation, aquathermal expansion and horizontal loading caused by tectonic stresses. Due to the very low compressibility of water very few of the candidates can be eliminated without further investigation. It is not unlikely that two or more of these mechanisms can work in parallel and those different parts of the basin or different basins may have various origins of overpressure. These facts illustrate the importance of describing the geology of the basin as completely as possible and model fluid flow and test the various generating mechanisms through time, which may influence the present day overpressure distribution.

Several papers mainly published during the 80s and early 90s have formed a consensus claiming that compaction disequilibrium is the predominant cause of overpressures in many basins (Mann and Mackenzie, 1990) and (Kooi, 1997). Although compaction disequilibrium intuitively is an obvious candidate for overpressure generation the mechanism may be insufficient to account for close-to lithostatic fluid pressures in formations older than some 100 Ma (Kooi, 1997). Kooi's conclusion is based upon a one-dimensional numerical model using a lower limit of shale permeability ranging from about 10^{-22} m^2 to 10^{-19} m^2 depending on the porosity. He further stresses that if future work shows those shale permeabilities at a basin scale is less than the values discussed, the conclusion may need modification. However, if lateral fluid flow is allowed to take place (suggested by this thesis and by Darby et. al (1996)) the lateral dissipation will reduce the ability for disequilibrium compaction to generate close to lithostatic pressures even more. Mechanical compaction gradually decreases during subsidence because cementation processes reduce the ability for the sediments to compact. This fact disfavours the compaction disequilibrium as the dominating mechanism at the depths where overpressure usually is observed. Hermanrud et al. (1998) show a stronger correlation between temperature and porosity (average core porosity for sands and porosity from density logs for shales) than between effective stress and porosity based upon sands and shales from the Haltenbanken area offshore Norway, and conclude that temperature, and not the effective stress, exerts the main control on porosity reduction. The temperature porosity correlation is not very convincing since the porosity varies about 10 % at certain temperatures. In addition, it is speculative to draw conclusions upon porosity plots since a large number of geological and geochemical processes are able to cause large variations on both basin and reservoir scale. It is thus very difficult to find convincing porosity observations of disequilibrium compaction.

Diagenetic candidates for generating overpressure can be divided into two groups: dehydration and cementation. The most common dehydrative process is smectite to illite transformation in shales. Since the volume of released fluid is small in this process it is

unlikely that smectite dehydration is a primary cause of overpressure but a secondary importance since precipitation of diagenetic minerals decrease the permeability in shales and adjacent reservoirs (Osborne and Swarbrick, 1997). Quartz cementation of sands occurs most intensively at burial depths between 3.5 km and 5 km (Bjørlykke and Høeg, 1997). This fact makes this process a very hot candidate for generating the overpressure since very often overpressure is observed at these depths (Darby et. al, 1996). The quartz cementation consists of three stages: solution, diffusion and precipitation where precipitation of the quartz cement is the rate controlling process (Walderhaug, 1996). This process generates overpressure by squeezing the formation water through reducing the porosity. The increased overpressure will reduce the effective stress and further compaction. This statement promotes the quartz cementation as a process of primary importance rather than one of secondary importance. One of the main objections against quartz cementation as pressure generating mechanism is that mineral precipitation and dissolution could produce abnormal pressuring only if no fluid can enter or escape from the rock at the time these reactions occur. If fluid escapes from the rock in response to cement infilling, then pore pressure would not increase (Osborne and Swarbrick, 1997). The diagenetic community is deeply divided in the question whether cementation and dissolution take place in an open or a closed setting (Osborne and Swarbrick, 1997). In addition overpressure is likely to inhibit quartz cementation where the major source of silica is from pressure solution because when pore pressure increases, effective stress decreases, reducing the stress at grain contacts (Osborne and Swarbrick, 1997). However, as long as precipitation is the rate controlling process the build-up of overpressure should not slow down the process significantly. Since time and temperature control the precipitation of cement quartz cementation is able to generate overpressure during a hiatus and even during a period of up-lift.

Most authors seem to agree that the effect on the overpressure from aquathermal expansion is of minor importance compared to other generating mechanisms (e.g. Hall, 1994, Luo and Vasseur, 1992, Osborne and Swarbrick, 1997). Overpressure usually builds up gradually across a transition zone indicating that reduced permeability retards the fluid escape. The viscosity of brine decreases with increasing temperature and thus the formation water more easily will escape when heated. This fact illustrates the need for an impermeable seal if thermal expansion should be the primary cause of overpressure. An impermeable seal will result in sharp transition zones for the overpressures, which is not the case in most basins containing overpressure.

Hydrocarbon generation is another candidate for pressure generation. If organic matter is present the maturation process take place at more or less all depths but most intensively between 3 km and 5 km. The gas generation and oil cracking, which are the most effective pressure generating parts of the hydrocarbon maturation, are most intense below 3 km.

This is a very favourable depth interval with regard to the observed overpressures. Quantification of these processes is clearly needed for their integration into basin models (Osborne and Swarbrick, 1997).

In addition to the possible mechanisms listed above, undrained lateral stress caused by tectonic activity is a plausible origin for overpressure. This process has definitely a large potential since the horizontal stress increases, in contrast to vertical load, without a corresponding increase in vertical stress. The ratio between increment of pore pressure and the increment of horizontal stress has sometimes been observed to be larger than 1 (Yassir, 1998). Lateral compression has often been suggested as a possible pressure generating mechanism in sedimentary basins, but has been poorly quantified (Bour et al., 1995). Global occurrences of overpressuring show, with a few notable exceptions, a strong relationship between overpressure and present day compressional tectonics (Yassir, 1998). This relationship may reflect that sedimentary basins tend to form in compressional tectonics rather than the occurrences of overpressure are caused by the tectonic compression. The generation of overpressure does not depend upon lateral stress since several basins containing overpressure without lateral compression are observed (e.g. the North Sea rift basins).

In many papers discussing the causes of overpressure it seems to be a common understanding that mechanisms retarded by increasing pressure (e.g. compaction, hydrocarbon generation) are disfavoured as primary causes. This is not an obvious conclusion. Lateral flow seems to affect the basinwide distribution of overpressure (Borge and Sylta, 1998, Bredehoeft et. al, 1988, Darby et. al, 1996) which indicates that the nature of the overpressures is dynamic. This means that the overpressures slowly dissipate through time and that the generating mechanism or mechanisms keep pace with the dissipation. The balance between generation and dissipation ensures that the generating mechanisms are able to supply overpressure through geological time. Pressure generating mechanisms that are not retarded by increasing overpressure or by another process may consume all their potential in a very short time. If the overpressure is a dynamic phenomenon large overpressures are drained either by hydraulic leakage and/or lateral flow. Thus some mechanisms seem to be very efficient because they have no competitors. However, such pressure generation mechanisms are only able to influence the pressure in a short period of time.

It is necessary to quantify both the pressure generation and the fluid flow in order to be able to model the pressure distribution in a sedimentary basin. Lateral flow and dissipation of overpressure on a basin scale seem to be much less discussed than the plausible mechanisms generating the overpressure. When overpressures develop in high permeable sandstone located between low permeable shale sequences, faults play an important role.

Usually faults are partly or completely sealing and thus form barriers to fluid flow (Knipe, 1992, Mann and Mackenzie, 1990, Smith, 1966). In order to model the development of overpressure it is necessary to suggest models for flow across faults. The impact of the faults on regional overpressure seems to be considerable so that the pattern of faults revealed by seismic investigation will create a base for the overpressure distribution in a region. Hydraulic fracturing and lateral connectivity usually create a regional sink in a basin. It is very important to model the correct timing of hydraulic leakage because the overpressure probably is a dynamic phenomenon and it affects the secondary migration of oil and gas significantly.

The paper “Modelling of pressure compartments in the North Viking Graben” published in the special issue “Pressure compartments, seals and systems” of Energy, Exploration & Exploitation, is presented in chapter 2 and forms a starting point for this Dr. Ing. thesis by suggesting a simple model for lateral flow. This paper was given as an oral presentation at the EAGE conference in Glasgow, 1995. Based upon the results in section 6.2, two contributions at international conferences are made: The oral presentation “Overpressure – a static or dynamic phenomenon?” was given at the EAGE conference in Helsinki, 1999. The poster “Quantification of mechanisms for generating overpressure in the Haltenbanken region” was presented at the IAMG conference in Trondheim, 1999.

2. 3D modelling of fault bounded pressure compartments in the North Viking Graben

Hans Borge and Øyvind Sylta
IKU Petroleum Research
N-7034 TRONDHEIM, NORWAY

Abstract

The work presented in this paper involves modelling of the overpressure distribution in Jurassic reservoir and carrier rocks in the North Viking Graben. The main concept used in this study is that faults may form low-permeability barriers to fluid flow in compacting basins, and may thus influence overpressure distribution. The mapped faults in the study area are linked together so that they divide the area into 225 compartments. A model based on Darcy's law and information about offset and burial depth describes the flow conditions across the faults and between the compartments. This model describes a regional fault permeability architecture. A commercial reservoir simulator is used to calculate the fluid flow and the pressure development in all the compartments. The model was calibrated to pressures measured in 16 released exploration wells. The best match to these wells was obtained with a mean deviation of 9.5 bars and a standard deviation of 18.5 bars between the observed and predicted overpressures for the Brent Group. The results from this pressure modelling can be used to simulate secondary migration of oil and gas.

Introduction

The main idea behind the model developed to calculate a realistic present day pressure map is that faults form barriers to fluid flow. The Middle Jurassic Brent Group in the North Viking Graben is divided into pressure compartments bounded by the mapped faults. Faults can cause big lateral pressure differences in a reservoir (Mann & Mackenzie, 1990), and thus constitute a lateral seal for the pressure compartments. Distinct pressure-depth gradients in the pre-Cretaceous sandstones in the UK Central Graben suggest compartmentalisation and hydraulic separation of the sandstone into pressure cells (Darby, Haszeldine & Couples, 1996). Over- and underlying sealing layers may thus cause vertical boundaries for the pressure compartments. Figure 1 illustrates the concept of pressure compartments. In this study, no geometrical reconstruction of faults is carried out other than linking the mapped faults together in order to form the pressure compartments. According to this model all changes in overpressure occur across the faults. What appear to be fluid compartments in a subsurface basin can result from dynamic movement in which

almost all of the changes in fluid potential occur associated with zones of low permeability (Bredehoeft, Belitz & Sharp-Hansen, 1992). It is assumed that fluids inside a pressure cell are in free hydraulic communication. The pressure is treated as transient and the compartments as dynamic over time.

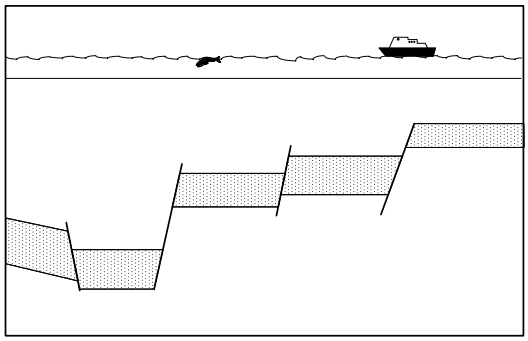

Figure 1 Schematic outline of pressure cells

The connectivities between the neighbouring compartments are calculated based upon data provided by seismic such as thickness of reservoir, depth to fault, length of fault and size of fault offset/overlap. A transmissibility model for the faults is inferred. The ability for water to flow between connected cells is described only by the transmissibility. This is a quite useful approach because most commercial reservoir and basin simulators have an arbitrary connection device, which means that it is possible to connect any two grid blocks. The data provided by seismic are treated as variables, while the rest of the parameters in the transmissibility model have the same values all over the study area. In this way a regional model for fault based permeability architecture is introduced. If the parameters were allowed to vary freely from fault to fault, the calibration would probably become too large. The main task is to model fault- or fault zone- permeability when evaluating sealing or preferential paths for fluid flow migration. Previous work on this topic is very scarce in the literature and exists only at the qualitative level (Antonellini & Aydin, 1994).

The pressure compartments were coded into the SimBest II reservoir simulator from SSI and connected according to the inferred model. Other simulators, e.g. Eclipse, may also be used. “Wells” at the boundary of the study area control the development of overpressure. Overpressure development in a sedimentary basin is directly related to the rate of fluid escape from the sediments (Yu & Lerche, 1996). However, the mechanism or mechanisms generating the overpressure is highly debated (Osborne & Swarbrick, 1997), (Walderhaug, 1996) and (Kooi, 1997). The modelling presented in this paper does not concentrate on the generation of overpressure, but the lateral dissipation, which is assumed to be governed by the partly sealing faults.

It is assumed that the fluid flow modelled in this study reflects the contribution to the overpressure from undercompaction of sediments during burial subsidence. Other factors such as fluid thermal expansion, dewatering of clays and hydrocarbon generation are considered less important (Yu & Lerche, 1996), and are not included in the simulations.

The study area, located between 2° and 4° E and 61° and 62° N (Figure 2), which is about 40 km west of the Sognefjord, represents an area of about 20000 km². It includes quadrants 34 and 35 and the northern parts of quadrants 30 and 31 on the Norwegian continental shelf. This area contains several oil and gas fields, e.g. Visund, Huldra, Agat, Veslefrikk and the northern parts of the Troll field.

The resulting pressure maps can be used as input to secondary migration simulations (Sylta, 1996). Hydrodynamic pressure (potential) differences across faults may increase or decrease the oil and gas leakage across the faults. It is therefore of crucial importance to the success of hydrocarbon secondary migration studies that the results from the pressure modelling are used. Otherwise, the fault leakage model becomes too unconstrained and the predictive capability of the model may be non-existent.

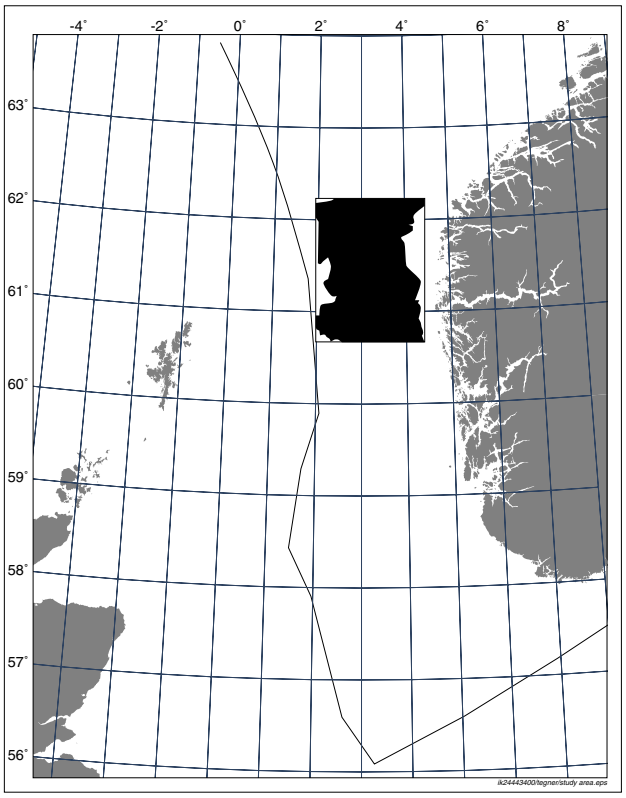

Figure 2 The study area

Pressure cells

The compartmentalisation of the study area was carried out by using the mapped faults shown in Figure 3. In order to create pressure compartments, some of the faults were tied together by extending them beyond the seismically resolved tip to the nearest fault. The results of this process can be seen by comparing Figure 11 with Figure 3. Based upon this assumption, the study area is divided into compartments bounded by the blocky lines shown in Figure 4. This could be a realistic way to consider the compartmentalisation because even faults which are too small to be seen on seismic can contribute to the compartmentalisation of a block (Gauthier & Lake, 1993). Extending the faults beyond the seismic resolution increases the connectivity of the fault pattern (Pickering et al., 1997). The fault compartment interpretation involves making closed compartments by connecting fault traces in a geologically reasonable manner. We did not remove any fault segments. Faults that are not part of closed polygons automatically lie inside the compartments and therefore are not used in the pressure modelling.

It has long been known that fault systems have a degree of self-similarity across a wide range of scales (Yielding, Walsh & Watterson, 1992; Wen & Sinding-Larsen, 1994; Gauthier & Lake, 1993). Considerable progress has been made in recent years in methods of predicting sub-seismic fault populations. Prediction of realistic spatial distributions of sub-seismic faults is much less certain (Heath, Walsh & Watterson, 1994). However, extensional fractures are non-fractal and frequently terminate against fractures of the same family (Loosveld & Franssen, 1992). These factors may justify the subjective fault connections made in this study rather than developing a model or algorithm connecting faults based upon fractal or self-similar criteria.

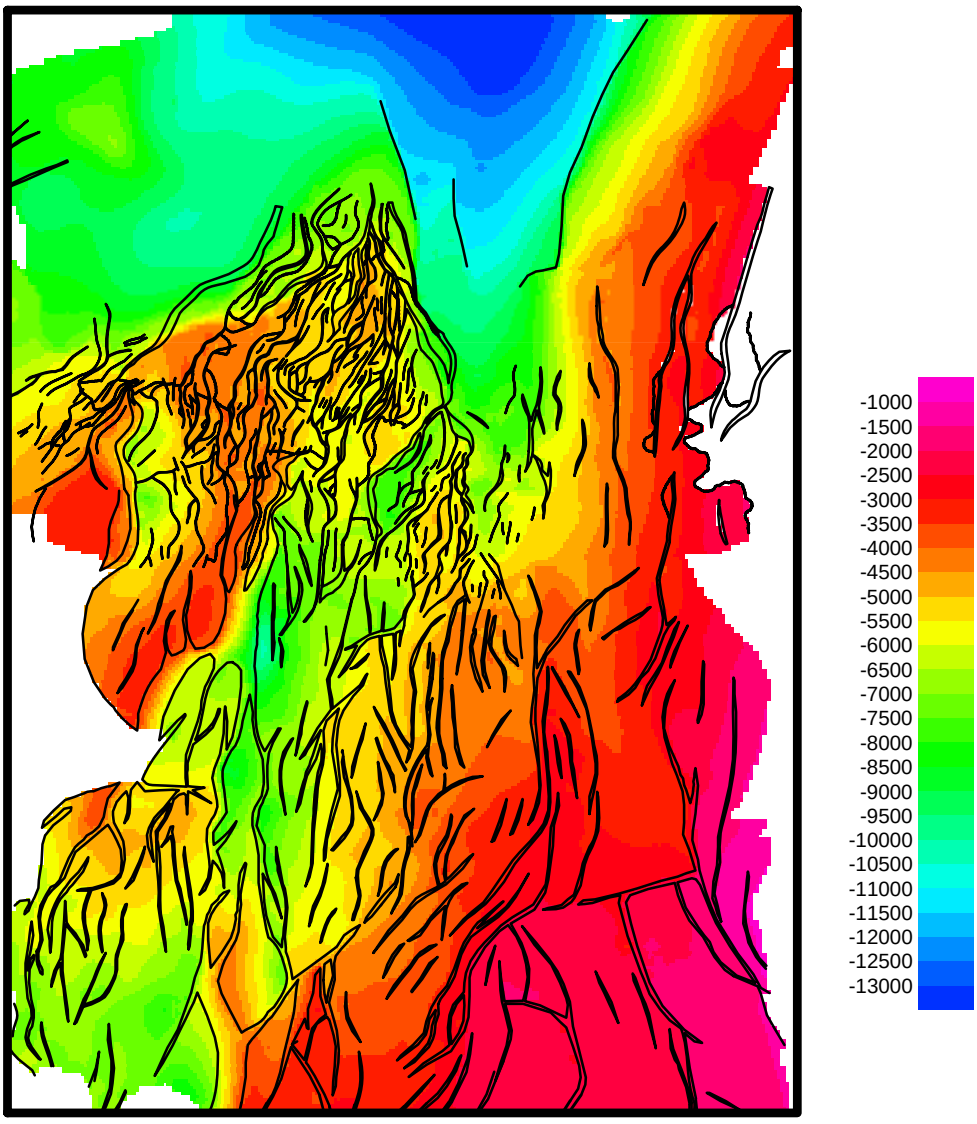

Figure 3 *Present day depth* (m) *map of Top Brent Group with interpreted faults mapped from seismic data*

Figure 4 *The study area divided into pressure compartments. Pixels between the compartments without fill are defined as inside of faults and are not part of any pressure compartments. Each compartment is shown in one greyscale value. The actual value is arbitrary, and does not indicate pressure or overpressure.*

Fault permeability characterisation

A cataclastic fault may result in either a permeability increase or decrease (Knipe 1992, Loosveld & Franssen, 1992), but the latter is more common (Loosveld & Franssen, 1992). Granulation and cataclasis, associated with faulting in porous sandstone, cause the porosity to drop approximately one order of magnitude in a deformation band and almost to zero adjacent to a slip plane; permeability drops one to four orders of magnitude normal to a deformation band and more than seven orders of magnitude perpendicular to a slip plane (Antonellini & Aydin, 1995). In addition to this, the high overpressures in the deep and intermediate parts of the basin indicate that the faults act as seals. During periods of active movement, the faults may have gone through short transient periods when the faults acted as fluid migration pathways (Knipe, 1992). Possible non-sealing periods like this are unlikely to affect the lateral fluid flow on a geologic time scale. The pressure build-up in this area took place after the faults were active, so that it is natural to assume that all the faults to a certain extent are sealing.

In order to deduce a model for fluid flow, a fault is considered as a low permeable block located between two reservoirs as illustrated in Figure 5. The transmissibility, T, which is the ability of water to flow through a porous block, is given in Equation 1. Faults are considered to be low-permeable blocks with a specific thickness. Therefore we do not have to determine whether the faults are surrounded by damage zones or deformed zones in the model. Irrespective of the structures forming the faults, the impact on fluid flow can be accounted for by this block.

$$T = \frac{\Delta l \, H \, K}{b} \qquad (1)$$

Equation 1 forms the basis for a "Fault Transmissibility Model". It is assumed that one of the most important properties of faults is whether they have an offset or an overlap. The model introduced by Equation 2 and illustrated in Figure 7 accounts for fault throw effects. It is desirable that the transmissibility should be more or less proportional to the contact area when overlaps are modelled, because sand-sand contacts usually are "non-sealing" (Nybakken, 1991). Thus, in the case of decreasing overlap, the transmissibility decreases linearly to $p\%$ of the original transmissibility given in Equation 1. Faults in the Brent province (located only few km west of the study area) with throws greater than the reservoir thickness have a better than 90% probability of sealing (Knott, 1993). This observation suggests a relatively low value of the parameter p and justifies large differences in transmissibility between overlapping faults and faults with an offset. It is further assumed that the transmissibility function follows an exponential curve in the case of increasing offset. Even if the fault throw is small $(\theta \approx -H)$, the permeability is

considerably decreased by the fault block. The argument is that cataclasis and shale smearing will reduce the permeability even at small fault throws. If there is no throw $(\theta = -H)$, which means that the reservoirs overlap completely, the model will simplify to Equation 1.

$$T(\theta) = \frac{\Delta l\, K}{b}\left[(p-1)\theta + pH\right] \qquad \theta < 0$$

$$T(\theta) = \Delta l\; pH\, e^{-B\theta}\, \frac{K}{\sqrt{b^2 + \theta^2}} \qquad \theta > 0 \tag{2}$$

Numerical simulations of K_{eff} / K (the ratio between effective horizontal permeability and the permeability in a shale-free sandstone matrix) vs. fault density have shown that the effective permeability decreases linearly (or very close to linearly for the 3D models) with increasing fault density (Heath, Walsh & Watterson, 1994). This observation may support the linear part of the transmissibility curve in Figure 7. If the overlap variable $\theta \in (-H,0)$ is comparable to or proportional to the fault density, the statement above supports the assumptions that $T(\theta)/T$ decreases linearly with increasing offset, where T and $T(\theta)$ are taken from Equation 1 and 2 respectively. In addition, fault seal data from the northern North Sea show that increasing the maximum fault throw compared to the reservoir interval thickness increases the fault seal probability (Knott, 1993). The regional fault seal model given in Equation 2 is a simplification intended to describe the regional lateral fluid flow behaviour. The model is not designed for investigating individual faults in detail for prospect analysis.

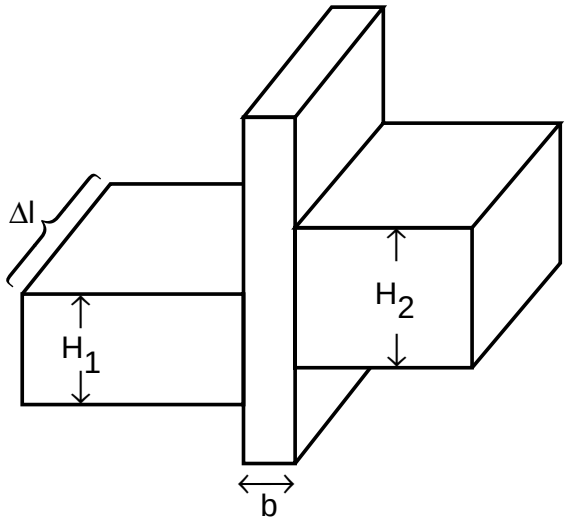

Figure 5 Schematic outline of a fault

Table 1 Nomenclature

K	:	Permeability inside the fault block
b	:	Width of fault block
Δl	:	Length of fault block
T	:	Transmissibility
H	:	Thickness of reservoir, $H = \min\{H_1, H_2\}$
ϕ	:	Porosity
D	:	Water-depth
z	:	Depth to fault
δ_{sh}	:	Rate of change in permeability (log) versus porosity (log) in log (permeability) - log (porosity) relationship for shallow depths, i.e. $\phi > \phi_b$.
δ_{de}	:	Rate of change in permeability (log) versus porosity (log) in log (permeability) - log (porosity) relationship for deep parts, i.e. $\phi < \phi_b$.
K_b	:	Permeability where $K - \phi$ curve changes between deep and shallow relationships.
ϕ_b	:	Porosity where $K - \phi$ curve changes between deep and shallow relationships.
c	:	Rate of change in porosity versus depth
ϕ_0	:	Porosity at seabed
θ	:	Offset/overlap (see Figure 6)
p	:	Percent remaining fault-transmissibility when both the overlap and the offset is zero.
B	:	Parameter controlling the exponential decrease of the transmissibility function.

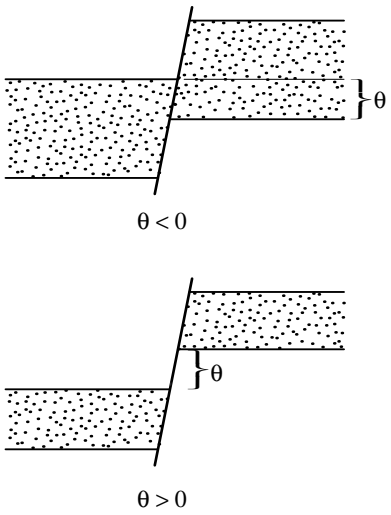

Figure 6 *Fault with overlap ($\theta < 0$, above) and fault with offset ($\theta > 0$, below).*

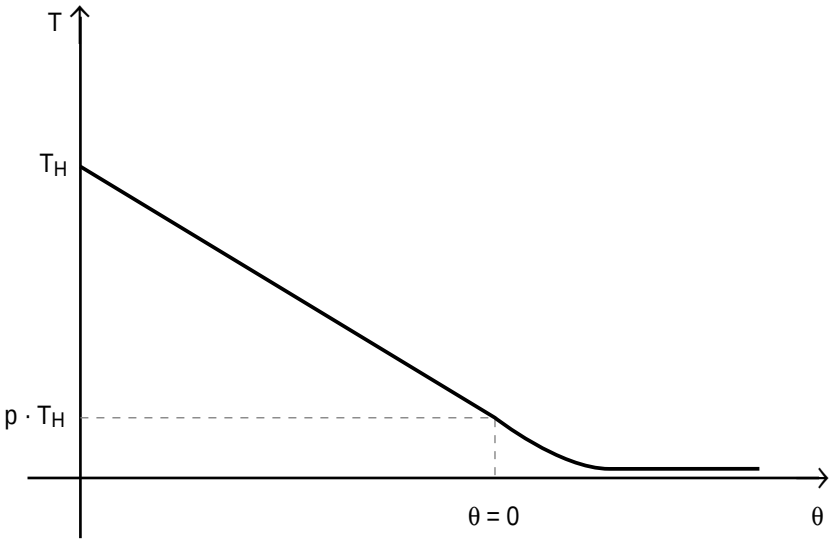

Figure 7 *Transmissibility function - the "Fault model"*

The permeability of clastic rocks is often treated as dependent on porosity, which again is considered to be a function of depth (Sclater & Christie, 1980). In order to include these properties and complete the fault transmissibility model, the relationships between permeability and porosity presented in Equation 3 and illustrated in Figure 8 are used. Note

that by using this permeability model it is possible to differentiate the relationship between permeability and porosity in the deep and shallow areas in the basin. This introduces a great flexibility to the calibration work and is supported by Loosveld & Franssen, 1992.

$$K = K_b\left(\frac{\phi}{\phi_b}\right)^{\delta_{de}} \quad \phi < \phi_b$$

$$K = K_b\left(\frac{\phi}{\phi_b}\right)^{\delta_{sh}} \quad \phi > \phi_b \qquad (3)$$

The porosity is given by Equation 4 which is the most usual porosity function used in numerical basin models (Wangen, 1992). This porosity model is deduced for isostatic burial history models and it provide a useful permeability-depth relationship for the fault blocks.

$$\phi = \phi_0 e^{-c(WD-z)} \qquad (4)$$

The variables and parameters in Equations 1, 2, 3 and 4 are explained in Table 1. The parameters b, p, B, ϕ_b, K_b, δ_{de}, δ_{sh}, ϕ_0 and c have to be determined during the calibration of the model although reasonable starting values can be obtained for b, ϕ_b, ϕ_0 and c by geological reasoning. All the parameters are given the same value over the entire study area. Properties like width of fault, thickness of reservoir, water depth, depth to fault and offset/overlap differentiate the transmissibility values between the faults. Transmissibilities between neighbouring compartments are calculated by using Equations 2, 3 and 4 on a fault segment to fault segment (grid node) basis and adding the contributions along the blocky lines in Figure 4. The grid resolution is 500 m.

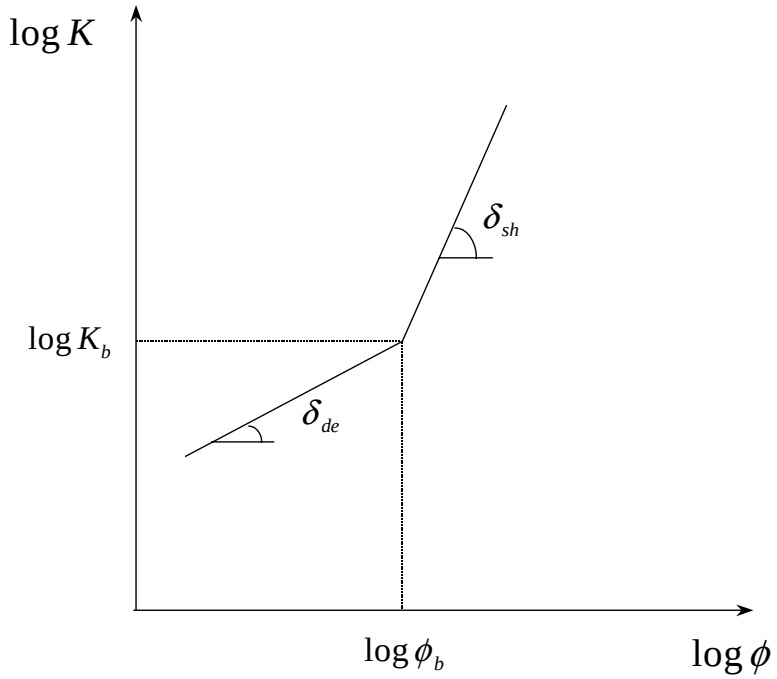

Figure 8 Permeability vs. Porosity

A simplification used in this study is to keep the geometry, and thus the sealing properties, constant through time. However, this simplification is not as limiting as it might seem. There are three main categories of seals: collapse seals, cement seals and juxtaposition seals (Knipe, 1992). The collapse and juxtaposition seals are more or less constant throughout the time we are modelling the pressure, since the faults have not been active since early Cretaceous. The cement seals are more difficult to handle in this model. The idea is that the model during the calibration process will provide a mean value of the sealing effect through time, which is sufficient to describe the sealing effects for the purpose of basin-scale pressure modelling. In addition, the faults in the study area are extensional fractures developed in the Jurassic and they have not been active since early Cretaceous.

The simulations

All the pressure compartments are represented in the SimBest II simulator from SSI by the present day depth to the top Brent Group and the thicknesses of the Brent Group, Dunlin Group and Statfjord Formation. In addition, thick sequences of shale/seal were added both above and below these reservoir units. The reservoirs in all the neighbouring compartments were then set up with the fault transmissibility model, by use of an arbitrary cell

connection device available in the simulator. This situation is illustrated in Figure 9. In this way a pseudo 3D model for fluid flow is achieved. A similar pseudo 3D model including more geological units can be found in Bredehoeft et al (1992).

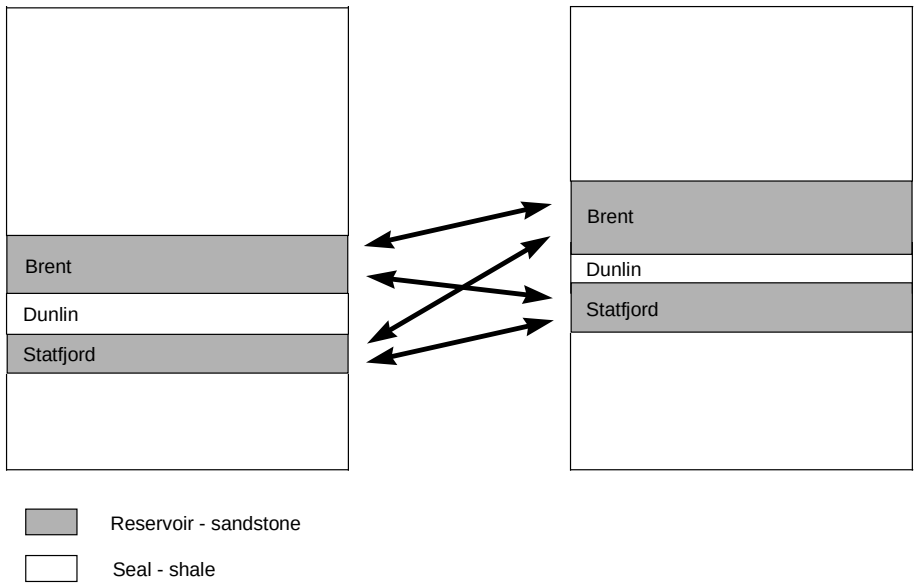

Figure 9 *Possible connections specified between two neighbouring pressure cells. The arrows show flow connections using fault model.*

In order to make use of a 3D reservoir simulator technology, which already exists, we transform the problem from one in which the potential difference between the basin and the flank is caused by an increase in the overpressures in the basin (e.g. Ungerer et al. 1990), to one in which the potential difference is caused by a lowering of pressures at the flank. Instead of building up an overpressure, this system is initiated with a large overpressure of about 400 BAR over the entire study area. Two pressure compartments on the flank, one in the Visund area and one in the 34/4 block (see Figure 11) are defined as boundary compartments. In each boundary compartment, a “production well” has been defined in order to create differences in the overpressure. These differences are modelled to be the driving forces in the system and the overpressure histories in the boundary compartments are forced to follow the curves outlined in Figure 10, upper part. The pressure curve for the flank in Figure 10 upper part represents hydrostatic pressure. In order to find the real modelled overpressure this curve must be subtracted from the other curves as illustrated in the lower part of Figure 10.

The present day overpressure in the boundary cells is known from wells located within them. The boundary cell pressure histories (the curves in Figure 10), are of course not known. These curves were constructed in order to give an acceptable match to the present day overpressure in the calibration wells presented in Table 2. The large and rapid drop in overpressure on the flank and in the Visund area in Figure 10 represents a large increase in the difference in overpressure between the deep and shallow parts of the basin caused by a rapid pressure release on the eastern flank. The best matched overpressure presented in Tables 2 and 3 occurred only about 1.3 Myr after this marked drop. Thus this drop may well correspond to a large pressure release caused by a rapid uplift of the flank due to the disappearance of the last ice-age. Without introducing this pressure drop it was not possible to match the model. Groundwater is drained laterally through the Brent and Statfjord layers due to the differences in overpressure shown in Figure 10. By changing the parameters in the transmissibility model the flow rate is adjusted until the modelled overpressures match the observed overpressures in the released exploration wells in the study area.

In order to achieve the best match it was necessary to increase the vertical permeability in the seal shown in Figure 9. The drained water in the Brent Group and Statfjord Formation is thus partly replaced by vertical flow from the thick overlying and underlying sequences. The model thus incorporates vertical fluid flow into the sands expelled from over- and underlying shales. These observations show that both vertical and lateral fluid flow affect the present day overpressure distribution in the basin.

The SimBest II reservoir simulator uses a finite difference formulation of the conservation of mass and Darcy law to describe the water flow. This results in a system of coupled algebraic equations. The simulator treats the pressures fully implicit by using the proprietary SSI matrix solver ESPIDO which SSI claims is a fast, robust and powerful method.

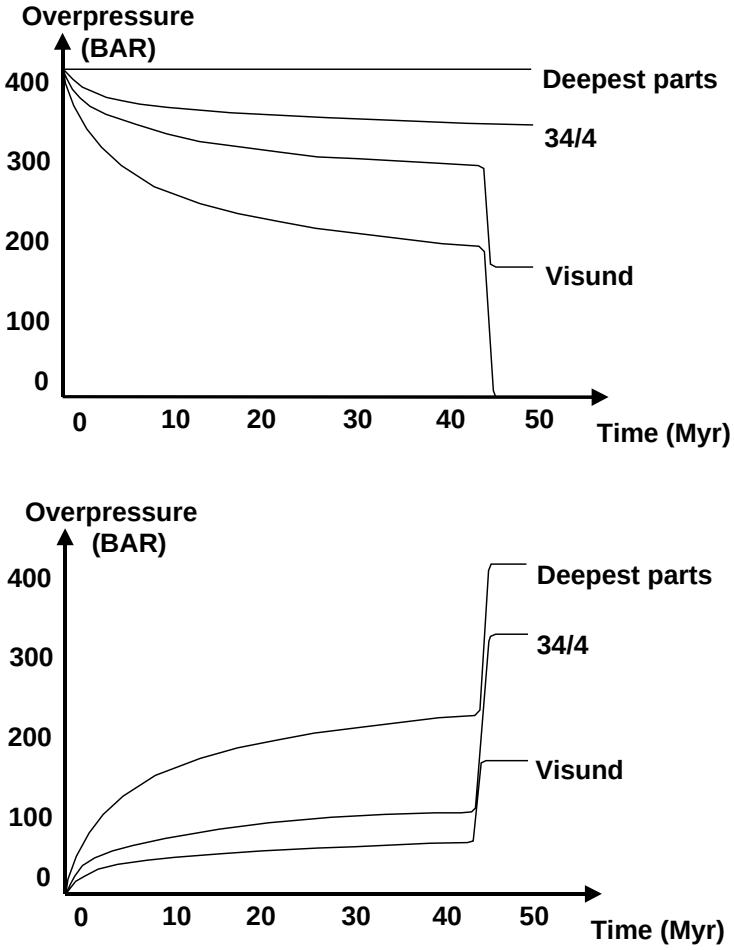

Figure 10 *Modelled overpressure histories (upper part) and the actual modelled overpressures (lower part) in the boundary cells. The dynamic basin overpressure histories (lower) are transformed into a static basin formulation (upper) in order to make use of existing pressure simulators. See Figure 12 for location of these cells.*

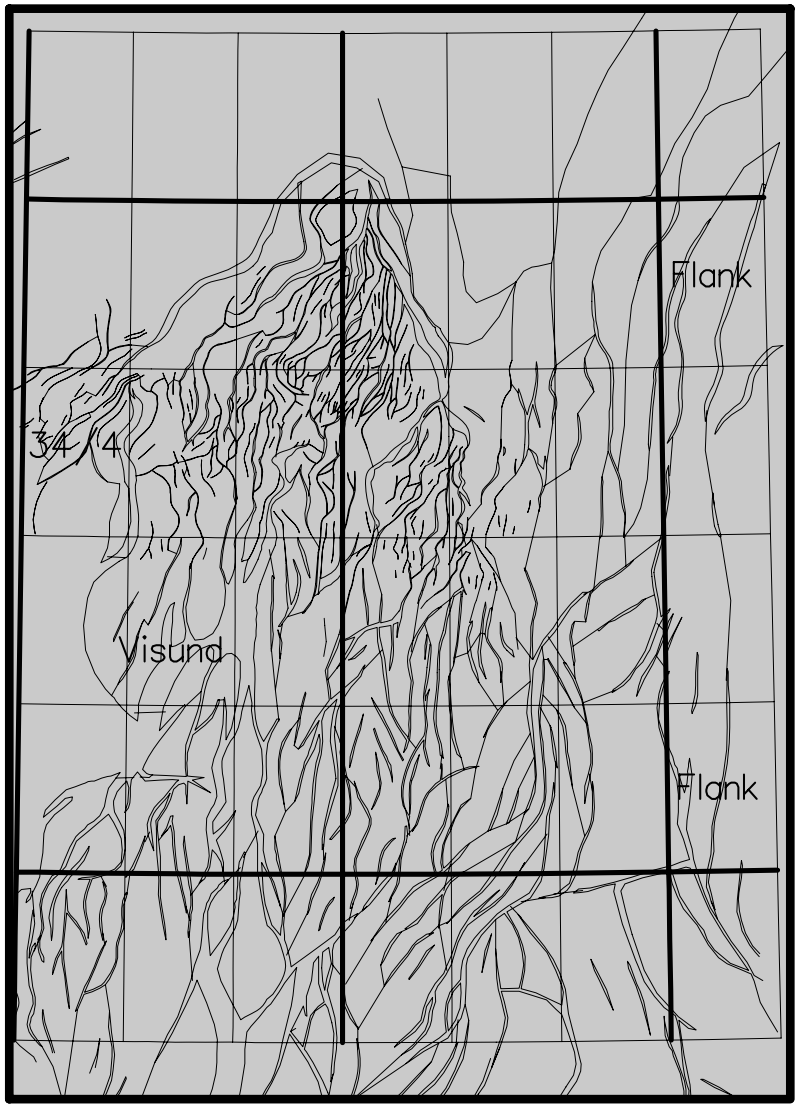

Figure 11 The locations of the boundary cells and mapped faults linked together

Data input

The pressure modelling, as performed in this study, requires three types of data: A present-day depth-converted map of the top of the reservoir, the present-day thickness of the reservoir and the mapped outline of pressure compartments. The Top Brent Group depth map, including outlined pressure compartments of the study area, is shown in Figure 4. Further details about the area can be found in Sylta, 1993.

A two-way time (TWT) map (grid) was provided. This TWT grid was depth-converted using a simple time-depth lookup curve. Three isopachs from the seismic mapping were constructed. These were the Brent Group, the Dunlin Group and the Statfjord Formation. The TWT isopachs were converted to depth using a constant interval velocity of 3500 m, which is considered to be of sufficient accuracy for the work performed in this study.

The data discussed above are the only basic input data required for the modelling. Other input data are assumed by the modellers, e.g. shale permeabilities etc. The simplicity of the required input data is one of the strengths of the pressure modelling performed in this study: It is desirable to only require data that geologists are able to provide.

The pressure data used for calibration in the study were taken from the Well Data Summary Sheets published by the Norwegian Petroleum Directorate (NPD). Based on geological tops and pressure measurements from RFT-tests, the groups and formations were identified and an upper and lower limit for the overpressures calculated.

Results

During a comprehensive calibration process the parameters given in Table 2 appeared to give the best match. The overpressure in the study area is plotted in Figure 13 while the deviations in overpressure are given in Table 3. The intervals of measured overpressure in Table 3 are calculated as an upper and lower deviation from hydrostatic pressure measured by RFT tests.

The results incorporate all the known main trends of the overpressure in the study area today. The models predict nearly hydrostatic conditions on the eastern flank and very high overpressure in the North Viking Graben which is located in the lower left corner of the study area. Moving eastwards from the North Viking Graben area the overpressure gradually decreases towards hydrostatic. Moving eastwards from the Visund field, located in the middle of block 34/8, it is necessary to cross a basin with high overpressure before arriving at the flank. With some exceptions, the overpressure increases with increasing

depth. This is in good accordance with the observations made in the UK Central Graben by Darby, Haszeldine & Couples, 1996.

The average fault transmissibilities between the connected pressure compartments are plotted in Figure 14. Note the consistency between the transmissibility values in Figure 14 and the modelled present day overpressure in Figure 13. Low transmissibility between two neighbour cells tends to give a large difference in overpressure while high transmissibility values may allow the overpressure to stay more or less equal across the faults. Red colours on the eastern flank in Figure 14 indicates high connectivity between the pressure compartments. Figure 14 indicate lower transmissibilities along a diagonal from the lower left corner to the upper right corner. In Figure 13 the corresponding areas are clearly overpressured. The faults near the Visund field (see Figure 11 for the location) have relatively high transmissibility values. According to the model, formation water is allowed to drain laterally in this area resulting in an intermediate overpressure as indicated by Figure 13. Conclusively, the correspondence between the connectivity and the pressure compartments suggested by the model presented corresponds well to the resulting overpressure.

Table 2 Best match parameter values.

b	p	B	ϕ_b	K_b	δ_{de}	δ_{sh}	ϕ_0	c
20	0.05	0.0069	0.1	$1.55 \cdot 10^{-5}$	1	10	0.45	0.0004

Table 3 Deviation table, Brent Group (nearest sand/reservoir are used in the wells where the Brent Group is absent). See Figure 12 for location of the wells.

Well	Measured overpressure (BAR)	Modelled overpressure (BAR)	Deviation (BAR)
30/02-02	294.1 - 302.5	310.7	8.2
30/03-02	41.6 - 50.6	113.9	63.3
31/02-01	5.8 - 6.5	7.2	0.7
31/02-05	5.4 - 5.5	7.1	1.6
31/02-08	8.6 - 10.3	12.8	2.5
31/03-03	8.6 - 9.5	6.5	-2.1
34/02-03	255.3 - 255.9	262.3	6.4
34/02-04	201.5 - 247.9	216.8	0.0
34/10-23	385.4 - 390.2	401.9	11.7
35/03-04	48.1 - 64.5	57.0	0.0
35/03-05	10.4 - 15.6	28.3	12.7
35/08-01	200.0 - 206.9	215.2	8.3
35/08-02	170.7 - 184.1	179.5	0.0
35/08-03	184.2 - 192.5	185.6	0.0
35/11-01	6.8 - 7.2	10.1	2.9
35/11-02	145.3 - 158.5	113.9	-31.4

Standard deviation = 18.5

Mean deviation = 9.5

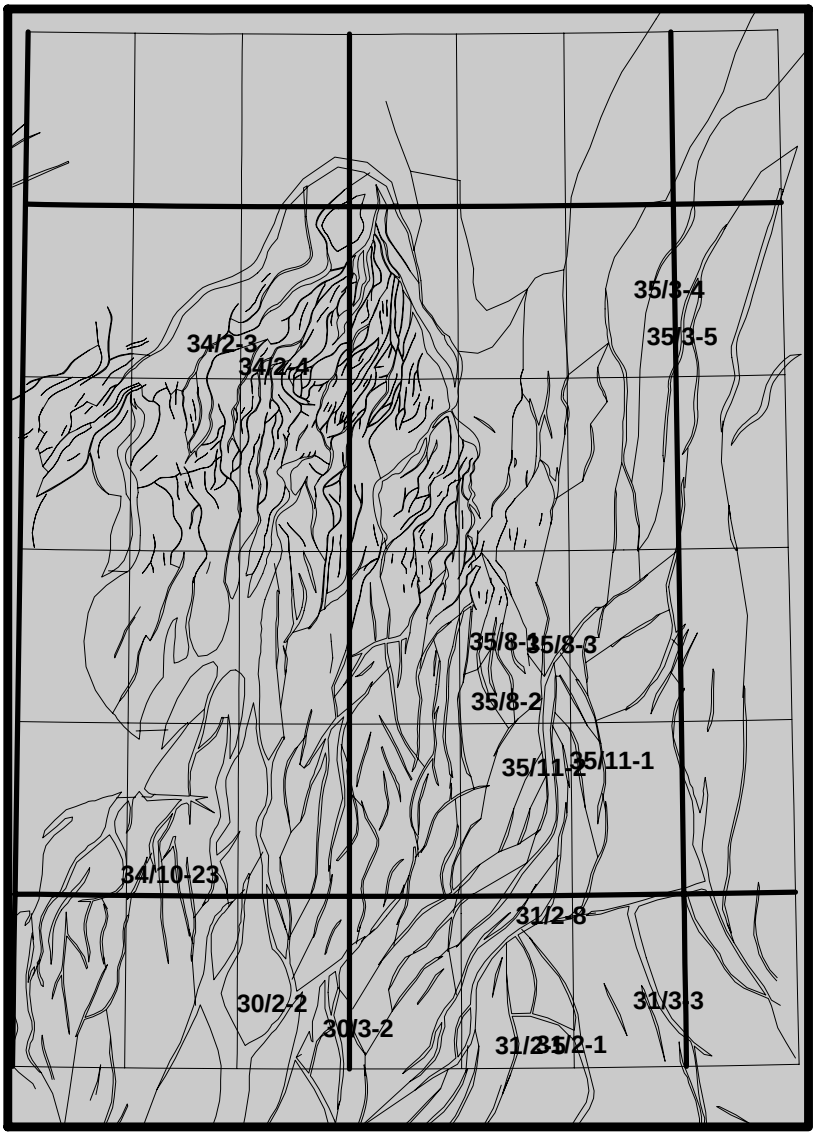

Figure 12 The location of the calibration wells

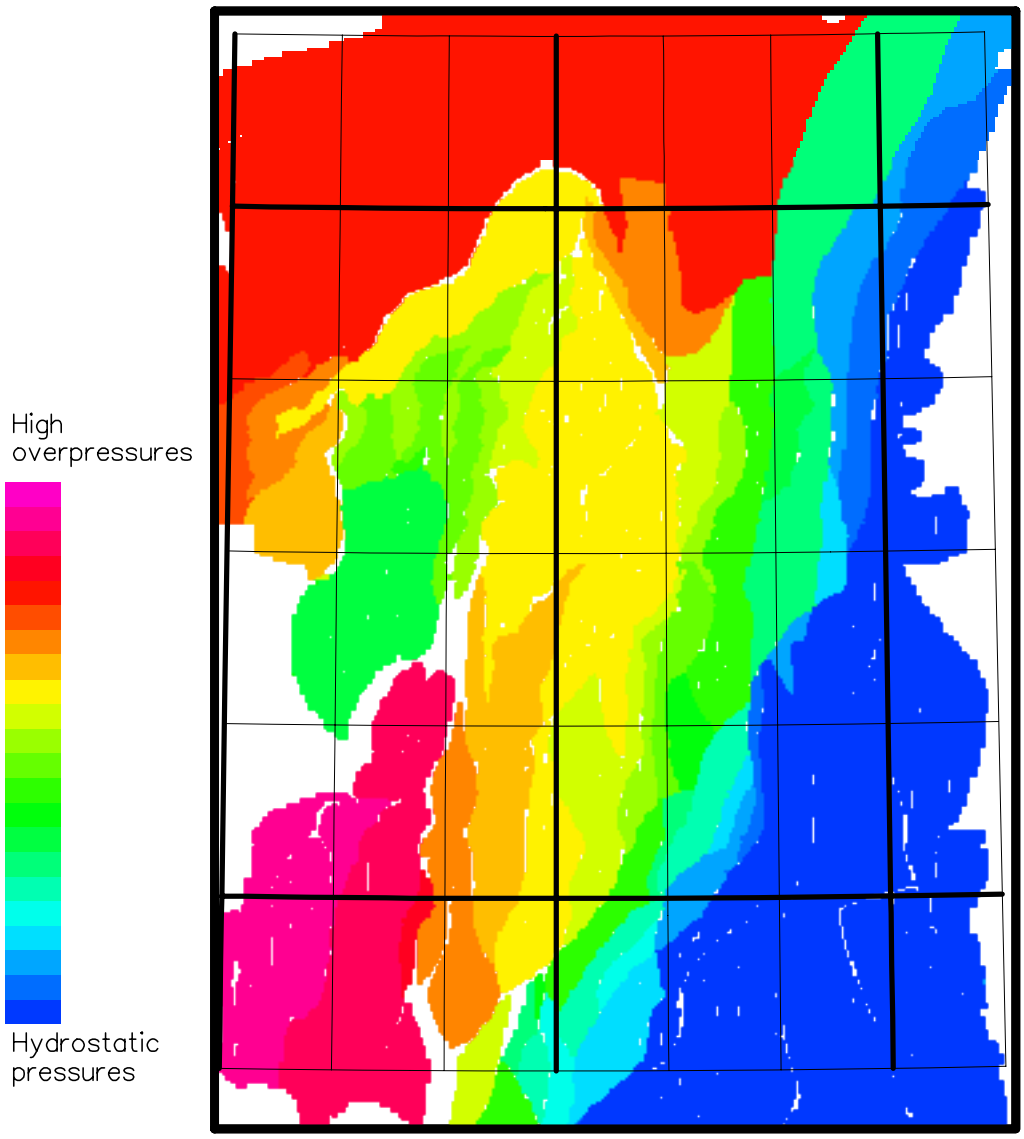

Figure 13 *Present-day overpressures in the Brent Group.*

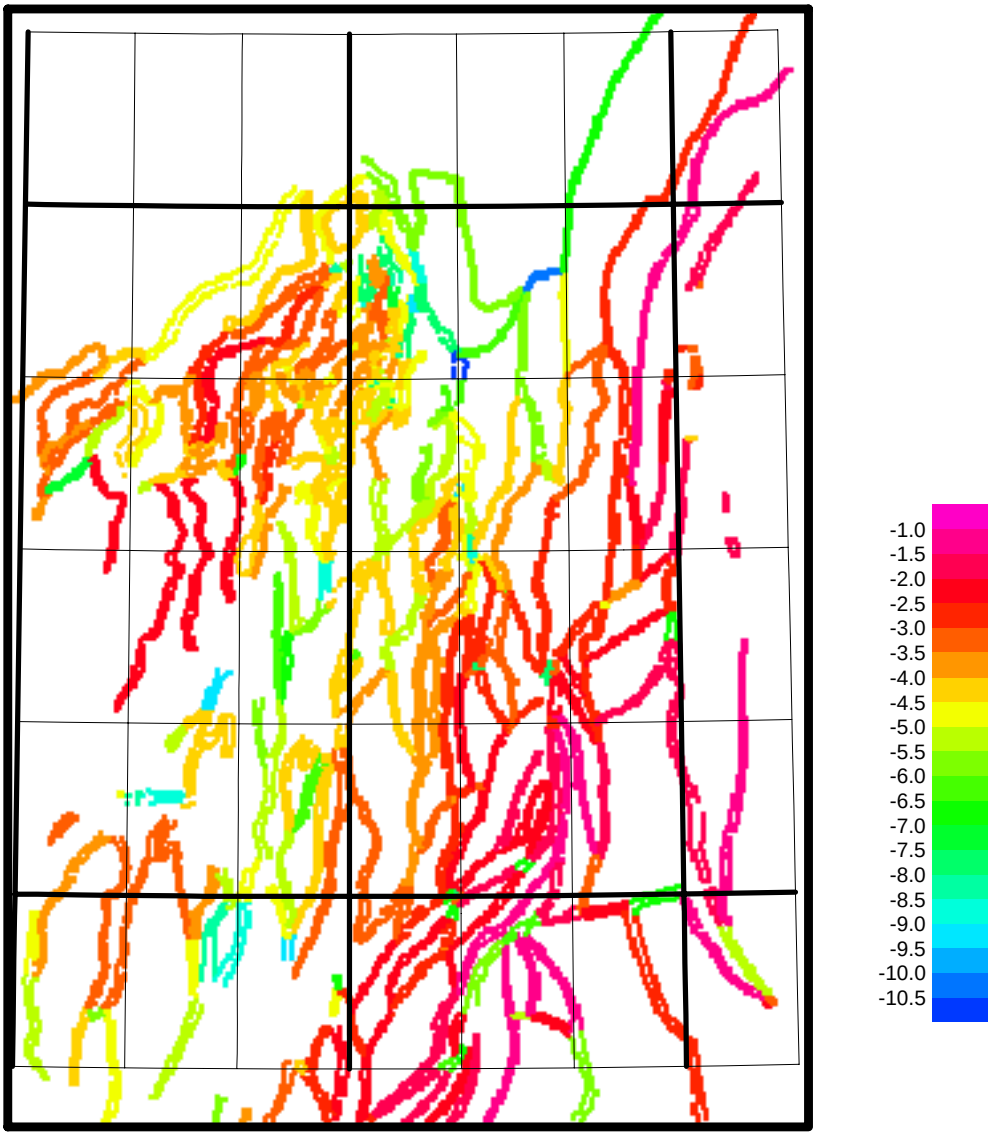

Figure 14 *Average cross-fault transmissibilities* $\left[\mathrm{m}^3\right]$, $\log_{10}$ *scale.*

Sensitivity

In order to understand the importance of each individual parameter in Table 2, a sensitivity analysis was carried out. This was done by varying one parameter while the others parameters remained fixed and then studying the standard and mean deviation of the modelled overpressures. The most obvious effect was that an increase in the transmissibilities resulted in a generally lower basin-wide overpressure and vice versa. This was the case for all the parameters. None of the changes reduced the mean or standard deviation significantly. This means that the deviation function is very close to a local minimum.

Varying parameter B did not cause any changes in the overpressure and this parameter influenced the result only when p had an unrealistically high value. Since B describes the shape of the exponential curve in Figure 7, it is assumed that there is almost complete sealing, and therefore very little water flow, across faults with some offset. All the parameters in Table 2 with the exception of B are plotted in the sensitivity diagram in Figure 15. The curves in Figure 15 show the percentage increase or decrease in mean and standard deviation caused by the specified changes of the parameter on the x-axis.

All the parameters meet the expectations e.g. decreasing the transmissibilities results in higher overpressures. The system seems to remain stable as long as the width of the fault blocks (b) lies within the range of 20 - 25 m. Extending the values beyond this range caused a large increase in the deviations. As long as the values of p are between 0 and 0.1 hardly any change to the mean and standard deviation is seen. Based upon this observation, faults with offset are interpreted to be more or less completely sealing since the p parameter represents the percentage remaining transmissibility at no overlap (Table 1). The model is very sensitive to changes in K_b and ϕ_b (the co-ordinates for the breaking point between the shallow and deep parts of the permeability-porosity-curve). Only small variations cause a dramatic increase in the deviations. The modelled overpressures are very sensitive to changes in c and ϕ_0 as well (the parameters that changes the porosity), while the δ_{sh} and δ_{de} mainly influence the pressures in the shallow and deep parts, correspondingly.

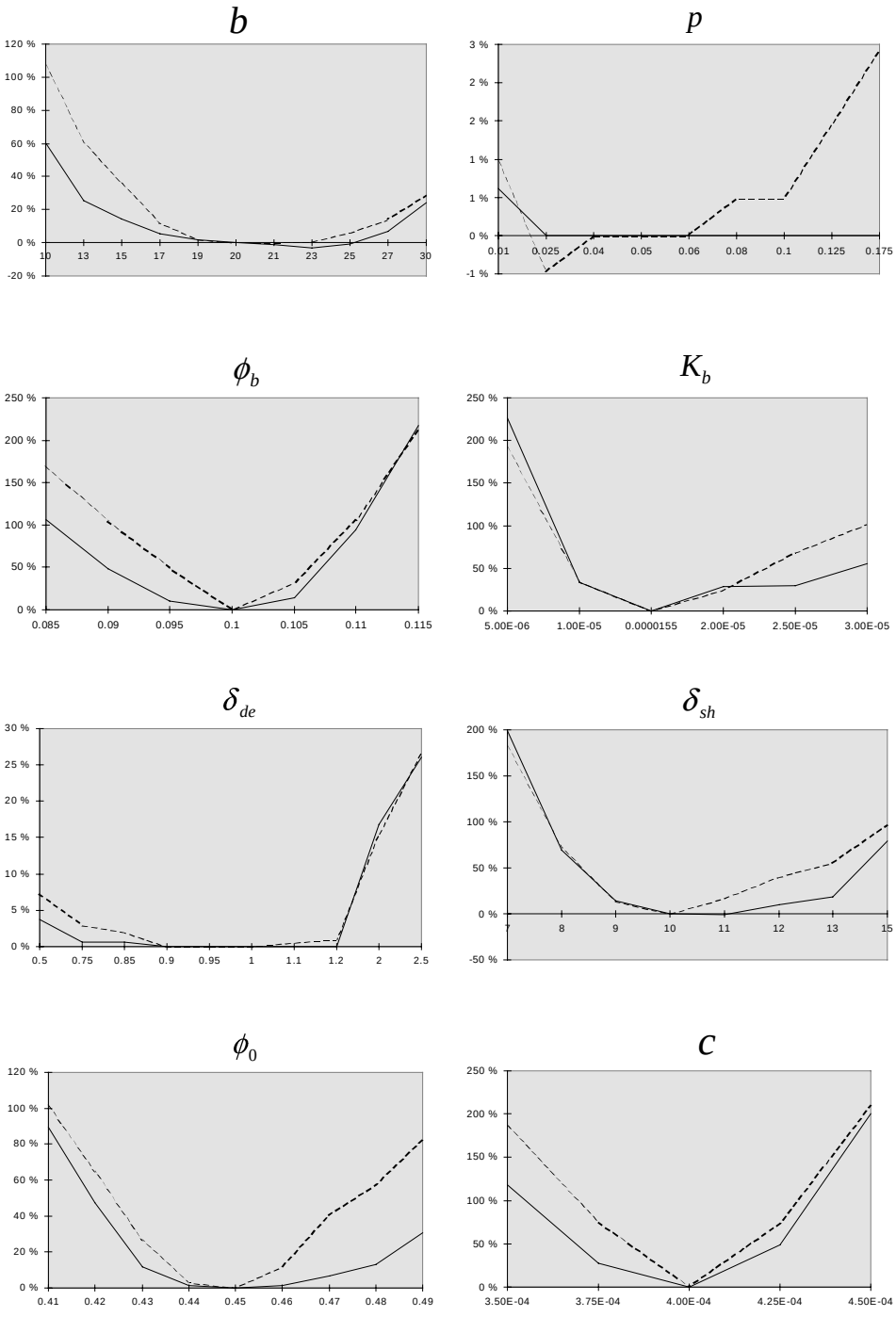

Figure 15 *The percentage variation of mean (continuous lines) and standard (dotted lines) deviation (y-axis) vs. variation of parameters (x-axis)*

Discussion and Conclusions

The deviations in Table 3 are with the exception of wells 30/03-02 and 35/11-02, very acceptable. Well 30/03-02 is located at the edge of the study area and this large deviation may be due to a boundary effect. If the study area were extended southwards a probable drainage path from the southern parts of block 30/03 to the hydrostatic flank would have been included. A drainage to the eastern flank would have reduced the modelled pressures in well 30/03-02. In addition to this, the sensitivity analysis suggests that there is too good communication between well 35/11-02 (which is underestimated) and well 30/03-02. The modelled overpressure in the two cells containing these wells follow each other during both the calibration of the model and the sensitivity study. The pressure cells between blocks 30/03 and 35/11 are long, narrow and oriented in a north-east direction. This means that there are relatively few seals between these two areas. Some of the explanation of the two large deviations in Table 3 may be that the process of defining pressure compartments and/or the fault permeability model is inadequate to describe the fluid flow in this area.

It is important to point out that the best match parameter values presented in Table 2 applied to the model are not an attempt to describe the true transmissibilities across the faults in the study area. It is of course impossible to measure the transmissibilities across large faults in order to verify a transmissibility model for a basin. The main idea behind the approach represented in Equation 2 is that this model describes the distribution of transmissibilities among the faults i.e. the permeability architecture, and thereby reveal a lateral basin-wide pattern of fluid flow.

In one- and two-dimensional models for predicting overpressure, vertical fluid flow compaction plays a key role in creating overpressures (Wangen 1992, Yu & Lerche, 1996). The pseudo three dimensional approach developed in this study does not have the same need for vertical fluid flow in order to create overpressure because the differences in overpressure are introduced by putting “production wells” in some boundary compartments. Nevertheless, in order to achieve the best match it is necessary to increase the vertical permeability so that the vertical fluid flow becomes significant compared to the lateral fluid flow. Based upon this observation, it is necessary to draw the following two conclusions: (1) Smaller scale fractures and faults in sealing layers may cause increasing permeabilities in some areas. This could be a possible explanation why it was necessary to model some communication through the Dunlin Group in Figure 9; (2) It is therefore of crucial importance to find a realistic ratio between lateral and vertical fluid flow when modelling pressure development in three dimensions.

Based upon the results and the relative low deviations all over the study area, we suggest that the lateral overpressure distribution in the pressure compartments is, to a large extent, controlled by the faults and the lateral fluid flow. To describe the regional lateral fluid flow it is not sufficient to characterise the faults as sealing or non-sealing. The results imply that fault transmissibilities can be computed in spite of very large fault seal differences at a local scale. The fact that it is possible to calibrate the model very closely to the measured pressures suggests that the model is a good approximation. Future drillings can reveal the model's ability to predict overpressures.

Acknowledgements

PGS provided the mapped data, interpreted the faults and made the initial version of the fault compartment interpretation.

References

ANTONELLINI, M., AYDIN, A., 1994: Effect of Faulting on Fluid Flow in Porous Sandstones: Petrophysical Properties. AAPG Bulletin vol. 78, No. 3, March 1994.

ANTONELLINI, M., AYDIN, A., 1995: Effect of Faulting on Fluid Flow in Porous Sandstones: Geometry and Spatial Distribution. AAPG Bulletin vol. 79, No. 5, May 1995.

BREDEHOEFT, J.D., BELITZ, K., SHARP-HANSEN, S., 1992: The Hydrodynamics of the Big Horn Basin: A Study of the Role of Faults. AAPG Bulletin vol. 76, No. 4, April 1992.

DARBY, D., HAZELDINE, R.S., COUPLES, G.D., 1996: Pressure Cells and Pressure Seals in the UK Central Graben. Marine and Petroleum Geology, Vol. 13, No. 8, 865-878.

GAUTHIER, B.D.M., LAKE, S.D. 1993: Probabilistic Modelling of Faults Below the Limit of Seismic Resolution in Pelican Field, North Sea, Offshore United Kingdom. AAPG Bulletin vol. 77, no. 5, May 1993.

HEATH, A.E., WALSH, J.J., WATTERSON, J., 1994: Estimation of the Effects of Sub-seismic Sealing Faults on Effective Permeabilities in Sandstone Reservoirs. North Sea Oil and Gas Reservoirs -III, Norwegian Institute of Technology.

KNIPE, R.J., 1992: Faulting Processes and Fault Seal. Structural and Tectonic Modelling and its Application to Petroleum Geology. NPF Special Publication 1.

KNOTT, S.D, 1993: Fault Seal Analysis in the North Sea. AAPG Bulletin vol. 77, no. 5, May 1993.

KOOI H: Insufficiency of compaction disequilibrium as the sole cause of high pore fluid pressures in pre-Cenozoic sediments. Basin Research Vol. 9, No. 3, September 1997.

LOOSVELD, J.R.H., FRANSSEN, R.C.M.W., 1992: Extensional vs. Shear Fractures: Implications for Reservoir Characterisation. SPE 25017.

MANN, D.M., MACKENZIE, A.S. 1990: Predictions of pore fluid pressures in sedimentary basins. Marine and Petroleum Geology vol. 7, February 1990.

NYBAKKEN, S. 1991: Sealing fault traps - an exploration concept in a mature petroleum province: Tampen Spur, northern North Sea. First Break vol.9, no. 5, May 1991.

OSBORNE M J, SWARBRICK R E: Mechanisms for generating overpressure in sedimentary basins: A reevaluation. AAPG Bulletin, Vol. 81, No. 6, June 1997.

PICKERING, G., PEACOCK, D.C.P., SANDERSON, D.J., BULL, J.M., 1997: Modelling tip zones to predict the throw and length characteristics of faults. AAPG Bulletin vol. 81, no. 1, January 1997.

SCLATER, J.G., CHRISTIE, P.A.F., 1980: Continental stretching: an explanation of the post-Mid-Cretaceous subsidence of the Central North Sea basin. J. Geophys. Res., 85, 3711-3739.

SYLTA, Ø., 1993: New techniques and their applications in the analysis of secondary migration. Basin Modelling: Advances and Applications. NPF Special Publication no. 3.

SYLTA, Ø., 1996: Pressure compartments and fault sealing of hydrocarbons: A modelling approach. Abstracts: Hydrocarbon seals - Importance for exploration and production. NPF, January 1996.

UNGERER, P., BURRUS, J., DOLGIEZ, B., CHÉNET, P.Y., BESSIS, F., 1990: Basin evaluation by integrated two-dimensional modelling of heat transfer, fluid flow, hydrocarbon generation and migration. AAPG Bulletin vol. 74, No. 3, p 309-335.

WALDERHAUG O, 1996: Kinetic modelling of quartz cementation and porosity loss in deeply buried sandstone reservoirs. AAPG Bulletin, Vol. 80, No. 5, May 1996.

WALSH, J.J., WATTERSON, J., YIELDING, G., 1994: Determination and Interpretation of Fault Size Populations: Procedures and Problems. North Sea Oil and Gas Reservoirs III, Norwegian Institute of Technology.

WANGEN, M., 1992: Pressure and Temperature Evolution in Sedimentary Basins. Geophys. J. int., 110, 601-613.

WEN, R., SINDING-LARSEN, R., 1994: Probability Kriging of Sub-seismic Fault Throws with Multifractal Distributions. Geostatistics for the Next Century, 488-497.

YIELDING, G., WALSH, J.J., WATTERSON, J., 1992: The Prediction of Small-scale Faulting. First Break vol. 10, No. 12, December 1992.

YU, Z., LERCHE, I., 1996: Modelling abnormal pressure development in sandstone/shale basins. Marine and Petroleum Geology, Vol. 13, No. 2, p 179-193.

3. Stationary overpressure distribution

In chapter 2 an overpressure distribution through time was estimated based upon fluid flow calculations between pressure compartments induced by pressure differences in some chosen boundary compartments. These calculations were rather complicated and time-consuming due to the use of a reservoir simulator. The aim of this chapter is to verify if it is possible to find a present day overpressure distribution using the same concept of boundary compartments and assuming stationary conditions for the lateral flow. The least square solution technique is used to find an overpressure distribution between the boundary values introduced. This methodology is applied to a simple synthetic system (Figure 3.1) and to the North Viking Graben data presented in chapter 2.

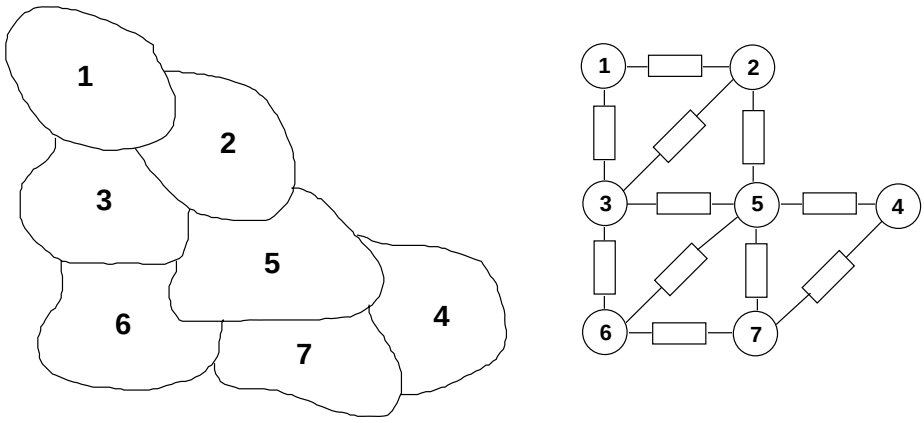

Figure 3.1: A simple synthetic system of pressure compartments (left) and the corresponding network analogy (right)

It is possible to formulate Darcy's law on the same form as Ohm's law where the flux is directly proportional to the difference in potential (Equation (3.1)). The flux q between two pressure compartments is proportional to both the transmissibility T and the difference in overpressure ΔP. μ and B denote the viscosity and the formation volume factor of the fluid, respectively. Part two of Equation (3.1) show that the fault represents a resistance

(R) to the flux across the fault. Figure 3.1 illustrates a simple connected network of nodes, which corresponds to a collection of pressure compartments. It is possible to describe the relations between the potentials for a network of pressure cells using a system of linear algebraic equations as outlined in Equation (3.2). N is the number of nodes (pressure compartments), the matrix A describes the resistance (transmissibility) network, the vector $\mathbf{x}$ contains the potentials (overpressures) and $\mathbf{b}$ contains the net flux in or out of the nodes (pressure compartments).

$$q = \frac{T}{\mu B} \cdot \Delta P$$
$$\Delta P = R \cdot q \qquad (3.1)$$

$$A\mathbf{x} = \mathbf{b} \qquad A \in \mathrm{R}^{N \times N} \qquad \mathbf{x}, \mathbf{b} \in \mathrm{R}^{N} \qquad (3.2)$$

All the entries of the flux vector $\mathbf{b}$ are zero because a stationary flow is assumed. Thus the system (3.2) can be reformulated to (3.3) denoting the flux on node/compartment level. Equation (3.4) is achieved by applying Darcy's law (3.1) to the stationary flow (3.3). This system can be solved with regard to the overpressure without paying attention to the size of the pressure compartments because the pressure is constant due to the assumption of stationary flow conditions. The viscosity μ and formation volume factor B are not included in the rest of the calculations because it is possible to remove them from (3.4) where the right side equals zero. It is assumed that the transmissibility model introduced in the previous chapter handles the strong relationship between depth and overpressure. The transmissibilities T_{ij} in (3.4) are the entries of the matrix A in (3.2) while the diagonal elements are given by the sum of the rows in (3.5). The matrix A is symmetric (since $T_{ij} = T_{ji}$), sparse (since $T_{ij} = 0$ for most i and j) and diagonally dominant. All these qualities are advantageous with regard to finding a simple, robust and efficient algorithm to solve the system (3.2). Equation (3.6) illustrates how (3.2) looks like for the simple example outlined in Figure 3.1.

$$\sum_{j=1}^{N} Q_{ij} = 0 \qquad i = 1, \ldots, N \qquad (3.3)$$

$$P_i \left(\sum_{j=1}^{N} T_{ij} \right) - \sum_{j=1}^{N} P_j T_{ij} = 0 \qquad i = 1, \ldots, N \qquad (3.4)$$

$$a_{ii} = -\sum_{i \neq j} a_{ij} \qquad (3.5)$$

$$\begin{bmatrix} a_{11} & -T_{12} & -T_{13} & 0 & 0 & 0 & 0 \\ -T_{12} & a_{22} & -T_{23} & 0 & -T_{25} & 0 & 0 \\ -T_{13} & -T_{23} & a_{33} & 0 & -T_{35} & -T_{36} & 0 \\ 0 & 0 & 0 & a_{44} & -T_{45} & 0 & -T_{47} \\ 0 & -T_{25} & -T_{35} & -T_{45} & a_{55} & -T_{56} & -T_{57} \\ 0 & 0 & -T_{36} & 0 & -T_{56} & a_{66} & -T_{67} \\ 0 & 0 & 0 & -T_{47} & -T_{57} & -T_{67} & a_{77} \end{bmatrix} \begin{bmatrix} P_1 \\ P_2 \\ P_3 \\ P_4 \\ P_5 \\ P_6 \\ P_7 \end{bmatrix} = \begin{bmatrix} 0 \\ 0 \\ 0 \\ 0 \\ 0 \\ 0 \\ 0 \end{bmatrix} \qquad (3.6)$$

So far all the entries in vector **b** in (3.2) are equal to zero, and every constant solution $P_j = P_0$ for all j satisfies the system. In order to achieve non-trivial solutions it is necessary to specify the overpressure in some compartments. Some of the overpressures P_j may be known due to wells drilled in the respective compartments. These known pressures are removed from the solution vector **x**, multiplied with the respective entries in A and added to the vector **b** in (3.2). If x_j is known it is possible to remove this value from **x** and column j from A. Thus if the overpressure is known in k pressure cells (3.2) will be rewritten as (3.7). The decoupling of the known overpressures destroys the symmetric and quadratic properties of A in (3.2). If the overpressures P_1 and P_4 in (3.6) are known, the system (3.8) is achieved.

$$A\mathbf{x} = \mathbf{b} \qquad A \in \mathrm{R}^{N \times N-k} \qquad \mathbf{x} \in \mathrm{R}^{N-k} \qquad \mathbf{b} \in \mathrm{R}^{N} \qquad (3.7)$$

$$\begin{bmatrix} -T_{12} & -T_{13} & 0 & 0 & 0 \\ a_{22} & -T_{23} & -T_{25} & 0 & 0 \\ -T_{23} & a_{33} & -T_{35} & -T_{36} & 0 \\ 0 & 0 & -T_{45} & 0 & -T_{47} \\ -T_{25} & -T_{35} & a_{55} & -T_{56} & -T_{57} \\ 0 & -T_{36} & -T_{56} & a_{66} & -T_{67} \\ 0 & 0 & -T_{57} & -T_{67} & a_{77} \end{bmatrix} \begin{bmatrix} P_2 \\ P_3 \\ P_5 \\ P_6 \\ P_7 \end{bmatrix} = \begin{bmatrix} -a_{11}P_1 \\ T_{12}P_1 \\ T_{13}P_1 \\ -a_{44}P_4 \\ T_{45}P_4 \\ 0 \\ T_{47}P_4 \end{bmatrix} \qquad (3.8)$$

The matrix A in (3.2) is singular because the row sums equal zero (Equation (3.5)). Assuming the stationary flow (3.3) and prescribing some of the entries in the solution vector **b** in Equation (3.2) result in the decoupled system (3.7) to be overdetermined because there are more equations than unknowns. In other words, a unique relation between transmissibility and changes in overpressure does not exist. In order to find a

pressure vector the least square solution for the system is provided. Too many fixed nodes (known overpressures) may cause problems for the model, because these constraints very easily lead to a system of equations without any plausible solution. Thus a representative selection of boundary compartments only covering the main pressure trends in the study area should be used decoupling the system (3.2) into (3.7).

3.1 Application to a simple test system

Figure 3.1 illustrates a simple system with 7 pressure compartments, which is described mathematically by Equation (3.5). The boundary values shown in Table 3.1 specify the boundary overpressures in cell number 1 and 4 and thus (3.8) apply to the system. The transmissibilities between the cells are given in Table 3.2. In order to calculate the solution-vector MatLab, an integrated technical computing environment delivered by the Math Works Inc, has been used to estimate the least square solution. The resulting overpressures are illustrated in Figure 3.2. The transmissibilities between the cells 2 and 3, 5 and 6 and 5 and 7 are in general significant lower than the rest of the connectivities made. Thus two main paths for fluid flow between node 1 and 4 are made (1-2-5-4 and 1-3-6-7-4).

Table 3.1: Boundary conditions for the simple test system

Cell no.	Overpressure
1	100.0
4	5.0

Table 3.2: Transmissibilities for the simple test system

From cell	To cell	Transmissibility
1	2	$2.0 \cdot 10^{-4}$
1	3	$3.0 \cdot 10^{-3}$
2	3	$1.0 \cdot 10^{-4}$
2	5	$8.0 \cdot 10^{-4}$
3	5	$5.0 \cdot 10^{-5}$
3	6	$5.0 \cdot 10^{-3}$
4	5	$1.5 \cdot 10^{-4}$
4	7	$4.0 \cdot 10^{-3}$
5	6	$3.0 \cdot 10^{-5}$
5	7	$8.0 \cdot 10^{-5}$
6	7	$2.0 \cdot 10^{-3}$

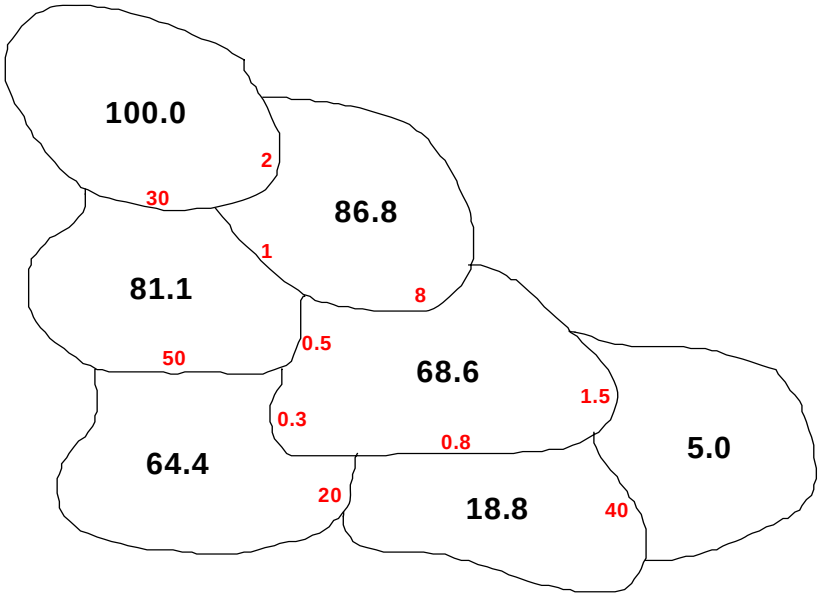

Figure 3.2: Modelled overpressures (black numbers) distribution in the synthetic system. The red numbers show the transmissiblity values.

The pressure distribution achieved using the least square solution plotted in Figure 3.2 seems reasonable, because the overpressures gradually decrease moving from cell 1 to cell 4 (Figure 3.1). Following the two main paths for fluid flow mention above, there is a clear tendency in Figure 3.2 between low transmissibilities and large pressure changes across the faults. The formation water in this simple synthetic basin may follow 11 different flow paths from cell 1 to cell 4. The overpressures in the cells 2, 3, 5 and 6 are relatively high due to the vicinity to the highly pressured cell 1 and only a minor influence from cell 4. The modelled overpressure in cell 7 is low because the relatively high transmissibility that connects this cell to the low-pressured cell 4 drains the overpressure efficiently.

3.2 Application to the North Viking Graben

The methodology deduced in this chapter is applied to the Brent Group in the North Viking Graben area presented in chapter 2. The aim of this section is to test the stationary dissipation qualitatively using real data. Since the measured overpressures in some of the simulations are used as boundary cells it has no meaning to calibrate the model as in chapter 2. If the methodology is able to reproduce the known main pressure trends in the area it may be possible to apply this dissipation method using a system of pressure compartments where the overpressure is generated inside all the cells. In order to avoid

numerical problems it was necessary to remove the small single pixel cells. These tiny pressure cells do not have any geological influence on the system - they are only “noise” from the process of dividing the area into compartments. For all practical reasons the system of pressure compartments used in this section is identical to the Brent system presented in chapter 2. The study area consists of 190 pressure compartments as shown in Figure 3.3.

It is necessary to specify the overpressure in some of the pressure compartments in order to run this model. Which of the cells that are chosen to describe the boundary influence the results. The model has therefore been tested for three different boundary strategies. The model has first been tested by defining the overpressure in some cells that cover the main overpressure trends illustrated in Figure 13, chapter 2. Thereafter the observed overpressures from the exploration wells in Table 3.3 are used as fixed pressures in the model. Finally, both the main trends and observed pressures from the two previous tests are used.

Figure 3.4 shows the modelled present day overpressure when the main trends of the overpressure in the North Viking Graben are specified. Some chosen compartments at the hydrostatic flank, the highly overpressured deep parts of the basin and the intermediate pressured area at the edge of the study area nearby the Visund fields, have fixed pressure values. In addition, the local maximum in overpressure in the northern part of the graben is given and decoupled from the system. Since this simplified stationary model does not include any generation mechanisms, all local maximum and minimum values should be given in addition to the boundary pressures. Although all depth- and time-dependencies, vertical fluid flow and geological history are excluded from this simplified model, the overpressure distribution Figure 3.4 seems to be satisfactory on a basin scale. In the southern part of the study area the smooth transition from a very high overpressure to the hydrostatic flank is maintained while in the northern part of the graben forms a highly pressured ridge. Thus this simple model describes the main basinwide pressure trends. The eastern hydrostatic flank is obviously modelled too far in the western direction. The overpressure should be modelled into shallower parts of the basin. This can be achieved by reducing the transmissibilities in the shallow parts instead of adopting the transmissibility values from the best match simulation in chapter 2.

The modelled overpressures in cell 32 and cell 20 in Figure 3.5 are equal to 419 and 401 bar, respectively. According to the simplified model introduced in this chapter the overpressure in cell 56 should lie between 401 and 419 bar. Due to the small size of cell 56 the transmissibility values $T_{\{20,56\}}$ and $T_{\{32,56\}}$ are very low. Based upon the basinwide relation between connectivities and differences in potential, the solution suggested by the least square method models the overpressure in cell 56 to about 700 bar. This artificial

“wrench-effect” often strikes small cells, cells at the edge of the basin and cells that border on faults with a large displacement (off-set). To avoid this annoying situation, small cells at the edge of the study area should be removed. Sometimes it is possible to prevent a “pressure wrench” by fixing the overpressure in nearby pressure compartments. In the situation presented in Figure 3.5 the best solution is to recalculate the overpressure in cell 56 locally. Subsequent to the least square calculation the overpressure in cell 56 should be re-estimated locally based upon the overpressure in the cells 32 and 20 and the connectivities to the two respective cells.

Figure 3.6 shows the resulting overpressures from the run using the released exploration wells listed in Table 3.3 as fixed pressure compartments (see Figure 12, chapter 2 for the locations of the wells). These wells are located in certain areas and do not necessarily describe an appropriate boundary for the model. The overpressures in the graben are obviously modelled too high. Thus the transition in the southern part becomes too narrow and the ridge in the north too high. Otherwise the modelled overpressure in the study area is very satisfactory. Both the Visund area, the deep area in the south-western corner of the study area and the depth at which the overpressure starts accumulating seem to match the observed data very well.

Figure 3.7 shows the results from running the model including the boundary cells from both the two previous simulations. Introducing a relatively large number of boundary cells resulted in a too strictly constrained system of equations that again lead to extensive wrench-effects and numerical artefacts. In order to get a reasonable result for this model small pressure compartments were removed, decoupled or recalculated locally. Figure 3.7 reveals that the results from this simulation are very close to the previous one with the exception that some parts of the overpressure in the north-western part of the graben is modelled closer to the values presented in chapter 2.

Figure 3.8 shows the difference between the modelled overpressures in Figure 13 chapter 2 and in Figure 3.7. The blue coloured axis following the graben confirms that the simplified model estimates these pressures to be too high. A parallel red coloured axis to the west of the graben indicates that the simplified model models the overpressures too low. The two axes clearly indicate that the simplified model provides a flatter pressure distribution and thus the transition zones are modelled to be narrower than the corresponding zones modelled by the dynamic model.

In conclusion, the methodology introduced in this chapter is an appropriate and simple tool able to roughly estimate a present day overpressure distribution in a basin based upon the overpressures specified in some of the compartments. Although the assumed stationary flow and the specified overpressures overdetermine the system, it seems that the

methodology is able to suggest a reasonable solution to a real data set. Consequently, the method should be applied to a system where pressure is generated in all the pressure compartments at certain intervals through time. The stationary dissipation can thus be used as an algorithm performing lateral pressure distribution. If not, the stationary description should be replaced with a methodology modelling dynamic flow between the pressure compartments.

Table 3.3: The overpressure in the exploration wells used for input to the stationary flow model

Well	Overpressure (bar)
30/02-02	338.6
30/03-02	93.0
31/02-01	14.4
31/02-05	14.8
31/02-08	20.0
31/03-03	11.1
34/02-03	300.8
34/02-04	256.2
34/08-01	145.1
34/08-02	165.9
34/08-03	149.3
34/10-23	384.5
35/03-04	89.1
35/03-05	54.9
35/08-01	188.7
35/08-02	157.3
35/08-03	157.1
35/11-01	17.6
35/11-02	103.0
36/01-01	0.0

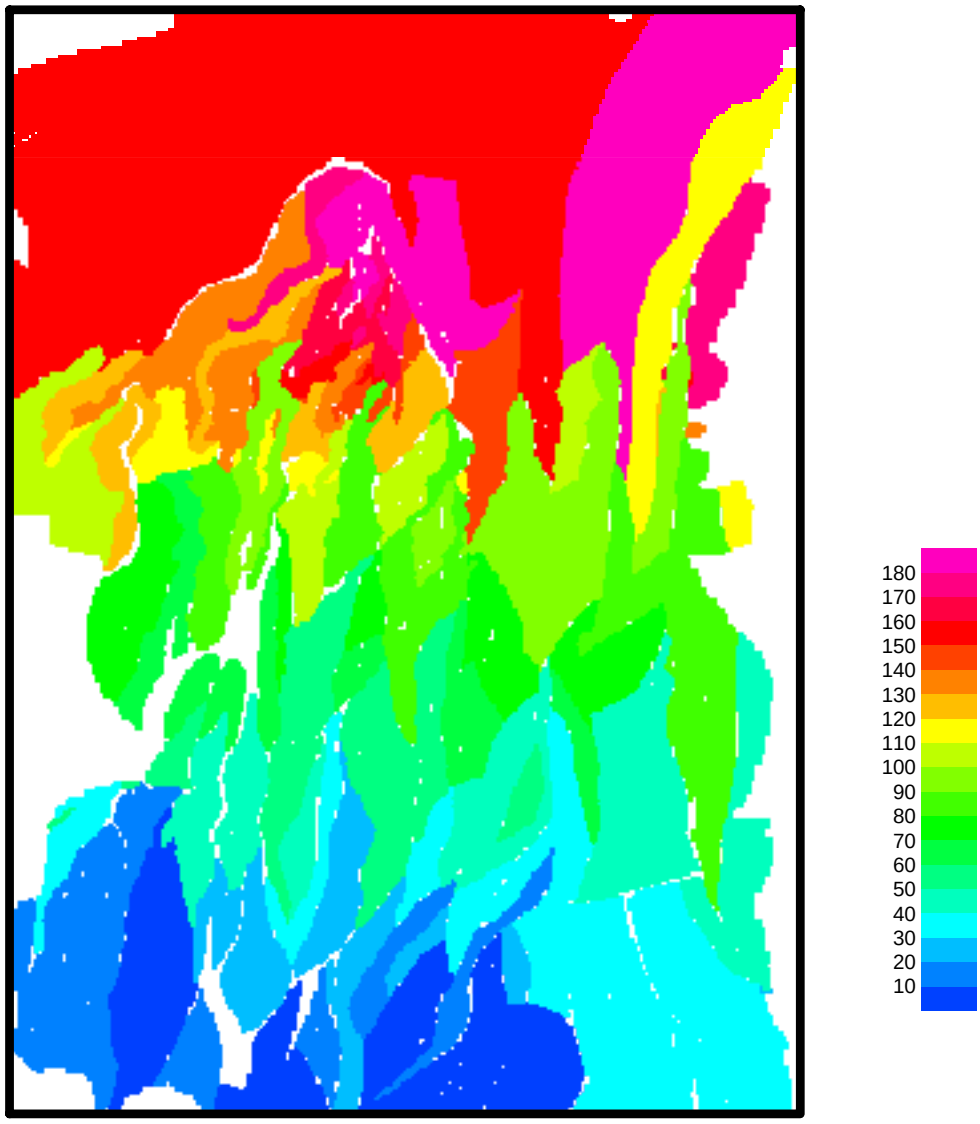

Figure 3.3: *The North Viking Graben divided into pressure cells. The colours indicate a name on the compartments. See Figure 2, 4 and 12, chapter 2 for location of the study area.*

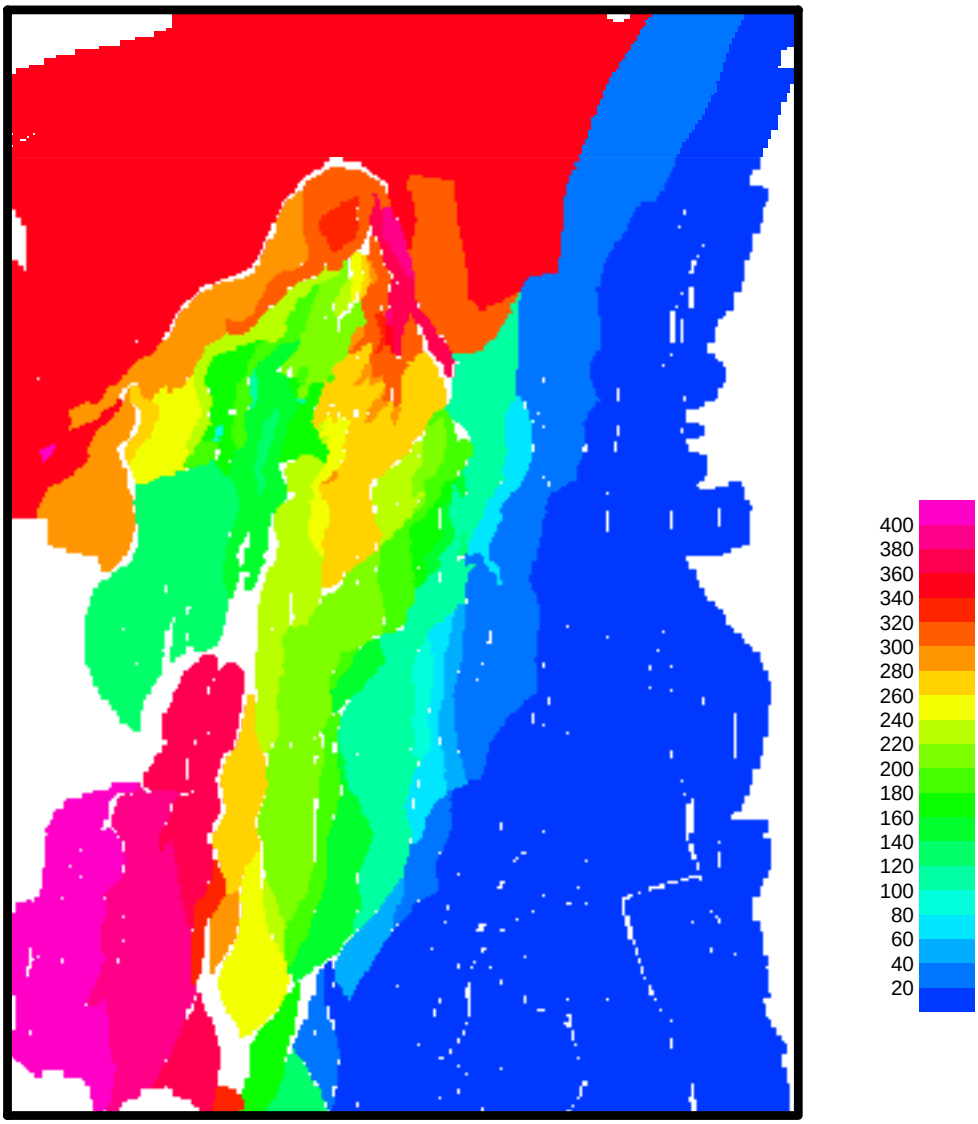

Figure 3.4: *The modelled present day overpressure* (bar), *the main trends are specified. Compare this plot to Figure 13, chapter 2, to see the deviation from the previous modelled result.*

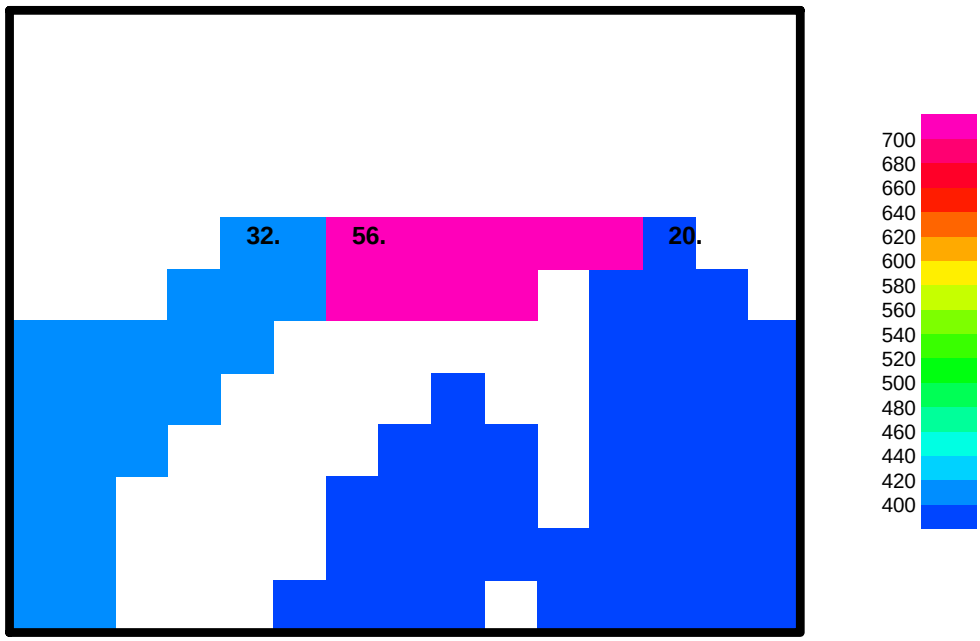

Figure 3.5: *Modelled overpressure* (bar) *in a small pressure cell. The artificial high overpressure in cell 56 is caused by the "wrench-effect" described in the text*

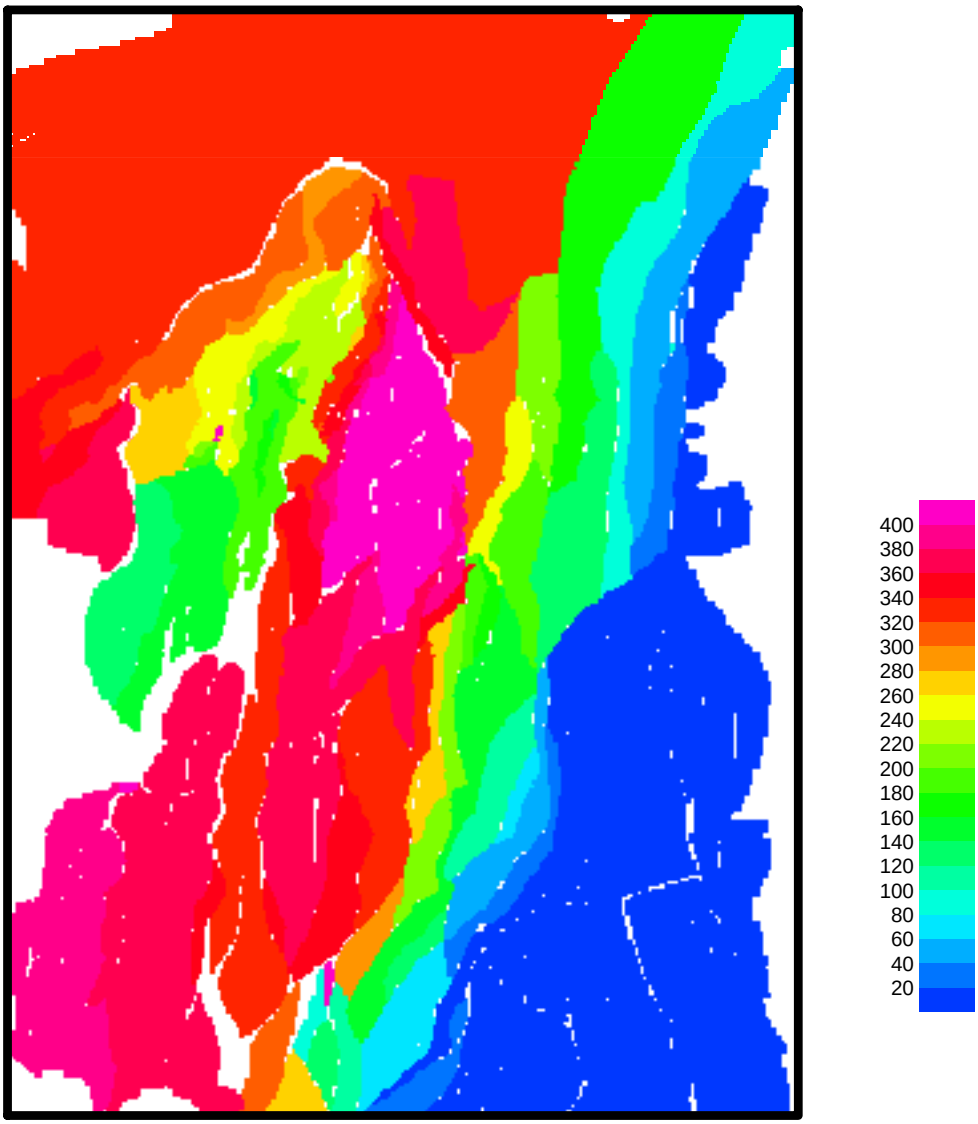

Figure 3.6: *The modelled present day overpressure* (bar)*, the overpressures from the released exploration wells are specified. Compare this plot to Figures 13, chapter 2, to see the deviation from the previous modelled result.*

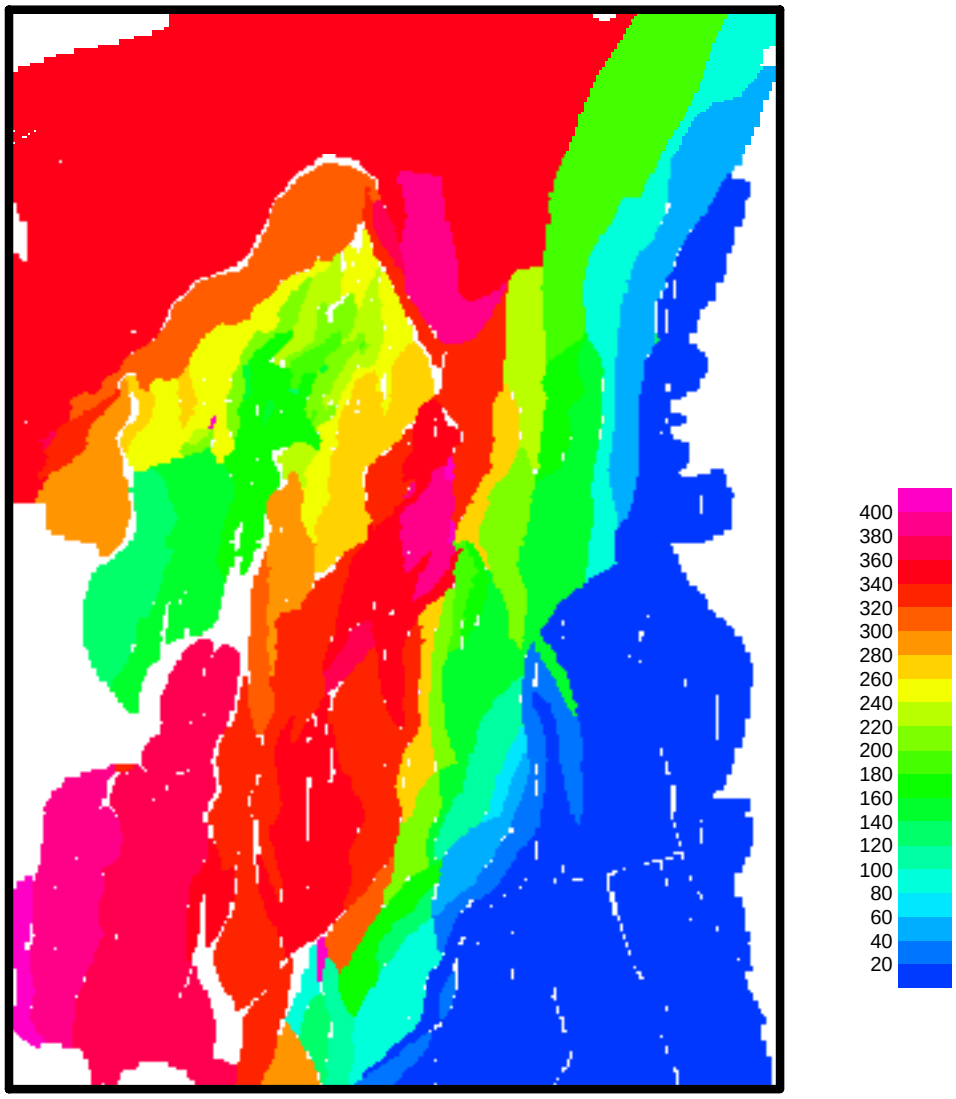

Figure 3.7: *The modelled present day overpressure* (bar), *the overpressures from both the main trends and released exploration wells are specified. Compare this plot to Figures 13, chapter 2, to see the deviation from the previous modelled result.*

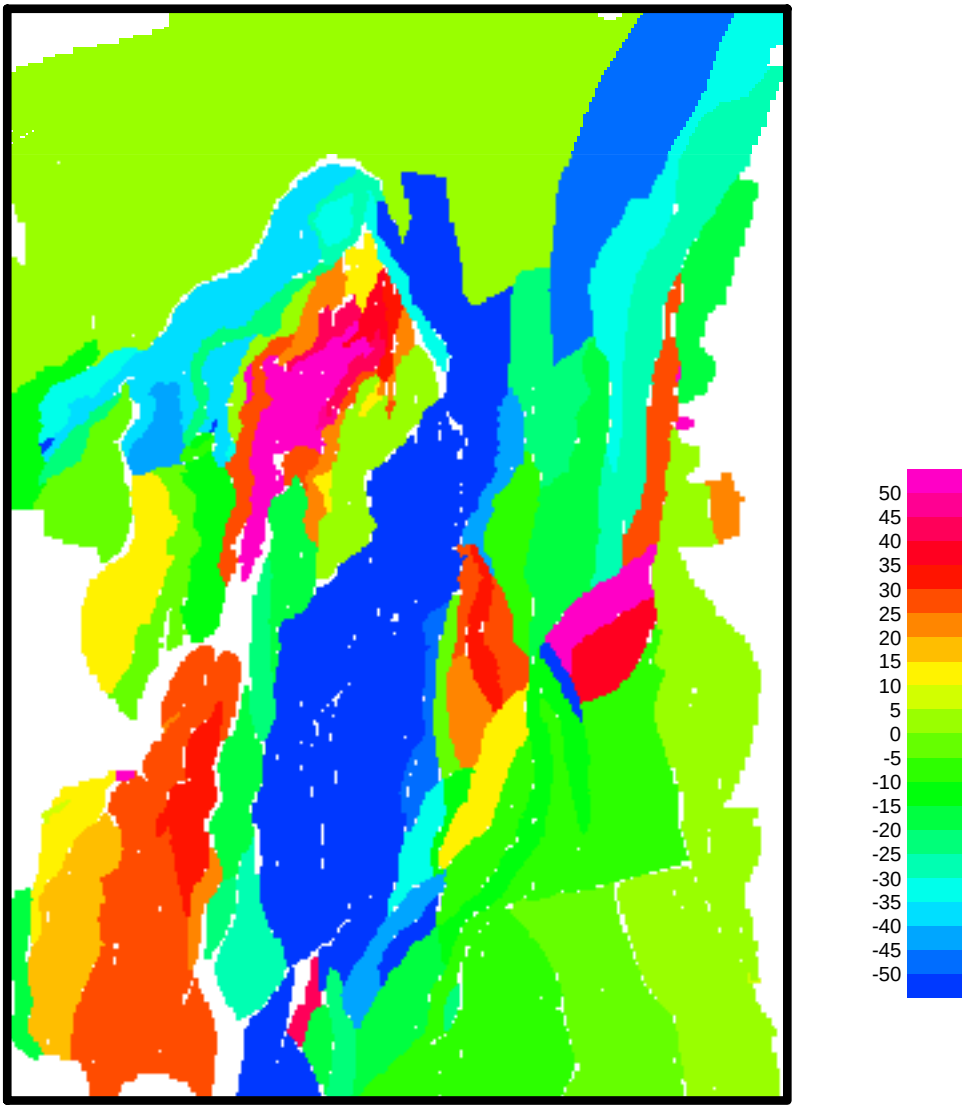

Figure 3.8: *The difference in overpressures* (bar) *between the FMC-model (Figure 13, chapter 2) and the simplified static model (Figure 3.7)*

4. Modelling in a regular grid

The concept of pressure compartments, which is used in chapters 2 and 3, has several benefits. It is an easy representation of a complex phenomenon and it provides a simple and realistic description of the regional fluid flow. The pressure compartments allow a very high resolution of the basin because the connected faults define the flow pattern. In addition, the number of pressure compartments or flow cells is reduced to a minimum. However, there might be some problems including arbitrary shaped pressure cells in a basin- or reservoir-simulator. The size of the pressure compartments may vary over several orders of magnitudes causing numerical problems. In addition, the faults do not follow rectangular grid blocks and thus result in a lot of work in reconstructing the faults using a grid refinement device. It might be necessary to increase the resolution in order to catch the fault pattern, subsequently increasing the size and complicating the computer model. If it is possible to convert the fault properties to a rectangular grid the lateral transmissibility model introduced in chapter 2 is accessible for simulators using equally sized and rectangular shaped nodes. In this chapter an algorithm for converting a fault-based pressure compartment representation into a rectangular grid block system is suggested and tested to the methodology introduced in chapter 3.

4.1 The Rectangular Grid Transmissibility Model (RGTM)

The idea behind the RGTM-algorithm is that it should be possible to calculate a resulting transmissibility between quadrangular grid blocks based upon the underlying faults. The dotted lines in Figure 4.1 represent the grid blocks in a conventional simulator while the curved lines represent the faults. According to this model the flow between grid nodes A and B in Figure 4.1 is controlled by the fault transmissibilities within the tilted RGTM grid block. Thus this algorithm needs an underlying fault transmissibility model to work.

In order to simplify the calculation of the resulting transmissibility T_{AB} the following three following assumptions are made:

1. Stationary flow (the net flux equals 0 for all the compartments within the RGTM grid nodes).
2. The flux through the RGTM-block, Q_{AB}, equals 1.
3. The overpressure at node A, P_A, equals 0.

These assumptions do not reduce the validity of the result because the transmissibility T_{AB} is constant with regard to flow regime, water-flux and overpressure. Thus the Darcy law applied to the resulting transmissibility (Equation (4.1)) simplifies to (4.2).

$$Q_{AB} = T_{AB} \cdot \Delta P_{AB} = T_{AB} \cdot \left(P_B - P_A \right) \qquad (4.1)$$

$$T_{AB} = \frac{1}{P_B} \qquad (4.2)$$

Equation (4.3) is achieved by doing the same mathematical formulation as in the deduction of the static model in chapter 3. This equation defines a system of linear equations, which is symmetric, sparse, diagonal dominant and positive definite.

$$\sum_{j=0}^{N} T_{ij} P_j - \sum_{j=0}^{N} T_{ij} P_i = \begin{cases} -1 & i = 0 \\ 0 & i = 1, \ldots, N-1 \\ 1 & i = N \end{cases} \qquad (4.3)$$

The T_{ij}-values are be given by Equation (4.2) and thus the system can be solved with regard to P_i.

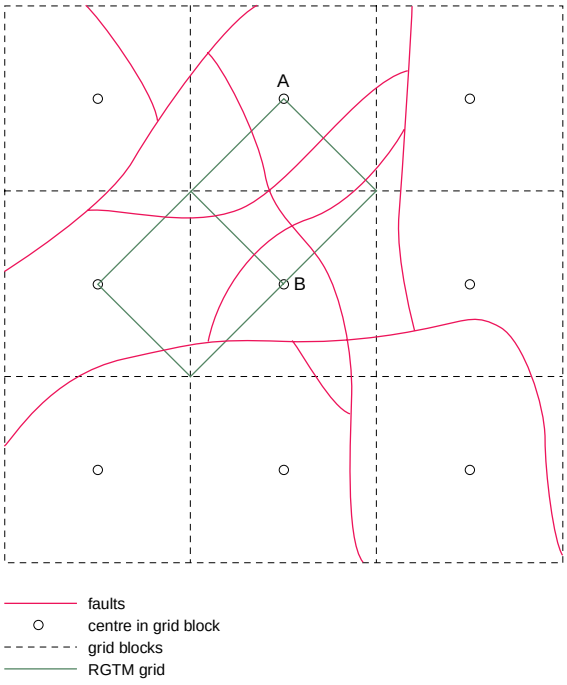

Figure 4.1: Sketch showing the geometric principles behind the RGTM-algorithm that distributes the fault properties to transmissibilities between rectangular grid blocks.

4.2 The RGTM-model applied to the NVG

The Rectangular Grid Transmissibility Model (RGTM) is applied to the study area presented in chapter 2 and in section 3.2. The algorithm divides the area of interest into a mosaic-like pattern consisting of tilted squares or rectangles. Figure 4.2 shows the North Viking Graben divided into a 11×14 RGTM-grid, while Figure 4.3 shows the resulting transmissibility map when the transmissibility model presented in chapter 2 and the RGTM-algorithm are applied to the area. The stationary dissipation model introduced in chapter 3 is applied to the RGTM-grid and the resulting overpressures plotted in Figure 4.4. This plot includes all the main trends of the overpressure in the area: The hydrostatic flank, the highly pressured deep parts of the North Viking Graben and the intermediate pressured areas located close to the Visund fields. In addition this figure shows the location and the values of the overpressure that are used as boundary conditions. These results clearly demonstrate that the RGTM-approach is a useful way to distribute fault-related properties to a regular grid representation.

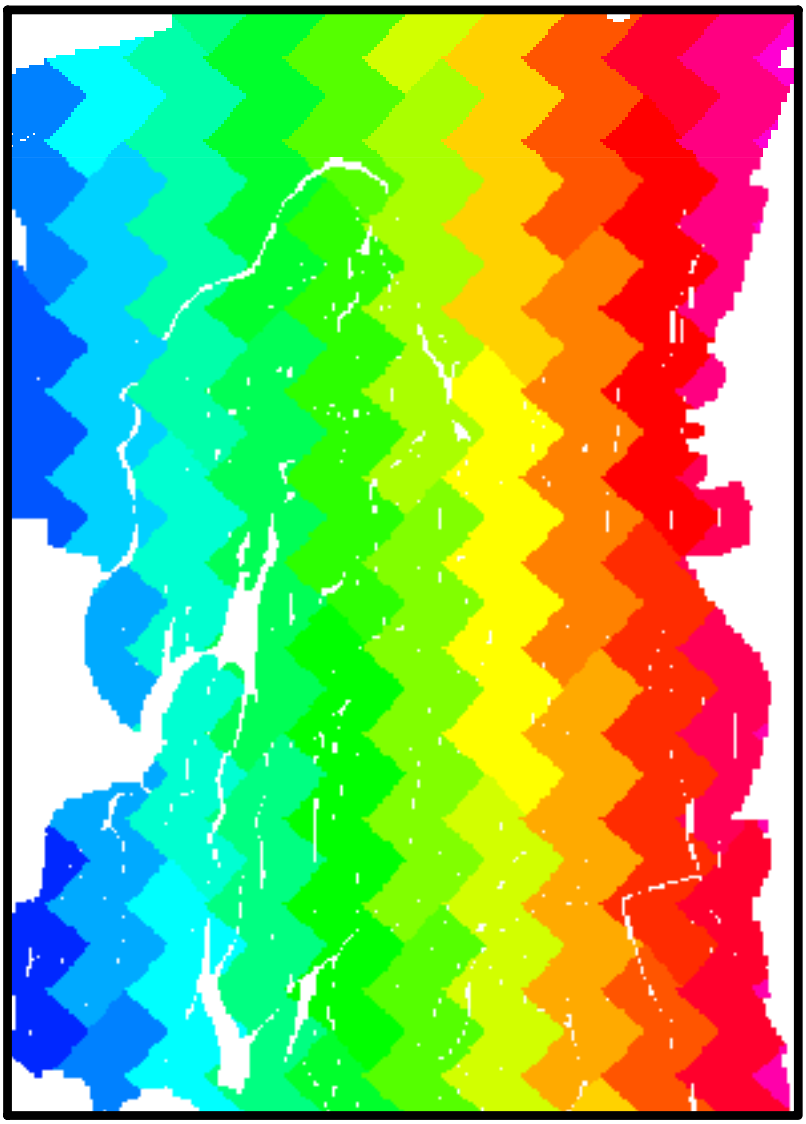

Figure 4.2: The North Viking Graben divided into an 11×14 *RGTM-grid*

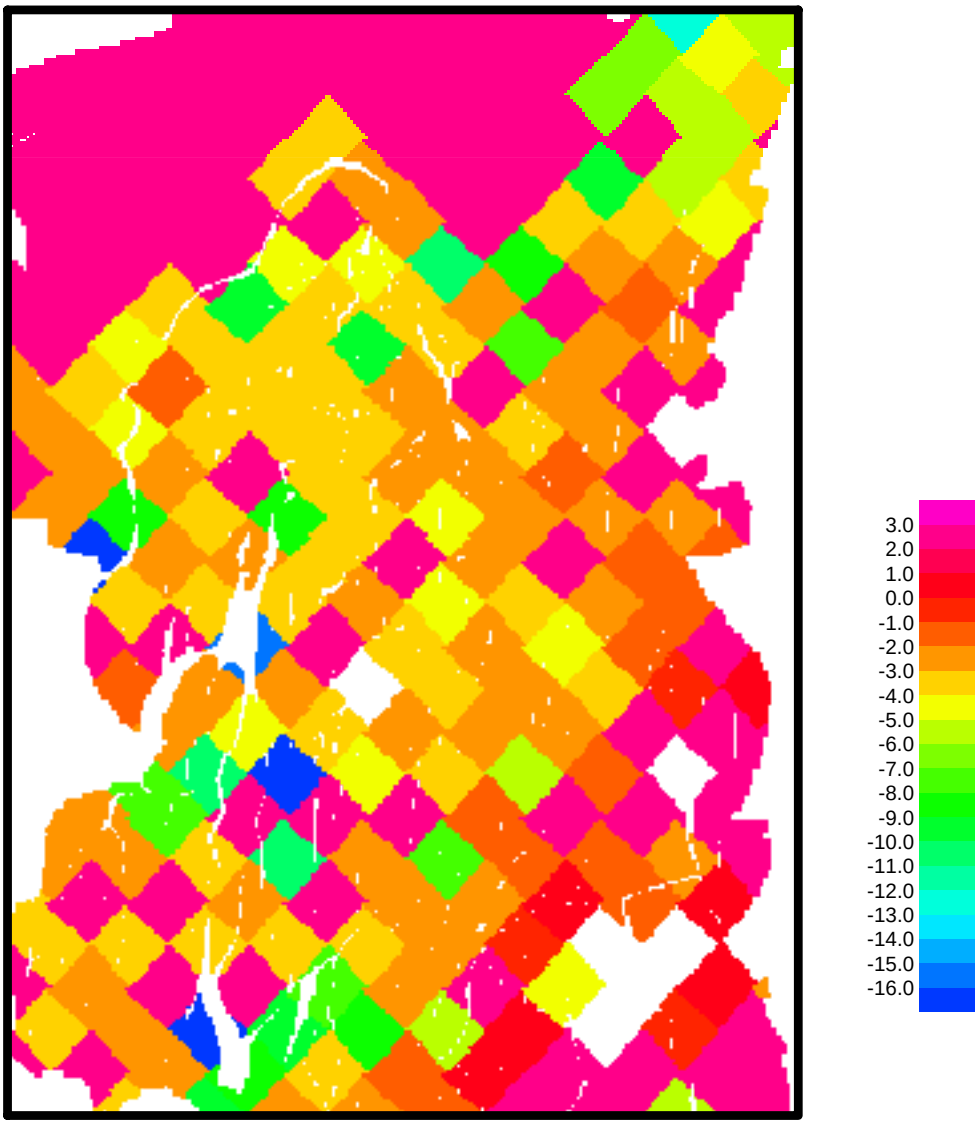

Figure 4.3: *An RGTM-based transmissibility* [mDm] *map (*$\log_{10}$ *scale) of the North Viking Graben*

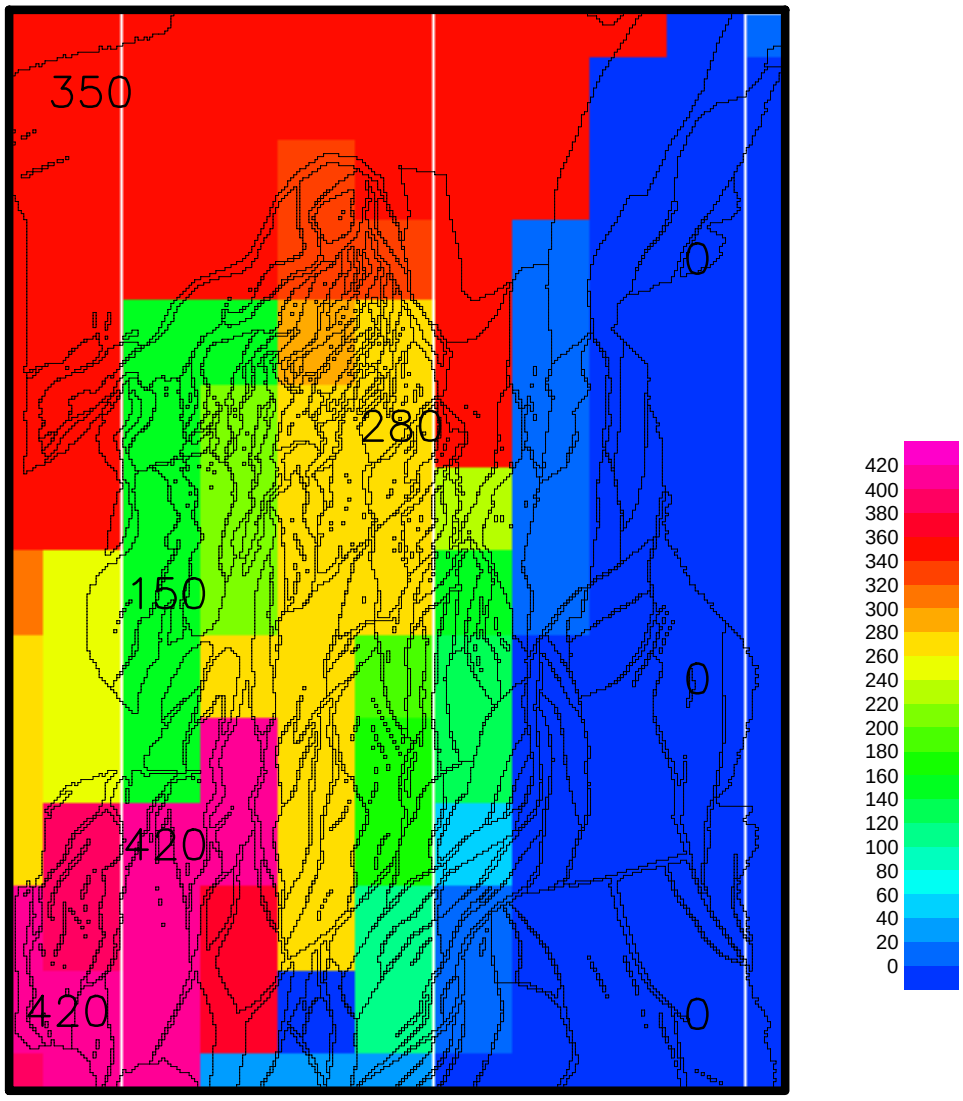

Figure 4.4: *Modelled present day overpressure* (bar) *in the North Viking Graben calculated by applying the static dissipation model to the RGTM-grid. The overpressures on the plot show the values and location of the predefined pressures.*

5. Fluid dynamics in sedimentary basins

In the previous chapters attention was paid to the effects of lateral flow and pressure dissipation. Quantifying the mechanisms generating overpressure and including a model for vertical fluid flow create a more complete and realistic description of a sedimentary basin. Thus it is possible to eliminate the need for both the use of a reservoir simulator and the concept of boundary compartments. A more unique model for the description of basin scale fluid flow is achieved since the choice of boundary compartments and overpressures within these cells affect the results.

The vertical fluid flow model introduced in this chapter is simply based upon the assumption that low permeable clays and shales retard the flow of formation water and thus allow the accumulation of overpressure. At which depth the clay/shale start to retard the vertical flow may vary in different basins. A simple model describing the accumulating properties of a basin is introduced. Both the lateral and vertical fluid flows are calibrated in the case studies in chapter 6 in order to match the observed present day overpressures. In addition, hydraulic leakage from the top points of the compartments is modelled if the pressure exceeds the lithostatic pressure.

As discussed in the introduction there are several properties that contribute to build up the overpressure. In this chapter porosity reduction caused by quartz cementation is chosen as the dominating internal source and shale undercompaction as the dominating external source for overpressure generation in the sand formations. These two mechanisms are implemented and tested to the data sets presented in chapter 6.

The pressure modelling case study performed in chapter 2 uses constant transmissibilities through time. This means that the present day offsets and overlaps across the faults are used for estimating the connectivities between the pressure compartments throughout the geological history. The consequences of this simplification may not be as extensive it might seem. Firstly, the dynamic nature of the modelled overpressure reduces the significance of the paleo fault geometry. Secondly, many basins have been geologically passive in large parts of the Cenozoic. Thus the present day fault geometry is of vital importance to the pressure distribution in many sedimentary basins. The methodology presented in this chapter is implemented in the PRESSIM simulator (Appendix B). This simulator updates the transmissibilities at certain points of time during the geological history based upon the changing depth and fault geometry. This is, however, not a complete dynamic description of the fault connectivities in a basin, because fault diagenesis, which is not discussed in this thesis, influences the fault transmissibilities independent of the fault geometry.

The starting point for the simplified stationary model in chapter 3 is equation (3.3), which states that the flow into a cell is equal to the flow out of it. In addition to the in- and outflux from the neighbours a sink and a source are introduced to each pressure cell as in equation (5.1). The sink and source terms are supposed to account for vertical fluid flow and to handle eventual internal generation of overpressure. By introducing these two additional terms two aims are achieved. Firstly, the static simplification that the net flow into a pressure compartment equals zero is abandoned allowing a dynamic situation to be modelled. Secondly, by using this formulation it is possible to model pressure generation within each pressure compartment. Figure 5.1 shows a schematic outline of the processes that are included in the description of fluid dynamics in a sedimentary basin.

$$\sum_{j=1}^{N} q_{ij} + Q_{\text{source}} - Q_{\text{sink}} = 0 \qquad i = 1,\ldots,N \qquad (5.1)$$

The stationary flow assumed in chapter 3 is now abandoned. A change in the overpressure in the pressure cells is estimated based upon the vertical flux instead of decoupling the known overpressures in some of the compartments as shown in (3.7). Equation (5.1) is solved frequently in order to model the development of overpressure. Lateral dissipation, the modelled vertical flow and the amount of generated pressure are used to calculate the net flux into or out of each pressure cell. Based upon this estimated flux a change in overpressure is suggested in each pressure compartment and the pressure vector corrected.

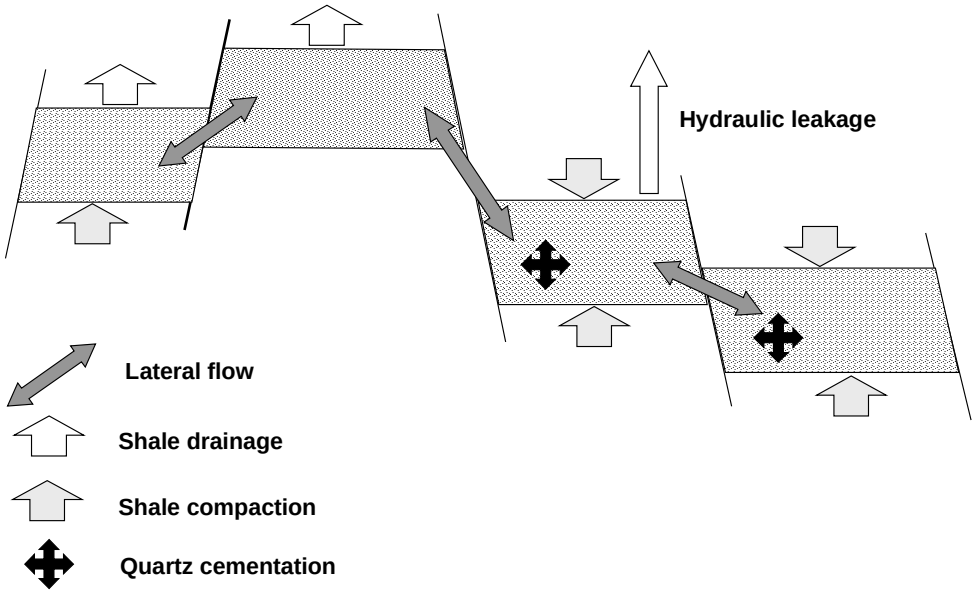

Figure 5.1: Schematic outline of the modelled processes in the basin

There exist two conceptual models in which the occurrence of overpressure can be categorised (Neuzil, 1995 and Luo and Vasseur, 1997). The first one is a dynamic model suggesting that the pressure disequilibrium is generated by ongoing processes, while the second static model suggests that the overpressure generated is a relic of previous geological processes which have been preserved through geological time. Which one of these two conceptual models that is closest to the outlined model depends upon the rates of the five fundamental hydrodynamic processes sketched in Figure 5.1. The pressure simulations to be carried out in the next chapter should indicate which one of these two conceptual models that best describe the nature of overpressure.

Least squares solutions of systems including vertical flow

The simple test system presented in section 3.1 (Figure 3.1) is used to test whether the least square solution technique used in the two previous chapters can be applied to Equation (5.1) and predict changes in the overpressures. The vertical net flux denoted as Q_{source} - Q_{sink} in Equation (5.1) is specified in the second column in Table 5.1 and Table 5.2 and put into the vector $\mathbf{b}$ in Equation (3.2). It is not necessary to specify the real vertical flux in this model, only a realistic ratio between the fluxes into the pressure compartments. The solution vectors in the third columns in Table 5.1 and Table 5.2 are achieved by using the least square technique to (3.2). A normalised solution is listed in the fourth columns.

The resulting changes in overpressure seem to be reasonable. Cell 3 has a larger increase in overpressure than cell 2 in spite of a lower net influx, both in run 1 and 2. The lateral connectivity between cell 1 and 3 is much higher than between cell 1 and 2. This shows that the model is able to handle both the net in-flux and simultaneously dissipate overpressure laterally in an expected manner. The same situation is observed when cell 5 and 6 are compared. Although these two cells have more or less the same net influx, cell 6 achieves a much higher increase in overpressure due to the relatively high connectivity to the most intensively pressure-generating cells.

The same methodology was applied to the compartmentalisation of the North Viking Graben, but the results did not make sense at all. The wide range of transmissibilities together with the more complex pressure distribution made it impossible for this simple methodology to work. Hence, this simplified way of handling generation and dissipation of overpressure does not work in real problems, and it is necessary to develop a more realistic geological description in order to handle real sedimentary basins.

Table 5.1: Net vertical influx, solution and converted pressure, run 1.

Cell no.	Net influx, $\lvert Q_{\text{sink}} - Q_{\text{source}} \rvert$	Solution vector **x**	Normalised solution vector
1	5.0	1943	1.00
2	2.0	443	0.56
3	1.8	843	0.68
4	0.0	-1473	0.00
5	0.5	-732	0.22
6	0.4	127	0.47
7	0.1	-1151	0.09

Table 5.2: Net vertical influx, solution and converted pressure, run 2.

Cell no.	Net influx, $\lvert Q_{\text{sink}} - Q_{\text{source}} \rvert$	Solution vector **x**	Normalised solution vector
1	5.0	5642	1.00
2	2.0	3603	0.65
3	1.8	4111	0.74
4	0.0	-178	0.00
5	0.1	529	0.12
6	0.1	2879	0.53
7	0.0	-217	-0.01

5.1 Vertical fluid flow model

The great variability and poor understanding of the large variation of the shale permeabilities are major obstacles to the accurate description of fluid flow in sedimentary basins (Yang and Aplin, 1998). It is not obvious that the Darcy law describes the flow through shales in general. An impermeable shale layer may force the main part of the fluid flux through inhomogeneities like fractures and cracks. Even though the shales allow Darcy flow to take place, the slow dissipation caused by the low permeabilities may lead to hydraulic fracturing and flow through fractures. Hence, two different flow regimes are able to take place simultaneously. There exist two reasons for developing an alternative shale-sealing model to the traditional permeability-depth estimates: Firstly, it is unlikely that there exists a unique relation between shale permeability and depth in a basin. Laboratory permeabilities at similar porosities can vary by a factor of 10^3 (Neuzil, 1994). Secondly, it is probably more relevant to model a change in the flow regime rather than a reduction in

permeability when the shales become sealing. Although it is clear that transmissive fractures or other heterogeneities control the large-scale hydraulic behaviour of certain argillaceous units, the permeability of many others is scale independent (Neuzil, 1994). In this section it is shown how the overpressure dissipates through a homogeneous shale sequence following Darcy law. An alternative model estimating the sealing efficiencies of the pressure compartments is deduced based upon pressure-depth observations. This model is implemented in the PRESSIM simulator and used in the case studies presented in chapter 6.

Table 5.3: Nomenclature, vertical fluid flow

q	Flux $\left(\mathrm{m}^3 \cdot \mathrm{s}^{-1}\right)$
K	Hydraulic conductivity, $K = \frac{\rho g k}{\mu}$ $\left(\mathrm{m} \cdot \mathrm{s}^{-1}\right)$
k	Shale permeability $\left(\mathrm{m}^2\right)$
P	Overpressure (Pa)
S	Specific storage $\left(\mathrm{m}^{-1}\right)$
t	Time (s)
z	Depth (m)
$\bar{z}$	Mean depth to pressure compartment (m)
z_t	Depth to top point of pressure compartment (m)
z_a	Accumulating depth (m)
z_s	Sealing depth (m)
z_{eff}	Effective sealing depth (m) of the pressure compartments
A	Accumulating exponent
f_A	Accumulating factor
h	Thickness of pressure compartment (m)
μ	Viscosity of formation water $\left(\mathrm{kg} \cdot \mathrm{m}^{-1} \cdot \mathrm{s}^{-1}\right)$
$\tilde{c}$	Compressibility of formation water $\left(\mathrm{Pa}^{-1}\right)$
P_H	Hydraulic leak-off pressure (Pa)
σ_1	First order coefficient in the hydraulic leak-off model $\left(\mathrm{Pa} \cdot \mathrm{m}^{-1}\right)$
σ_2	Second order coefficient in the hydraulic leak-off model $\left(\mathrm{Pa} \cdot \mathrm{m}^{-2}\right)$
ρ_w	Density of water $\left(\mathrm{kg} \cdot \mathrm{m}^{-3}\right)$
z_w	Water depth (m)

Darcy flow in shales

Applying the divergence theorem to Darcy law $(\mathbf{q} = K \cdot \nabla \mathbf{P})$ the hydrodynamic equation (5.2) can be deduced where K is the hydraulic conductivity and S is the specific storage of the shales. This equation shows how the overpressure P in a sand sequence dissipates across a shale sequence through time. Equation (5.2) is identical to the one-dimensional heat equation. By using Fourier integrals and assuming that the initial pressure distribution function $f(z)$ across the shale layer is bounded at all depths and integrable in every finite interval, Equation (5.3) can be shown to be the general solution of (5.2).

$$S\frac{\partial P}{\partial t} = \frac{\partial}{\partial z}\left(K\frac{\partial P}{\partial z}\right) \tag{5.2}$$

$$P(z,t) = \frac{1}{\sqrt{\pi}}\int_{-\infty}^{\infty} f\left(z + 2\sqrt{\frac{K}{S}}\xi\sqrt{t}\right)e^{-\xi^2}d\xi \tag{5.3}$$

Figure 5.2 illustrates an example of how a function $P(z,t)$ given in (5.3) behaves in an idealised one-dimensional situation through 8 million years. A 500 m thick shale sequence has a step shaped initial overpressure distribution, where 200 m of the shales are overpressured. The shale permeability is assumed to equal 10^{-22}m^2, the viscosity $2.7\cdot10^{-4}\,\text{kg}\cdot\text{m}^{-1}\cdot\text{s}^{-1}$ and the specific storage $4.41\cdot10^{-10}\,\text{Pa}^{-1}$. Very low shale permeability is chosen in order to illustrate the Darcy properties of a more or less sealing shale layer. Obviously, the thickness of the initial highly pressured sequence dominates the pressure development. Figure 5.3 shows the overpressure dissipation through 16 million years for a similar sequence where only 10 m are overpressured initially. This is however, not a big surprise because Equation (5.2) claims that the change in overpressure through time is proportional to the second derivative of the pressure with regard to the thickness.

Even though the calculations illustrated in Figure 5.2 and Figure 5.3 are highly speculative both with regard to the flow regime and shale permeability, the plots may illustrate how a profile of the overpressure develops through time in a low permeable/sealing shale sequence if Darcy flow takes place in the shales. The pressure dissipation plots in Figure 5.2 and Figure 5.3 are used as a theoretical basis for the finite drainage thickness introduced in the shale compaction model in section 5.2. The pressure dissipation given by the equations (5.2) and (5.3) is not used in the following shale sealing efficiency model or in the PRESSIM simulator used in chapter 6.

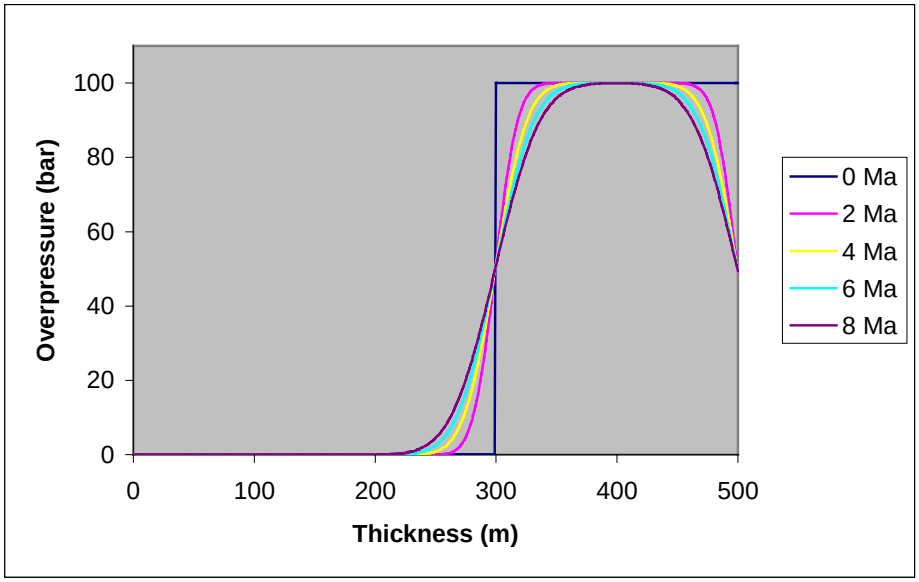

Figure 5.2: Modelled pressure dissipation through an idealised shale sequence where 200 m *of the sequence is initially overpressured*

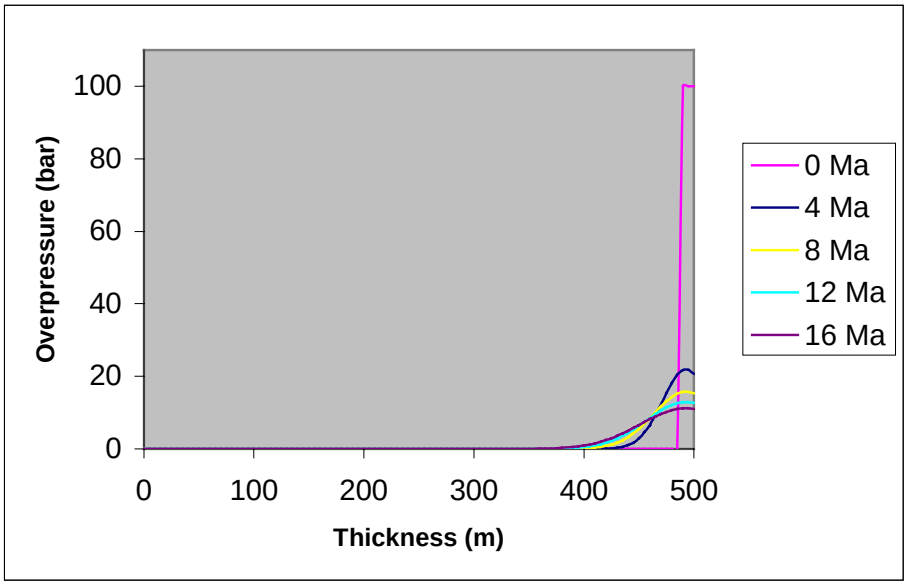

Figure 5.3: Modelled pressure dissipation through an idealised shale sequence where 10 m *of the sequence is initially overpressured*

Sealing efficiency of shales

A simple conceptual model is deduced by describing the sealing effects of the shales instead of applying Darcy law to estimated shale permeabilities. Figure 5.4 shows the simple philosophy behind the vertical fluid flow model deduced in this section. At shallow depths the clay and shale are supposed to be permeable for the formation fluids because of very high porosity. This is the reason why there is no overpressure observed at shallows depths in most sedimentary basin although the temperature increases and the mechanical compaction processes are usually very active at these depths. The transition from the shallow hydrostatic pressure to the deeper close-to-lithostatic pressure can be diffuse. Borge and Sylta (1998) and Darby et al. (1996) noted that in the depth interval 2500 m to 4000 m both hydrostatic and close-to-lithostatic pressures are observed in the North Viking Graben (Figure 5.5) and Central Graben (Figure 5.6), respectively. It is not possible to point out any relation between overpressure and stratigraphy based upon the data plotted in Figure 5.5. The early Cretaceous Cromer Knoll Group pressures are hydrostatic to slightly overpressured while the late Triassic Hegre Group pressures are clearly overpressured. The most interesting observation is that the measured overpressures in the Brent Group, which is the most continuos sand sequence, more or less strictly increase with the depth although the pressure may vary considerably at some depth. Thus lateral communication contributes to establish a pressure-depth relation. The two “steps” on the pressure-depth curve for the Brent Group in Figure 5.5 at 3000 m and 4000 m are caused by different prevailing conditions between lateral and vertical fluid flow. Based upon data from the South Caspian Basin, Bredehoeft et al (1988) draw the same picture: While fluids are expelled vertically through the compacting shales, the sands are acting as lateral drains.

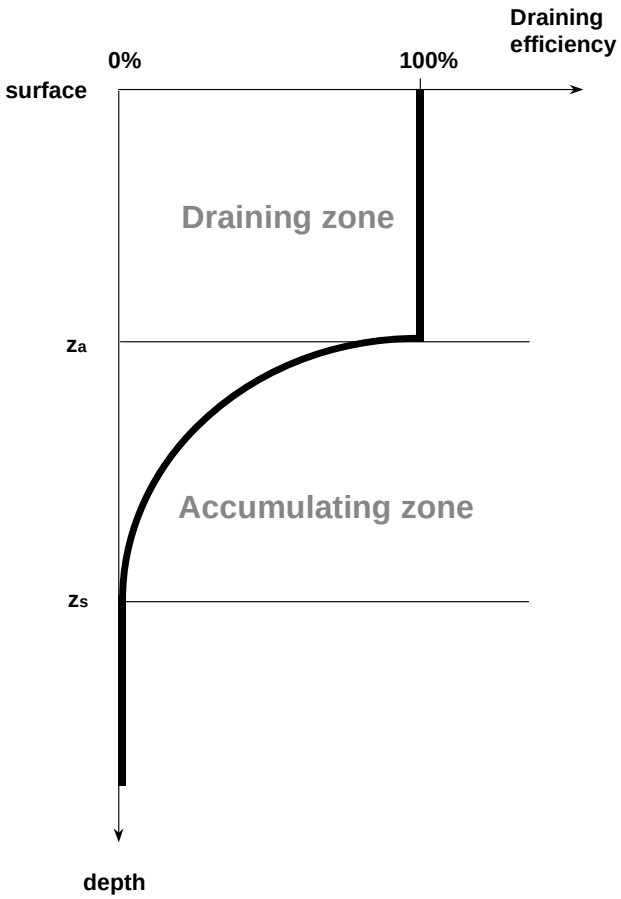

Figure 5.4: *The vertical flow zones in the vertical fluid flow model. The drainage curve illustrates a probable modelled relation between shale sealing and depth.*

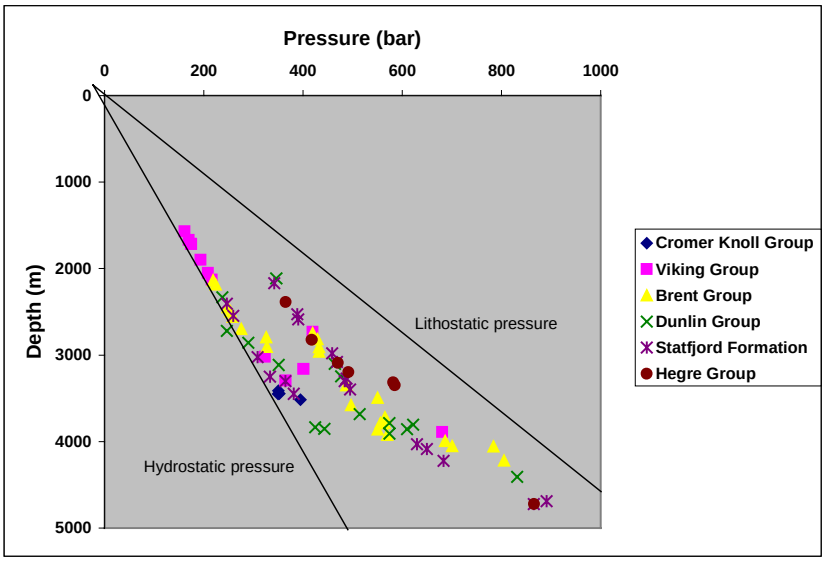

Figure 5.5: Pressure-depth plot for the North Viking Graben (modified from Borge and Sylta (1998))

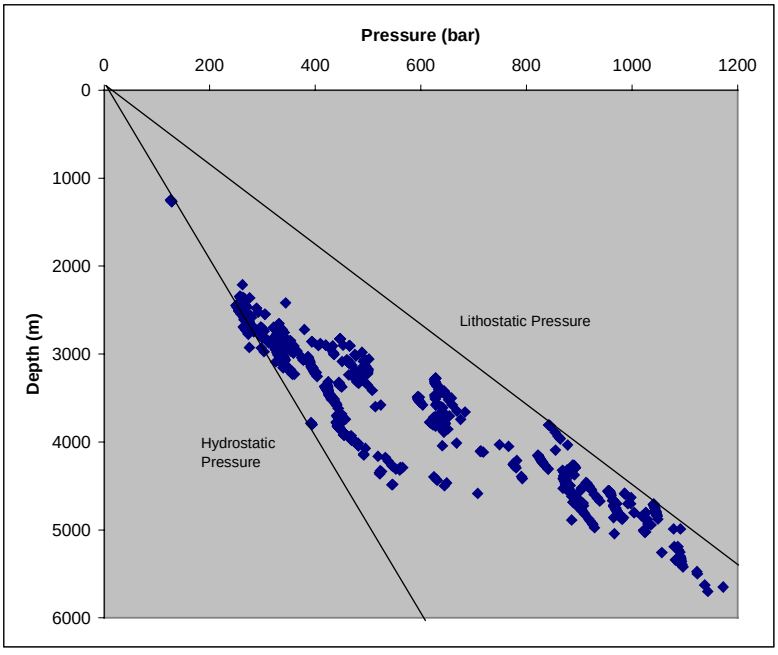

Figure 5.6: Regional pressure-depth plot for UK Central Graben (modified from Darby et al.(1996))

The pressure depth plots in Figure 5.5 and Figure 5.6 demonstrate that the shale gradually becomes sealing. Lateral connectivity and different sealing properties between the pressure compartments are the most probable causes for the great variability in the overpressures in the transition zone. To account for these observations the accumulating zone in Figure 5.4 is introduced. Formation water spilled into cells in this zone will partly be accumulated and partly drained vertically in accordance to (5.4). Below the accumulating zone pore fluids are not allowed to escape through the clay/shale sequences except for the flow caused by hydraulic fracturing. The simple curve in Figure 5.4 shows how much of the net influx that is kept in a pressure compartment and how much that is released vertically as a function of the depth. Equation (5.4) describes the shape of the curve in the accumulating zone. Thus by changing the values of accumulating depth (z_a), sealing depth (z_s) and the accumulating exponent (A) in (5.4) the modelled overpressure in the transition depth interval can be calibrated to fit the observed pressure measurements. However, it may be difficult to estimate an adequate depth z of a pressure compartment that can be used in (5.4). Pressure compartments with identical mean depths may have different sealing properties due to different depth profiles. The relations listed in Table 5.4 suggest an effective drainage depth for the pressure compartments based upon the top- and mean-depth compared to the modelled sealing and accumulating depths of the basin. Since it is the shallowest parts of the pressure compartments that dominate the vertical drainage the mean depth $\bar{z}$ and depth to top point z_t of the pressure compartments are used to determine the effective drainage depth z in (5.4) as listed in Table 5.4. The effective sealing depths listed in the left column in Table 5.4 are supposed to account for the shape of the pressure compartments. The deductions of these depths can be found in Appendix D.1.

$$f_A = \left(\frac{z - z_a}{z_s - z_a} \right)^A \qquad (5.4)$$

Table 5.4: Effective drainage depth of the pressure compartments based upon top-, mean-, accumulating- and sealing depths.

Effective drainage depth	Conditions
$z_{eff} = z_a$	$\bar{z} \le z_a$
$z_{eff} = z_s$	$z_t \ge z_s$
$z_{eff} = \frac{z_t + \bar{z}}{2}$	$(z_t > z_a) \wedge (\bar{z} < z_s)$
$z_{eff} = z_a + \left(\frac{\bar{z} - z_a}{2} \right) \left(\frac{\bar{z} - z_a}{\bar{z} - z_t} \right)$	$(z_t < z_a) \wedge (z_a < \bar{z} < z_s)$

$z_{eff} = z_s - \left(\frac{z_s - z_t}{2}\right)\left(\frac{z_s - z_t}{\overline{z} - z_t}\right)$	$(z_a < z_t < z_s) \wedge (\overline{z} > z_s)$
$z_{eff} = \frac{\overline{z} - z_s}{\overline{z} - z_s + z_a - z_t}\left[z_a + \left(\frac{z_s - z_a}{2}\right)\left(\frac{z_s - z_a}{z_s - z_t}\right)\right] + \frac{z_a - z_t}{\overline{z} - z_s + z_a - z_t}\left[z_s - \left(\frac{z_s - z_a}{2}\right)\left(\frac{z_s - z_a}{\overline{z} - z_a}\right)\right]$	$(z_t < z_a) \wedge (\overline{z} > z_s)$

Traditionally, modelling shale permeabilities has been the crucial point estimating compaction disequilibrium. A plausible reason for this is that currently models of porosity, permeability and pressure evolution in sedimentary basins are based primarily on mechanical compaction related processes (Bjørkum and Nadeau, 1998). Based upon extrapolation of sandstone data Bjørkum and Nadeau (1998) claim that illite precipitation in shales at temperatures of $80-100°\mathrm{C}$ reduces permeability by several orders of magnitude. Although it is not that obvious that Darcy flow takes place in the partly sealing shales it may be convenient to find the corresponding shale permeabilities for the curve outlined in Figure 5.4. Applying the compressibility definition to the part of the formation water that is not drained through the partly sealing shale and then combining it with Darcy's law yields the estimated corresponding permeabilities (5.5). f_A denotes the value of the accumulating factor while ΔP is the hydraulic head across the thickness of the overlying shales in the accumulating zone, ΔL. A complete deduction of (5.5) is presented in Appendix D.2.

$$k = \frac{(1-f_A)(f_A)^{\frac{1-A}{A}}\tilde{c}h\phi\mu(z_s - z_a)(\ln p_2 - \ln p_1)}{t_2 - t_1} \qquad (5.5)$$

In Figure 5.7 the mean effective vertical shale permeabilities estimated by (5.5) for the pressure compartments are plotted against the corresponding accumulating factors given by (5.4). These data are taken from a simulation in the North Viking Graben presented in chapter 6. These results suggest that the shales are turned into seals when the permeabilities decrease from 10^{-22} m^2 to 10^{-23} m^2. These permeabilities correspond well to the data presented by Deming (1994) but are approximately one order of magnitude lower than the analysis done by He and Corrigan (1995). Figure 5.8 shows the same permeability data plotted versus the top depth of the pressure compartments. Differences in the generated overpressure and form of the pressure compartments cause the spreading of the data in Figure 5.8. Thus it is difficult to draw a unique permeability-depth curve for the shales. If the diagenetic effects were included in the models describing the sealing effects of the shales, the spreading would probably have been even larger because the temperature

histories would then have been decisive for the shale permeabilities. In conclusion, the model deduced (Figure 5.4) allows different shale permeability-depth relations and thus corresponds well to the concept of pressure compartments. The main intention behind the estimate of shale permeabilities (5.5) is to demonstrate that the corresponding shale permeabilities plotted in Figure 5.7 and Figure 5.8 do not differ by several orders of magnitude from a Darcy flow model.

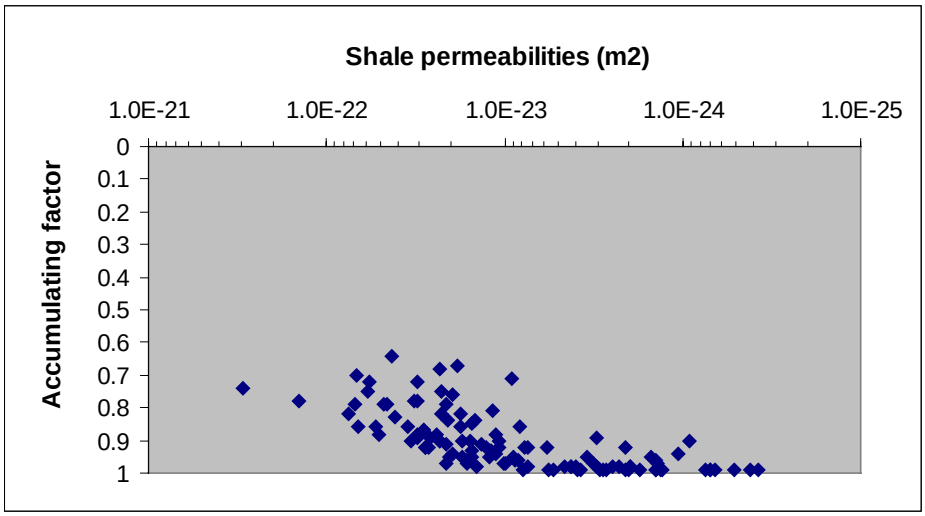

Figure 5.7: Estimated shale permeabilities (m^2) *vs accumulating factors*

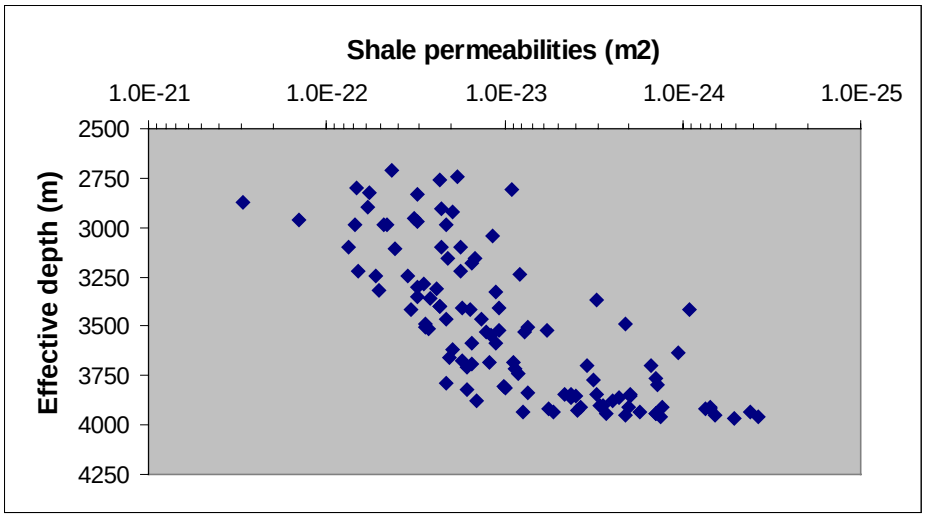

Figure 5.8: Estimated shale permeabilities (m^2) *vs mean depth* (m) *of the pressure compartments*

Hydraulic leakage

If the overpressure in a pressure compartment exceeds the lithostatic pressure the overlying shales will fracture due to the high pressure. The formation water is thus allowed to flow vertically through fractures. This situation occurs if the lateral dissipation is sufficiently small compared to the pressure generation. The model implemented in PRESSIM releases the amount of formation water necessary to keep the pressure at the leak-off pressure. However, most basins leak hydraulically at pressures below the lithostatic pressures. There are several models for describing this phenomenon and Equation (5.6) shows a simple model. Equation (5.6) describes a second order curve for the hydraulic leak-off pressure – a quite common situation for sedimentary basins. The last term in (5.6) represents the weight of the water column above the seabed.

$$P_H = \sigma_2 z^2 + \sigma_1 z + \rho_w g z_w \qquad (5.6)$$

If hydraulic fracturing occurs in a multi-layer model, the amount of hydraulically leaked formation water will be forced into the overlying formation generating an additional contribution of overpressure. By this way overpressure generated in one of the lower layers may find its way through several overlying formations.

5.2 Generation of overpressure

There are several mechanisms that may contribute to build abnormally high pressure in sedimentary basins and the importance of these processes is highly debated. The most common candidates for generation of overpressure are:

- diagenesis of smectite to illite in shales
- hydrocarbon generation
- thermal expansion of water
- mechanical compaction of sediments
- quartz cementation in sandstones
- horizontal loading by tectonic stresses

Abnormally high pressures have been detected in many different geological settings (Neuzil, 1995) thus the dominating pressure generating mechanism may vary between basins, within basins and through time. Mechanical compaction is controlled by effective stress and seems to be a probable source for the observed overpressure according to several authors (Mann and Mackenzie, 1990, Hall, 1994 and Osborne and Swarbrick, 1997). Quartz cementation in sandstones is, in contradiction to mechanical compaction, controlled by temperature. Quartz cementation has been recognised as the main cause of porosity loss

in many deeply buried quartzose sandstone reservoirs in various basins (Walderhaug, 1996). There seems to be a rather good agreement that the pressure generating effects caused by smectite to illite transformation (Osborne and Swarbrick, 1997) and thermal expansion of water (Hall, 1994, Luo and Vasseur, 1992 and Osborne and Swarbrick, 1997) are of minor importance to most basins.

Simple empirical models for mechanical compaction and quartz cementation are described in this section and included into the PRESSIM simulator as the pressure generating mechanisms. These processes quantify the porosity loss and the subsequent pressure generation in the pressure compartments. Both the shales and sands are compacted using these two mechanisms to estimate the change in porosity. Although some of the mechanisms listed above that are not included in the model may contribute to the generation of overpressure, the empirical models for quartz cementation and mechanical compaction will probably account for these contributions. The timing of the pressure generation is important because the pressure simulation is modelled on a geological time scale. Using both the stress dependent mechanical compaction and the temperature dependent chemical compaction the PRESSIM simulator is able to generate overpressure in periods without subsidence.

The amount of porosity loss within all the pressure compartments is estimated consecutive in time steps. It is thus necessary to model the physical behaviour of the formation water. Simple empirical models for compressibility and viscosity as a function of pressure, salinity and temperature are deduced in this section. Table 5.5 lists the nomenclature used in the models describing generation of overpressure.

Table 5.5: Nomenclature used for modelling pressure generation

$\tilde{c}$	Compressibility of formation water $\left(\mathrm{Pa}^{-1}\right)$
T	Temperature $\left(^{\circ}\mathrm{C}\right)$
T_0	Temperature at the bottom of the sea $\left(^{\circ}\mathrm{C}\right)$
$\left(\frac{\partial T}{\partial z}\right)$	Temperature gradient of the basin $\left(^{\circ}\mathrm{C}\cdot\mathrm{m}^{-1}\right)$
s	Salinity $\left(\mathrm{ppm}\right)$
μ	Viscosity $\left(\mathrm{kg}\cdot\mathrm{m}^{-1}\cdot\mathrm{s}^{-1}=10^{3}\mathrm{cp}\right)$
z	Depth $\left(\mathrm{m}\right)$
γ	Shale drainage thickness $\left(\mathrm{m}\right)$
h	Mean thickness of pressure compartment $\left(\mathrm{m}\right)$
$\tilde{A}$	Area of pressure compartment $\left(\mathrm{m}^{2}\right)$

f_σ	Stress dependency factor
P_H	Hydrostatic pressure (Pa)
P_L	Lithostatic pressure (Pa)
V_q	Volume of precipitated quartz cement (m^3)
V	Volume of present sandstone (m^3)
V_c	Volume of sandstone when quartz precipitation starts/started (m^3)
M	Molar mass of quartz $(60.09\ \mathrm{g \cdot mole^{-1}})$
r	Rate of quartz precipitation $(\mathrm{mole \cdot m^{-2} \cdot s^{-1}})$
r_1	Quartz precipitation rate constant $(1.98 \cdot 10^{-18} \mathrm{mole \cdot m^{-2} \cdot s^{-1}})$
r_2	Quartz precipitation rate constant $(0.022^\circ \mathrm{C}^{-1})$
ϕ_{C0}	Porosity when quartz cement precipitation starts
ϕ_{C1}	Porosity not accessible for quartz cementation
ϕ_{S0}	Sand-porosity at seabed
η_1	Porosity-depth constant 1 (m)
η_2	Porosity-depth constant 2
A_c	Quartz surface area when quartz cement precipitation starts (m^2)
A	Quartz surface area (m^2)
C	Clay coating factor
D	Diameter of grains (m)
t	Time (s)
ρ	Density of quartz $(2650\ \mathrm{kg \cdot m^{-3}})$
f	Fraction of detrital quartz when quartz cement precipitation starts
T_{C0}	Temperature where quartz cementation starts $(^\circ \mathrm{C})$
T_{C1}	Temperature (approximately) where quartz cementation is completed $(^\circ \mathrm{C})$
z_{C0}	Depth where quartz cementation starts (m)
z_{C1}	Depth where quartz cementation is finished (m)
z_t	Depth to top point of pressure compartment (m)
z_m	Mean depth to pressure compartment (m)
z_b	Depth to bottom point of pressure compartment (m)

Properties of the formation water

The definition of compressibility given in Equation (5.7) provides a simple and useful relation between porosity loss and increase in pressure. In order to be able to model the generation of overpressure it is necessary to know the compressibility of the pore water.

However, very few simple models for compressibility of brine that include the temperature and pressure ranges in a compacting sedimentary basin are published. The simple model (5.8) is used for calculating the temperature in the basin. The same surface temperature and thermal gradient are used all over the basin.

$$\tilde{c} = -\frac{1}{V}\frac{dV}{dP} \qquad (5.7)$$

$$T = T_0 + \frac{\partial T}{\partial z} z \qquad (5.8)$$

Standing (1974) published some compressibility curves including a correction due to dissolved salts. These measurements cover temperatures between $40°\mathrm{C}$ and $170°\mathrm{C}$ and pressures between 100 bar and 700 bar, approximately. The Equations (5.9), (5.10) and (5.11) attempt to describe and extrapolate these curves for basin modelling purposes. Figure 5.9 and Figure 5.10 show the compressibility curves given by these equations for a selection of pressures and salinities typical for sedimentary basins. The compressibility model is visually adjusted to fit Standing's data (1974) and not by applying a certain mathematical procedure. c denotes the compressibility of water and is given in $10^{-12}\,\mathrm{Pa}^{-1}$ while $\varsigma(s,T)$ is the factor which accounts for changes in the compressibility due to salinity. The salinity has the unit ppm. Compressibilities estimated by model (5.9) - (5.11) are compared to literature data compiled and evaluated by Rogers and Pitzer (1982) listed in Table 5.6. In average the deviations are about 4 % but excluding compressibilities from temperatures higher than $200°\mathrm{C}$ the average deviation is about 1 %. It is advantageous to obtain the best fit for the low compressibility values because according to Equation (5.7) the small compressibilities result in the largest contributions to the overpressure. The compressibility model represented by (5.9), (5.10) and (5.11) is valid for temperatures between $40°\mathrm{C}$ and $300°\mathrm{C}$ and pressures between 100 bar and 1000 bar, approximately.

$$\tilde{c}(P,s,T) = \varsigma(s,T)\begin{cases} 0.0127\left(T-\frac{340}{9}\right)^2 - 1.262\cdot 10^{-6}P + 439.4 & T < 143.3°\mathrm{C} \\ 0.0127\left(T-\frac{340}{9}\right)^2 + 387.2 - 1.262\cdot 10^{-6}\left(P - 41.37\cdot 10^6\right)\left(\frac{3}{100}T - 3.3\right) & T > 143.3°\mathrm{C} \end{cases} \qquad (5.9)$$

$$\varsigma(s,T) = \begin{cases} 1.0 - 1.45\cdot 10^{-6}s - 1.59\cdot 10^{-6}(T-65.6)^2 & 0 < s \le 5\cdot 10^4 \\ 1.0 - 1.45\cdot 10^{-6}s - 4.11\cdot 10^{-6}(T-65.6)^2 & 5\cdot 10^4 < s \le 1\cdot 10^5 \\ 0.9475 - 9.25\cdot 10^{-7}s - 5.10\cdot 10^{-6}(T-65.6)^2 & 1\cdot 10^5 < s \le 3\cdot 10^5 \end{cases} \quad T < 170°\mathrm{C} \qquad (5.10)$$

$$\varsigma(s,T)=\begin{cases}0.983-1.45\cdot10^{-6}s-0.09\cdot10^{-4}(T-170.0) & 0<s\le5\cdot10^{4}\\ 0.955-1.45\cdot10^{-6}s-1.80\cdot10^{-4}(T-170.0) & 5\cdot10^{4}<s\le1\cdot10^{5}\\ 0.892-9.25\cdot10^{-7}s-2.22\cdot10^{-4}(T-170.0) & 1\cdot10^{5}<s\le3\cdot10^{5}\end{cases}\quad T>170°\mathrm{C} \qquad (5.11)$$

The viscosity of brine as a function of temperature is given by Equation (5.12) in centipoise (cp). This model is based upon an extrapolation of data from Standing (1974) similar to those made for deducing the compressibility model. This viscosity model should not be used for temperatures below $70°\mathrm{C}$. Viscosity curves are plotted versus the temperature for some typical salinity values in Figure 5.11.

$$\mu(s,T)=\frac{1.3}{0.04T+0.6}+\left(3.0\cdot10^{-7}s+2.0\cdot10^{-12}s^{2}\right) \qquad (5.12)$$

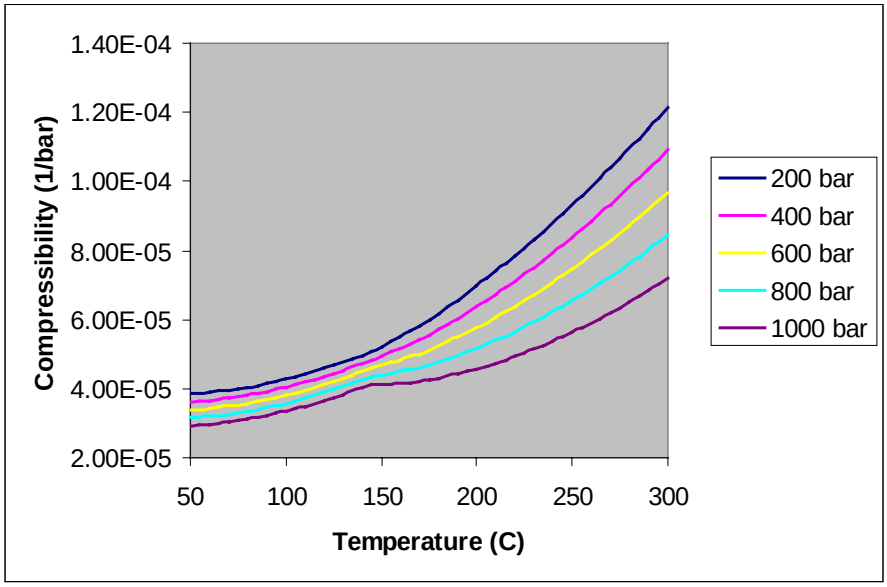

Figure 5.9: *Compressibility curves for some typical pressure values. The salinity is* 50000 ppm.

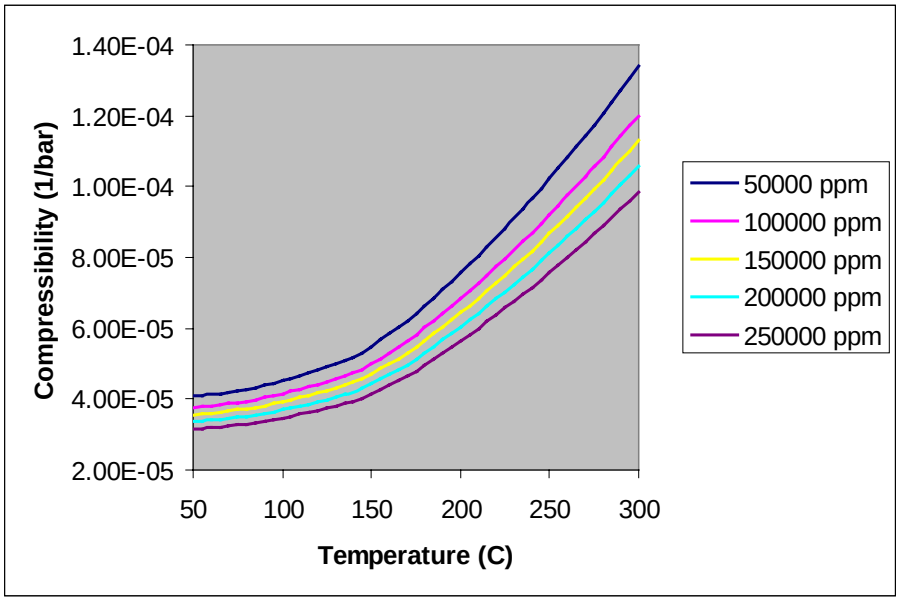

Figure 5.10: *Compressibility curves for some typical salinity values. The pressure is* 400 bar.

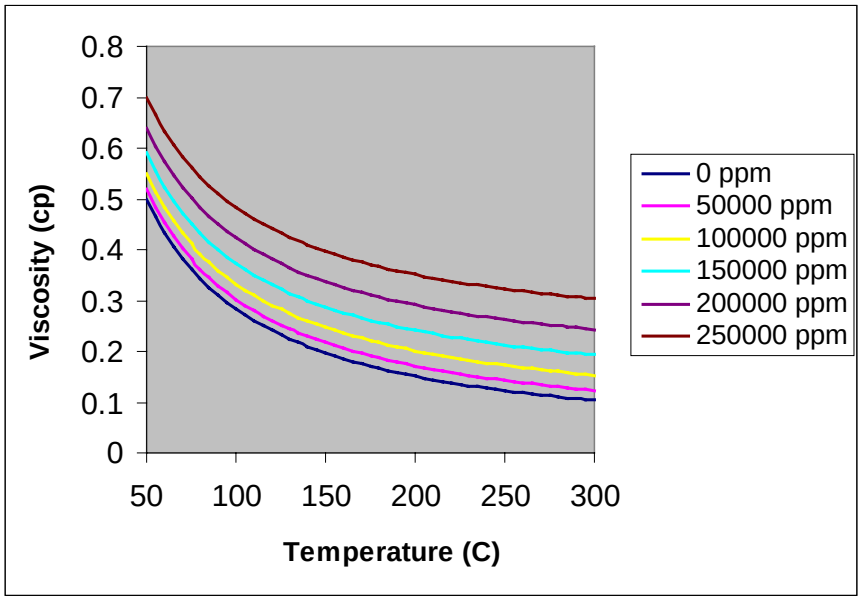

Figure 5.11: *Plot showing the viscosity versus temperature for some typical salinity values.*

It may seem unnecessary to deduce models describing the compressibility and viscosity of the formation fluid as a function of pressure, temperature and salinity if one can choose a constant compressibility and viscosity. Table 5.7 shows the increase in overpressure when an amount of brine is compacted by 1% at conditions prevailing at 2000 m, 4000 m and 6000 m depths. The differences in the resulting increases in overpressure are quite large. This simple example clearly illustrates that the formation water compacts more easily with increasing depths.

Equation (5.7) can be reformulated to the more convenient form (5.13). This expression gives the increase in overpressure as a function of net in- or outflux, volume of pressure cell, compressibility and viscosity.

$$\Delta P = \frac{\Delta V}{\tilde{c}(P,s,T)\cdot V} \qquad (5.13)$$

Table 5.6: The modelled compressibilities (5th column) compared to the data from Rogers and Pitzer (1982).

Pressure (bar)	Temperature (°C)	Salinity (ppm)	Rogers and Pitzer (Pa^{-1})	Modelled compressibilities (Pa^{-1})	Deviation (%)
200	100	10000	4.5E-10	4.6E-10	-1.3
200	100	25000	4.5E-10	4.5E-10	1
200	100	50000	4.4E-10	4.3E-10	2.8
200	100	75000	4.3E-10	4.1E-10	4.5
200	100	100000	4.2E-10	3.9E-10	6.3
400	100	10000	4.3E-10	4.3E-10	-0.2
400	100	25000	4.2E-10	4.2E-10	-0.3
400	100	50000	4.1E-10	4.0E-10	1.4
400	100	75000	4.1E-10	3.9E-10	5.3
400	100	100000	4.0E-10	3.7E-10	7
400	150	10000	5.2E-10	5.4E-10	-2.9
400	150	25000	5.1E-10	5.2E-10	-2.6
400	150	50000	5.0E-10	4.9E-10	1.3
400	150	75000	4.9E-10	4.7E-10	3.4
400	150	100000	4.8E-10	4.5E-10	6.3
600	100	10000	4.0E-10	4.1E-10	-1.5
600	100	25000	4.0E-10	4.0E-10	0.7
600	100	50000	3.9E-10	3.8E-10	2.3

600	100	75000	3.8E-10	3.7E-10	3.7
600	100	100000	3.8E-10	3.5E-10	7.8
600	150	10000	4.8E-10	5.1E-10	-5.3
600	150	25000	4.7E-10	4.9E-10	-5.2
600	150	50000	4.6E-10	4.7E-10	-1.3
600	150	75000	4.5E-10	4.5E-10	0.6
600	150	100000	4.4E-10	4.2E-10	3.4
600	200	10000	6.1E-10	6.4E-10	-4.4
600	200	25000	6.0E-10	6.2E-10	-3.8
600	200	50000	5.8E-10	5.8E-10	0.5
600	200	75000	5.7E-10	5.5E-10	2.9
600	200	100000	5.5E-10	5.2E-10	5.2
800	150	10000	4.5E-10	4.8E-10	-5.8
800	150	25000	4.4E-10	4.7E-10	-5.8
800	150	50000	4.3E-10	4.4E-10	-2.1
800	150	75000	4.2E-10	4.2E-10	-0.3
800	150	100000	4.0E-10	4.0E-10	0
800	200	10000	5.6E-10	5.7E-10	-2
800	200	25000	5.5E-10	5.6E-10	-1.5
800	200	50000	5.3E-10	5.2E-10	2.4
800	200	75000	5.1E-10	5.0E-10	2.8
800	200	100000	4.9E-10	4.7E-10	4.6
800	250	10000	7.5E-10	7.3E-10	2.7
800	250	25000	7.3E-10	7.1E-10	2.2
800	250	50000	7.0E-10	6.5E-10	6.4
800	250	75000	6.7E-10	6.3E-10	6.3
800	250	100000	6.4E-10	5.9E-10	7.8
800	300	10000	1.1E-09	9.5E-10	11.2
800	300	25000	1.0E-09	9.3E-10	10.7
800	300	50000	9.9E-10	8.4E-10	14.7
800	300	75000	9.6E-10	8.1E-10	15.8
800	300	100000	9.2E-10	7.6E-10	17.7
1000	200	10000	5.2E-10	5.1E-10	2.9
1000	200	25000	5.0E-10	4.9E-10	1.3
1000	200	50000	4.8E-10	4.6E-10	4.7
1000	200	75000	4.6E-10	4.4E-10	4.6
1000	200	100000	4.4E-10	4.1E-10	6
1000	250	10000	6.7E-10	6.3E-10	6.3

1000	250	25000	6.5E-10	6.1E-10	5.6
1000	250	50000	6.1E-10	5.6E-10	7.7
1000	250	75000	5.8E-10	5.4E-10	7
1000	250	100000	5.5E-10	5.1E-10	7.8
1000	300	10000	9.2E-10	8.1E-10	11.8
1000	300	25000	8.9E-10	7.9E-10	10.9
1000	300	50000	8.4E-10	7.2E-10	14.2
1000	300	75000	7.9E-10	6.9E-10	12.6
1000	300	10000	7.6E-10	6.5E-10	15

Table 5.7: Compaction data for brine (25000 ppm *NaCl), 1% compaction*

Pressure (bar)	Temperature (°C)	Compressibility (Pa^{-1})	ΔP (bar)
200.0	80	$4.3 \cdot 10^{-5}$	233
400.0	150	$5.1 \cdot 10^{-5}$	196
600.0	220	$6.8 \cdot 10^{-5}$	147

Compaction of shale

The easiest applicable method in practice to model compaction is to use empirical porosity-depth curves, which are based on samples from several basins around the world (Rivenæs, 1993). Baldwin and Butler (1985) formulated Equation (5.14) and (5.15) which describe the porosity-depth trends in hydrostatically pressured shales and in overpressured shales, respectively. These two porosity curves are plotted in Figure 5.12. It is assumed that the difference in porosity between normal pressured and overpressured shales represents the net volume of formation water squeezed out of the shales into the reservoirs due to compaction. The remaining part of the compaction water is assumed to be able to drain out of the basin without contributing to pressure generation. Shales that are 200 m or more in thickness do not lose pore water readily (Baldwin and Butler, 1985). It is thus assumed that an under- and overlying shale sequences of thickness γ expel pore fluid into the sands/reservoirs. Assuming that the compressibility of the clay minerals is negligible, the decrease in pore space represents an expulsion of fluid from the clays (Bredehoeft et al, 1988). Equation (5.16) estimates the net volume of formation fluids expelled from over- and underlying shales into a reservoir pressure compartment during the subsidence Δz (see Appendix D.3).

$$\phi_h(z) = 1 - \left(\frac{z}{6020}\right)^{0.15748} \qquad (5.14)$$

$$\phi_p(z) = 1 - \left(\frac{z}{15000}\right)^{\frac{1}{8}} \qquad (5.15)$$

$$\Delta V = 2\gamma\tilde{A}\left[\phi_p'(z) - \phi_h'(z)\right]\Delta z \qquad (5.16)$$

The amount of water flowing into the sands due to the compacting shales is reduced if the sands are overpressured. To account for this effect the stress dependency factor (5.17) is multiplied with the volume of expelled water (5.16). The factor (5.17) is close to one under hydrostatic conditions and close to zero if the pressure approach the lithostatic level. Thus accumulated overpressure will contribute to preserve the porosity of the over- and underlying shales in accordance with the curves plotted in Figure 5.12.

$$f_\sigma = \left(1 - \frac{P - P_H}{P_L - P_H}\right) \qquad (5.17)$$

Integrating the factor (5.17) multiplied with ΔP in (5.13) (ΔV is provided by (5.16)) from a depth z_0 to z_1 results in (5.18) which estimates the increase in overpressure, where P_0 is the overpressure at z_0 and P_L is the lithostatic pressure. This integration is carried out in Appendix D.3. The contribution from (5.18) is only included if the subsidence represents a loading beyond the previous maximum effective stress. Unloading and reloading below the maximum effective stress result in a much smaller change to the porosity than the rate of decrease on initial loading (Hall, 1994).

$$\begin{aligned} \Delta P &= \left(P_L - P_H - P_0\right)\left(1 - e^{-\chi}\right) \\ \chi &= \frac{2\gamma}{\tilde{c}h\phi(P_L - P_H)}\left[\left(\phi_p(z_1) - \phi_h(z_1)\right) - \left(\phi_p(z_0) - \phi_h(z_0)\right)\right] \end{aligned} \qquad (5.18)$$

Hansen (1996) concludes that it is questionable whether the compaction trend found studying Cretaceous and Tertiary shales on the Norwegian Shelf should be applied to shales buried deeper than 2600 m. Due to diagenetic changes the mechanical compaction of shales probably gradually decreases at large depths. Hermanrud et. al (1998) conclude that density and sonic log data from both the Haltenbanken and the North Sea do not discriminate between highly overpressured and normally pressured shales. Diagenetic reactions rather than mechanical compaction at large depths may dominate the reduction of porosity in shale (Olav Walderhaug, pers. comm.). This does not necessarily mean that the presented shale undercompaction model predicts wrong amounts of formation water expelled from the shales and into the sands applying the models to the Norwegian continental shelf. In contradiction to the referred data from the Haltenbanken area,

Bredehoeft et. al. (1988) and Gordon and Flemmings (1998) show shale porosity-depth plots that convincingly demonstrate shale undercompaction in the South Caspian basin and Eugene Island 330 (offshore Louisiana), respectively.

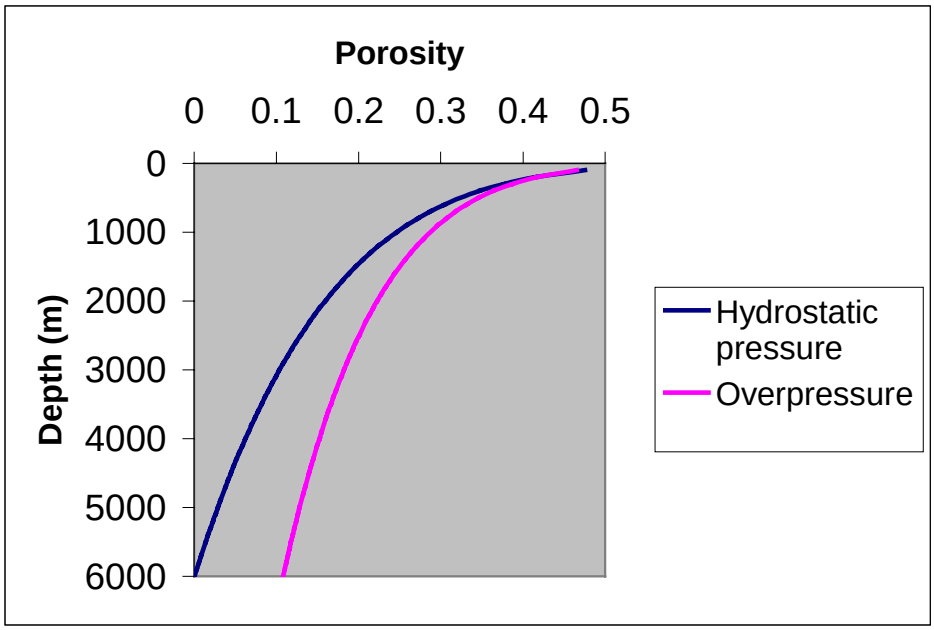

Figure 5.12: Porosity-depth trends for hydraulically pressured and overpressured shales (after Baldwin and Butler (1985)).

Compaction of sand

Quartz cementation leads to porosity loss in sand reservoirs and thus may become an important source of overpressure. The mathematically simple kinetic model (5.19), (5.20), (5.21) and (5.22), which simulates quartz cementation and the resulting porosity loss in quartzose sandstones as a function of temperature history (Walderhaug, 1996), is chosen for this purpose. The quartz cementation model is implemented into the PRESSIM simulator (see Appendix B) that models fluid flow numerically applying time steps less than 1 million years. It is thus sufficient to update the quartz surface area A and the temperature T at each time step, rather than integrating (5.19) and using a temperature-depth relation in (5.20).

$$V_q = \frac{MrAt}{\rho} \cdot V \qquad (5.19)$$

$$r = r_1 10^{r_2 T} \tag{5.20}$$

$$A = (1-C) A_c \frac{\left(\phi_{C0} - \frac{V_q}{V}\right)}{\phi_{C0}} \tag{5.21}$$

$$A_c = \frac{6 f V_c}{D} \tag{5.22}$$

If sufficient geological data and satisfactory models are available it is desirable to define the fraction of detrital quartz when quartz cement precipitation starts (f), the diameter of grains (D) and the porosity when quartz cement precipitation starts (ϕ_{C0}) over the entire basin and specify values for these variables in each pressure compartment. In the absence of such models f, D and ϕ_{C0} are treated as regional parameters which have the same value all over the basin. Walderhaug (1996) suggests the values for the quartz precipitation rate constants r_1 and r_2 in Table 5.5. The modelled volume of precipitated quartz cement V_q given by (5.19) is, in each time step, used as ΔV in Equation (5.13) and thus overpressure is generated internally in the pressure compartments.

Following the outlined model the quartz cementation process will cement all the pore space and thus cause the denominator in (5.13) to become very small and numerical problems will most probably occur due to large pressure changes in the cells with very low remaining porosity. In order to avoid these numerical problems the formula describing quartz surface area (5.21) is slightly modified by including irreducible water for the cementation process. Assuming porosities between 1 and 5 % are more or less inaccessible for the quartz cementation process may be reasonable in many cases (Olav Walderhaug, pers. comm.). Petrographic studies of deeply buried Jurassic North Sea sandstones show that sandstones with microcrystalline quartz coatings have well-preserved porosities (Wangen, 1998). Thus (5.19) and (5.21) are modified and implemented into PRESSIM as (5.23) and (5.24), respectively.

$$V_q = \frac{MrAt}{\rho} \cdot V \tag{5.23}$$

$$A = (1-C) A_c \frac{\left(\phi_{C0} - \phi_{C1} - \frac{V_q}{V}\right)}{\phi_{C0}} \tag{5.24}$$

Applying the starting temperature T_{C0} for the quartz cementation to the thermal model (5.8) estimates the depth (5.25) where the quartz precipitation starts. Above this depth the empirical model for mechanical compaction of sand (5.26) given by Robinson and Gluyas (1992) is used to estimate the porosity in the sands/reservoirs. Below the depth (5.25) only chemical compaction is modelled because the quartz cement make the sandstone hard and brittle. Probably, the transition from mechanical to chemical compaction as the prevailing porosity reducing mechanism gradually takes place over a specific range of depth. However, this change is more or less finished before the pressure compartments subside into the accumulating zone described in section 5.1. Thus this simplification causes only minor consequences to the modelled overpressure. A considerable part of the pressure compartments are usually buried below the depth z_{C0}. It is thus necessary to estimate the porosities for these compartments at the beginning of the simulation although the temperature histories are not known. Equation (5.27) describes how the initial porosity is defined for the pressure compartments below z_{C0}. This simple porosity-depth relation for quartz cemented sands is found by drawing a straight line between the porosity ϕ_{C0} at depth z_{C0} and the irreducible porosity ϕ_{C1} at depth z_{C1}. Compared to the porosity depth curves presented by Bjørkum et. al (1998a), Equation (5.27) estimates the porosity depth relation relatively well.

$$z_{C0} = \frac{T_{C0} - T_0}{\partial T / \partial z} \tag{5.25}$$

$$\phi = \phi_{S0} e^{-\frac{z}{\eta_1 + \eta_2 z}} \tag{5.26}$$

$$\begin{aligned} \phi &= \frac{\phi_{C0} - \phi_{C1}}{z_{C1} - z_{C0}}\left(z + z_{C0}\right) + \phi_{C0} \qquad z_{C0} < z < z_{C1} \\ \phi &= \phi_{C1} \qquad\qquad\qquad\qquad\qquad\qquad z \geq z_{C1} \end{aligned} \tag{5.27}$$

The vertical depth from the top to the bottom of a pressure compartment may be relatively large. The porosity is modelled at the top-, mean- and bottom depth of each pressure cell as outlined in Figure 5.13. The lower part may be completely cemented while the upper part may be located at the top of the quartz cementation window. By simulating the compaction at these three points the quartz cementation is modelled much more realistically for the whole compartment and the transition from mechanical to chemical compaction are smoothened. Estimating the total cemented pore volume in each time step the same weighting of the top-, middle- and bottom-depth is used as for the sand porosities in Equation (5.28).

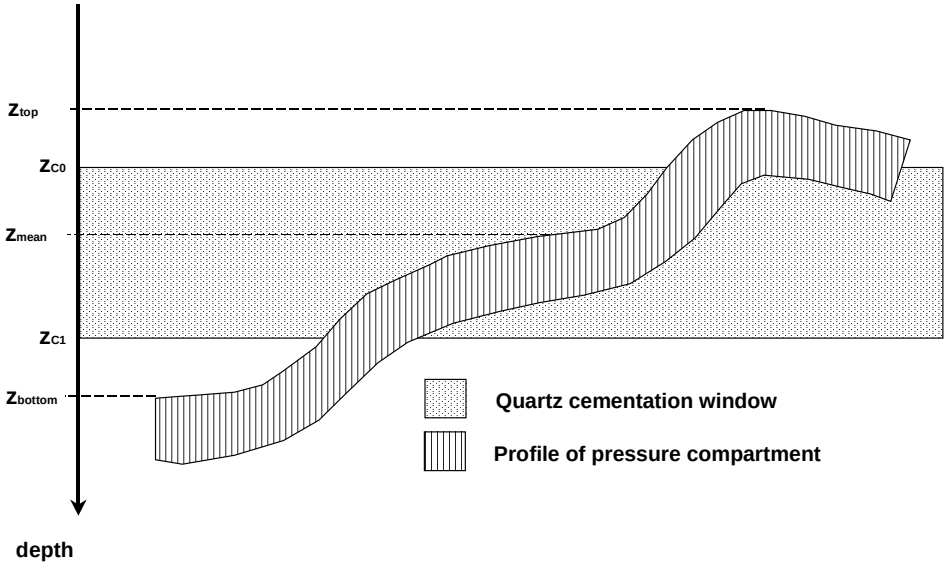

Figure 5.13: Schematic illustration of the profile of a pressure compartment and its depths related to the interval of quartz cementation.

Estimation of porosity

It is very important to model a realistic mean porosity of the pressure compartments. The porosity influences both the generation and dissipation of the overpressure since the porosity governs the volume of the formation water in Equation (5.13). Due to the net/gross consideration of the pressure compartments both the shale and sand porosities are included in the porosity function. While the shale porosities are averaged over the three depths in Figure 5.13, the weights of the sand porosities depend upon how much of the compartments that has subsided below the quartz cementation window. The Equation (5.28) shows how the porosities of the compartments are estimated based upon net gross ratio, top-, mean- and bottom-depth.

$$\bar{\phi}=\begin{cases}\dfrac{ng}{6(z_b-z_t)}\left((z_m-z_t)\phi_t+(z_b-z_t)\phi_m+(2z_b-z_{C2}-z_m)\phi_b\right) & \\ \quad+\dfrac{1-ng}{3}\left(\phi_p(z_t)+\phi_p(z_m)+\phi_p(z_b)\right) & (z_b>z_{C1})\wedge(z_m<z_{C1}) \\ \dfrac{ng}{6(z_b-z_t)}\left((z_{C1}-z_t)\phi_t+(z_b+z_m-z_t-z_{C1})\phi_m+(z_b-z_m)\phi_b\right) & \\ \quad+\dfrac{1-ng}{3}\left(\phi_p(z_t)+\phi_p(z_m)+\phi_p(z_b)\right) & (z_m>z_{C1})\wedge(z_t<z_{C1}) \\ \dfrac{ng}{3}\left(\phi_t+\phi_m+\phi_b\right)+\dfrac{1-ng}{3}\left(\phi_p(z_t)+\phi_p(z_m)+\phi_p(z_b)\right) & (z_b<z_{C1})\vee(z_t>z_{C1})\end{cases} \quad (5.28)$$

5.3 A numerical model describing pressure dissipation

In order to deduce a simple numerical model describing pressure dissipation Equation (5.7) is reorganised as (5.29).

$$\frac{dP}{dt}=-\frac{1}{\tilde{c}V}\frac{dV}{dt} \qquad (5.29)$$

Since $\mu\cdot\dfrac{d\mathbf{V}}{dt}=A\mathbf{p}$ the change in overpressure can be related to the matrix product $A\mathbf{p}$ as expressed in (5.30). Reorganising this expression to the incremental form (5.31) clearly shows that the discretisation correspond to the explicit forward Euler solution technique. By updating the pressures in the last term in (5.31) it is possible to reformulate this expression to the implicit backward Euler technique as shown in (5.32).

$$\frac{\Delta\mathbf{P}}{\Delta t}=-\frac{1}{\tilde{c}\mu V}A\mathbf{p} \qquad (5.30)$$

$$\mathbf{p}_{n+1}=\mathbf{p}_n-\Delta t\frac{1}{\tilde{c}\mu V_n}A\mathbf{p}_n \qquad (5.31)$$

$$\left(I+\Delta t\frac{1}{\tilde{c}\mu V_n}A\right)\mathbf{p}_{n+1}=\mathbf{p}_n \qquad (5.32)$$

The left side of (5.30) represents the derivative of the pressure with regard to time while the summation sign on the right side represent the second derivative related to space.

Principally, Equation (5.30) can be written as (5.33), which is a parabolic differential equation.

$$u_t + cu_{xx} = 0 \qquad (5.33)$$

The explicit forward Euler formulation (5.31) is implemented into the PRESSIM simulator (see Appendix B) to solve the system of parabolic differential equations because this is the simplest solution technique. It is neither necessary to invert a matrix nor to solve a system of linear equations numerically in order to find the pressure $\mathbf{p}_{n+1}$. However, this method is an unstable method. In order to stabilise the method the criterion (5.34) is used. This criterion ensures that the change in overpressure do not exceed the overpressure itself and thus prevents that an unstable situation occurs where the overpressures are oscillating between extremely high and low values. If this measure is exceeded the time step Δt is chopped to the half of its value. The chopping criterion (5.34) and the chosen halving strategy may cause the time steps to become too short. If this is due to high transmissibilities in general the simulation is rightly interrupted. Small pressure compartments with low permeabilities and a relative large flux passing through result in high values of the fraction in (5.34). In order to avoid that small compartments slow down the simulations a minimum dissipation volume (i. e. a minimum volume for V_i in (5.34)) is introduced. This minimum volume normally does not affect the basin wide pressure distribution significantly, but it smoothes the variations in the small cells and thus speeds up the simulations.

$$\max_i \left| \frac{\frac{\Delta t}{\tilde{c}_i V_i} \sum_{j=1}^{N} a_{ij} P_j^{(k)}}{P_i^{(k)} + 10.0} \right| < 1 \qquad (5.34)$$

If the explicit forward Euler solution technique is forced to used excessively small time steps compared to the smoothness of the overpressure vs. time curves, the system is said to be stiff (Lambert, 1991). The stiffness causes an exaggerated long time for the computer to solve the system. It is worse, however, if the stiffness leads to inconsistency between the method and the system. This means that the numerical method solves another system of equations than specified when the lengths of the time steps become excessively small. Thus overpressure may appear or disappear due to numerical difficulties. Although some of the case studies presented in the next chapter tend to be stiff it does not seem that inconsistency is a problem. However, the easiest way to handle stiffness and inconsistency is to apply the stable implicit backward Euler technique (5.32) to the lateral pressure dissipation.

Single layer model

Equation (5.35) shows how the forward Euler technique (5.31) is implemented for a single layer model, and how the overpressure in a pressure compartment is distributed/dissipated to its neighbours. The elements a_{ij} belong to a symmetric matrix similar to the one outlined in (3.5).

$$\frac{1}{\Delta t}\Delta P_i = -\frac{1}{\tilde{c}_i \mu_i V_i}\sum_{j=1}^{N} a_{ij} P_j \qquad i = 1,\ldots,N \tag{5.35}$$

Multi layer model

Dealing with more than one reservoir, the numerical scheme that calculates dissipation of overpressure becomes slightly more complicated. Equation (5.36) is used to estimate the volume of formation water flow into or out of a pressure compartment across the faults in a multi-layer model describing M layers. Equation (5.36) describes a system of linear equations $A\mathbf{p} = \Delta\mathbf{V}$ where $A \in \mathrm{R}^{(MN)\times(MN)}$ and $\mathbf{p}, \Delta\mathbf{V} \in \mathrm{R}^{MN}$.

$$\begin{aligned} &\sum_{l=1}^{M}\sum_{j=1}^{N}\left(P_{ik} - P_{jl}\right)T_{ijkl} = \Delta\mathbf{V}_{ik} && i = 1,\ldots,N \quad k = 1,\ldots,M \\ &P_{ik}\left(\sum_{l=1}^{M}\sum_{j=1}^{N} T_{ijkl}\right) - \sum_{l=1}^{M}\sum_{j=1}^{N} P_{jl}T_{ijkl} = \Delta\mathbf{V}_{ik} && i = 1,\ldots,N \quad k = 1,\ldots,M \end{aligned} \tag{5.36}$$

The matrix A consists of M^2 sub-matrixes denoted $\tilde{A}$ each consisting of N^2 elements, while the vectors $\mathbf{p}$ and $\Delta\mathbf{V}$ consist of M subvectors denoted $\tilde{\mathbf{p}}$ and $\Delta\tilde{\mathbf{V}}$, respectively. The situation is illustrated in (5.37). The sub-matrix decides which two layers that the elements connect while the positions inside the sub-matrixes shows which two pressure compartments that communicate. A is a sparse matrix since most of the elements equal zero. The sub-matrixes are not symmetrical since $T_{ijkl} \neq T_{jikl}$ but the matrix A is symmetrical since $T_{ijkl} = T_{jilk}$.

$$\begin{bmatrix} \tilde{A}_{11} & \tilde{A}_{12} & \cdots & \tilde{A}_{1M} \\ \tilde{A}_{21} & \tilde{A}_{22} & \cdots & \tilde{A}_{2M} \\ \vdots & \vdots & \ddots & \vdots \\ \tilde{A}_{M1} & \tilde{A}_{M2} & \cdots & \tilde{A}_{MM} \end{bmatrix} \begin{bmatrix} \tilde{\mathbf{p}}_1 \\ \tilde{\mathbf{p}}_2 \\ \vdots \\ \tilde{\mathbf{p}}_M \end{bmatrix} = \begin{bmatrix} \Delta\tilde{\mathbf{V}}_1 \\ \Delta\tilde{\mathbf{V}}_2 \\ \vdots \\ \Delta\tilde{\mathbf{V}}_M \end{bmatrix} \tag{5.37}$$

6. Pressure simulation case studies

The methodology presented in the previous chapter is deduced by implementing and testing the models on different case studies. Models, ideas and concepts are continuously refined or rejected based upon the effects on real basins. Input data, a short description of the basins, results and conclusions from the North Sea and the Haltenbanken region are presented in this chapter. The secondary migration and basin modelling tool SEMI (see Appendix A) is used for handling input data, transmissibility calculations, depth maps, fault grids and plotting. The pressure simulations are performed using the simulator PRESSIM (Appendix B), which is developed parallel to the work of this Dr. Ing. study.

6.1 Pressure simulation in the North Viking Graben

The development and distribution of the overpressure in the Jurassic Brent Group and Statfjord Formation in the North Viking Graben area are modelled in this section. Both the shale compaction and quartz cementation (see section 5.2) models are used as pressure generating mechanisms. The study area is more or less identical to the study area in chapter 2. Some minor pressure compartments and parts of the hydrostatic flank are removed from the model reducing the number of pressure cells from 225 to 186. The same present day depth map for the Brent Group and mapped faults presented in Figure 3, chapter 2 are applied in this study. A hydrostatic pressure gradient of $1.03 \cdot 10^4 \, kg \cdot m^{-2} \cdot s^{-2}$ was used calibrating the simulations while the observed overpressures in chapter 2 were based upon a hydrostatic gradient equal to $9.83 \cdot 10^3 \, kg \cdot m^{-2} \cdot s^{-2}$. Thus the estimated observed overpressures are in general slightly lower in this chapter than in the paper presented in chapter 2. Appendix C gives a brief description of uncertainties regarding the estimation of measured overpressures. The Gullfaks area located in block 34/10, which is a regional drain for the formation water (Per Arne Bjørkum, pers. comm.), is not covered by the maps describing the study area. Thus the modelled overpressure becomes too high in the northwestern corner of the study area. The overpressure history in the cell containing the 34/08-01 well (the Visund field) is defined in order to account for this boundary effect. Apart from this correction, all the generation and dissipation of overpressure are handled by the models described in chapter 5.

Figure 6.1 shows the present day depth to the Brent Group including the outlined pressure compartments and calibration wells. Figure 2, chapter 2 shows the location of the study area. No exploration wells or pressure measurements are located in the deep graben stretching from block 34/12 to block 35/2. There are, however, several wells at the flanks of this graben and it is very important to match these moderately overpressured pressure compartments. The Brent and Statfjord isopach maps are plotted in Figure 6.2 and Figure

6.3, respectively. The thickness of the Brent Group varies between 100-200 m in the study area, roughly speaking. In the southwestern and northeastern parts of the study area there are some spots with a considerable higher thickness. The Statfjord Formation isopach shows a relatively thick formation in the 34/5, 34/6 and 35/4 blocks, while the thickness in the rest of the area lies between 100 and 200 m. The shaly Dunlin Group is, with some exceptions, about 200 m – 300 m thick in the study area. Due to large variations in the net/gross ratio in both the Brent Group and Statfjord Formation a mean net/gross ratio is calculated for all the pressure cells based upon the plots presented in Figure 6.4 and Figure 6.5. In the Brent Group there are very high net-gross values in the southwestern parts of the study area. The values smoothly decrease in the northern and western directions. The Statfjord net-gross values are distributed slightly differently. The western parts of the study area have relatively high net-gross values while there is a decreasing trend in the eastern direction. The modelled reductions in the porosities caused by quartz cementation are influenced by the differences in the net-gross ratios plotted in Figure 6.4 and Figure 6.5, which are extrapolated from measurements in the exploration wells. In addition, the quartz cementation model is very sensitive to the temperature. Present day and estimated paleo waterdepth maps are therefore used in the study.

Table 6.1 lists the values of the parameters describing the generation and accumulation of overpressure used for modelling the best match presented in Table 6.3. The accumulating zone is modelled between 2500 m and 4000 m, which corresponds well to the observations in Figure 5.5. The very low value of the accumulating factor A is due to the need for accumulating the intermediate overpressure in the relatively shallow 35/8 and 35/11 area. There is nothing remarkable with the rest of the values listed in Table 6.1 except from the excessively short time step. Although the length of the time step is only 1000 years the numerical solver halves the time step 4 times in order to handle the ongoing pressure dissipation. The need for these short time steps is caused by the large differences in lateral transmissibilities and the intense pressure generation at certain depths. The study area contains both shallow and deeply buried pressure compartments. This leads to differences in the lateral connectivity of up to 10 orders of magnitude. Thus it becomes computational intensive to solve the flow matrix describing the dynamics of the modelled basin. Applying the parameters listed in Table 6.2 to the lateral transmissibility model described in chapter 2 resulted in the modelled present day overpressure listed in Table 6.3 and plotted in Figure 6.6 and Figure 6.7. In similarity with the modelled results in chapter 2, all the observed main trends in the North Viking Graben were covered by the results. Figure 6.6 and Figure 6.7 clearly show the high overpressures in the graben area between the shallow eastern flank and the Gullfaks/Visund area around block 34/8. In the southern parts the pressure increase from the hydrostatic eastern flank to the highly overpressured deep parts in the west. Table 6.3 shows the deviations between the modelled and observed overpressures. In average, the deviations are about 20 bar, which is close to the uncertainty

estimating the observed overpressures (Appendix C). Boundary effects cause the three largest deviations in Table 6.3. The overpressures in well 30/3-2 are modelled about 100 bar higher than the observed pressures both in the Brent Group and in the Statfjord Formation. This is due to the same boundary effect described in chapter 2, where the area south of the boundary acts as a drainage path for the 30/3-2 compartment. The shallow hydrostatic parts east of the 35/3-4 well has been excluded from the study area due to the decompaction applied to provide the paleo depth input data for this study. The most efficient drain for the 35/3-4 pressure compartment is thus not included and the modelled overpressure is about 90 bar higher than the observed. The standard and mean deviations in Table 6.3 can be reduced to 17.2 bar and 9.9 bar, respectively; if the calibration points affected by the boundary is excluded from the calibration. The overpressure in the compartment containing the 34/8-2 and 34/8-3 wells is modelled about 50 bar in excess of the observed values. It is difficult to drain this area by increasing the lateral connectivity without draining the 35/8 and 35/11 areas simultaneously and thus displacing the transition zone in the western direction. If the whole of the 34/7 and 34/10 blocks were included into the study area this would hopefully make up for this problem. The modelled overpressure in the 35/8-1 Brent compartment matches the observed pressure. However, the corresponding Statfjord compartment is modelled about 50 bar below the calibration pressure. This deviation is probably caused by an artificially high connectivity between the Statfjord Formation and the Brent Group in this area. It is not likely that the implemented generation mechanisms or vertical dissipation models cause the modelled overpressure to drop downwards at these depths.

Figure 6.8 and Figure 6.9 show the modelled average properties of the basin plotted versus time. The plot shows that there has been a relatively rapid subsidence the latest 2 million years while there has been a low or moderate subsidence rate the rest of the time. The modelled mean overpressure in the basin gradually increases from 0 bar to about 50 bar during the Eocene and Oligocene. The plot indicates relatively small changes in the overpressure in the late Tertiary while a rapid subsidence probably contributes to double the mean overpressure during the Quaternary. Figure 6.14 shows how this trend turns out for pressure distribution in the basin for some points of time. The results suggest that a considerable part of the observed overpressure in the North Viking Graben is generated during the Quaternary. In Figure 6.12 the modelled overpressures and leak-off pressures for all the Brent compartments are compared to the depths. This plot shows the same trend as the corresponding plot in Figure 5.5, which is based upon observed data. It seems that the differences between the modelled leak-off pressures and formation pressures reach a minimum between 3 km and 4 km depth. The ratio between generation and dissipation is maximised at these depths increasing the probability for hydraulic leakage. Below these depths the differences between formation pressures and leak-off pressures increase. Only

the boundary compartment west of well 34/10-23 has been modelled to leak formation water vertically. The cumulative leakage volume is plotted in Figure 6.8.

The mean porosity of the basin is modelled to slowly decrease during the Tertiary. The rapid Quaternary subsidence seems to speed up porosity reducing mechanisms. Figure 6.10 shows the modelled mean porosities of the Brent compartments at present day. Figure 6.13 shows the porosity trend for the Brent Group. The porosities seem to follow a relatively unambiguous trend at depths above 4000 m. The scattering in these data below 4000 m or porosities below 0.10 is caused by differences in temperature history and net-gross ratios. All the modelled porosities are supposed to reflect the water budget regarding large-scale fluid flow rather than the real porosities in the basin.

The quartz cementation model has been the dominating mechanism generating overpressure during most of the Tertiary (Figure 6.9). The rapid subsidence the latest 10 million years has increased the importance of the mechanical compaction. However, the modelled shale compaction decreases during continual rapid subsidence because the overpressure itself put a brake on the mechanical pressure generation. At present day the results presented in Figure 6.8 indicate that there is a 50-50 % distribution between the chemical and mechanical compaction. Figure 6.11 shows the modelled part of the overpressure generated by quartz cementation (PQC) for the Brent compartments at present day. Obviously, the chemical compaction generating overpressure is the most important mechanism at the intermediate overpressured flanks of the graben area. The high PQC-values in Figure 6.11 correspond well to the favourable depths in Figure 6.1 for the quartz cementation process. Figure 6.15 shows how the importance of the quartz cementation may vary through time. The results suggest that the quartz cementation more or less controlled the pressure generation 25 million years ago (upper left plot, Figure 6.15) when the subsidence was at a minimum (Figure 6.9). The same figure (lower left) shows that during the rapid subsidence two million years ago the modelled mechanical compaction seem to dominate the porosity reduction and the subsequent increase in pressure in the basin.

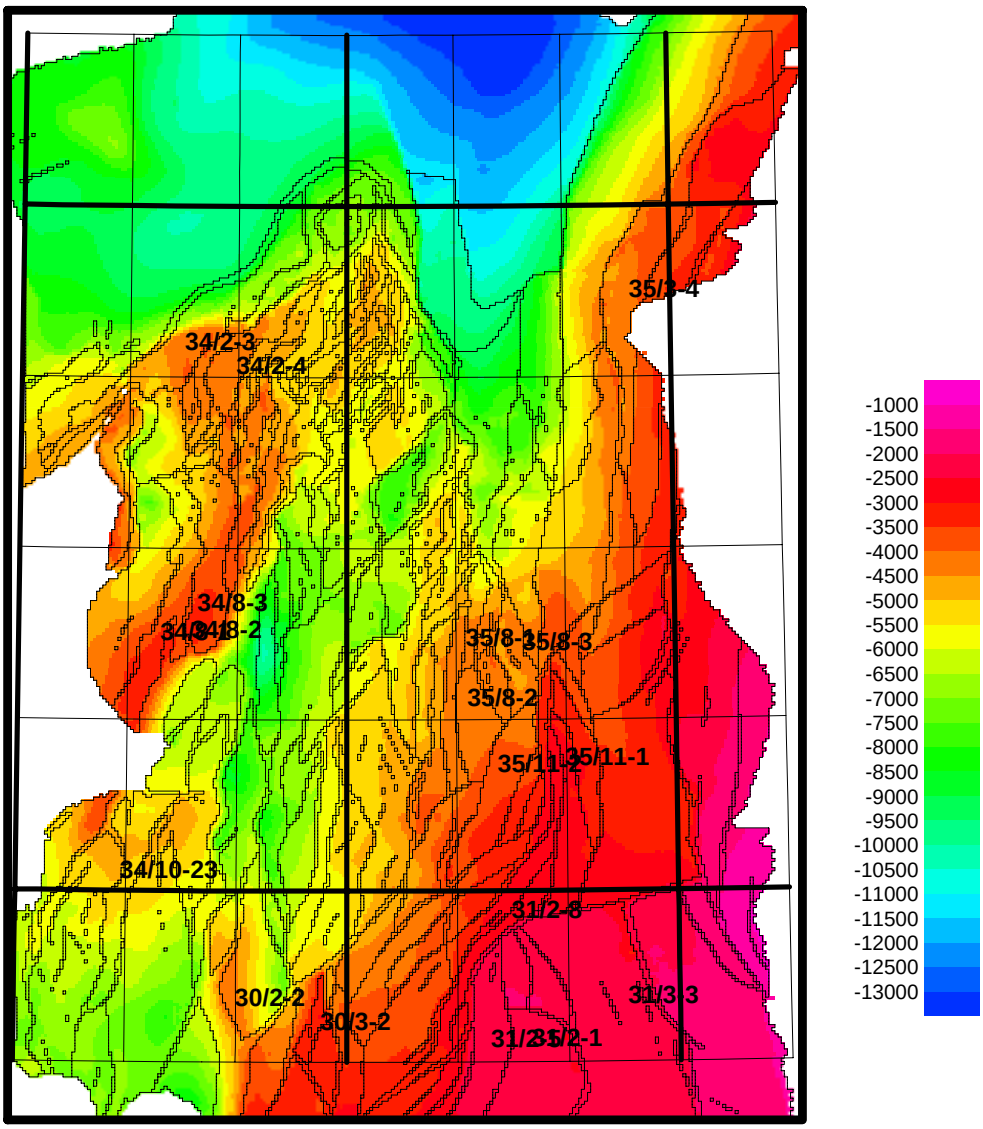

Figure 6.1: *Present day depth* (m) *to Brent in the North Viking Graben including outlined pressure compartments and the calibration wells*

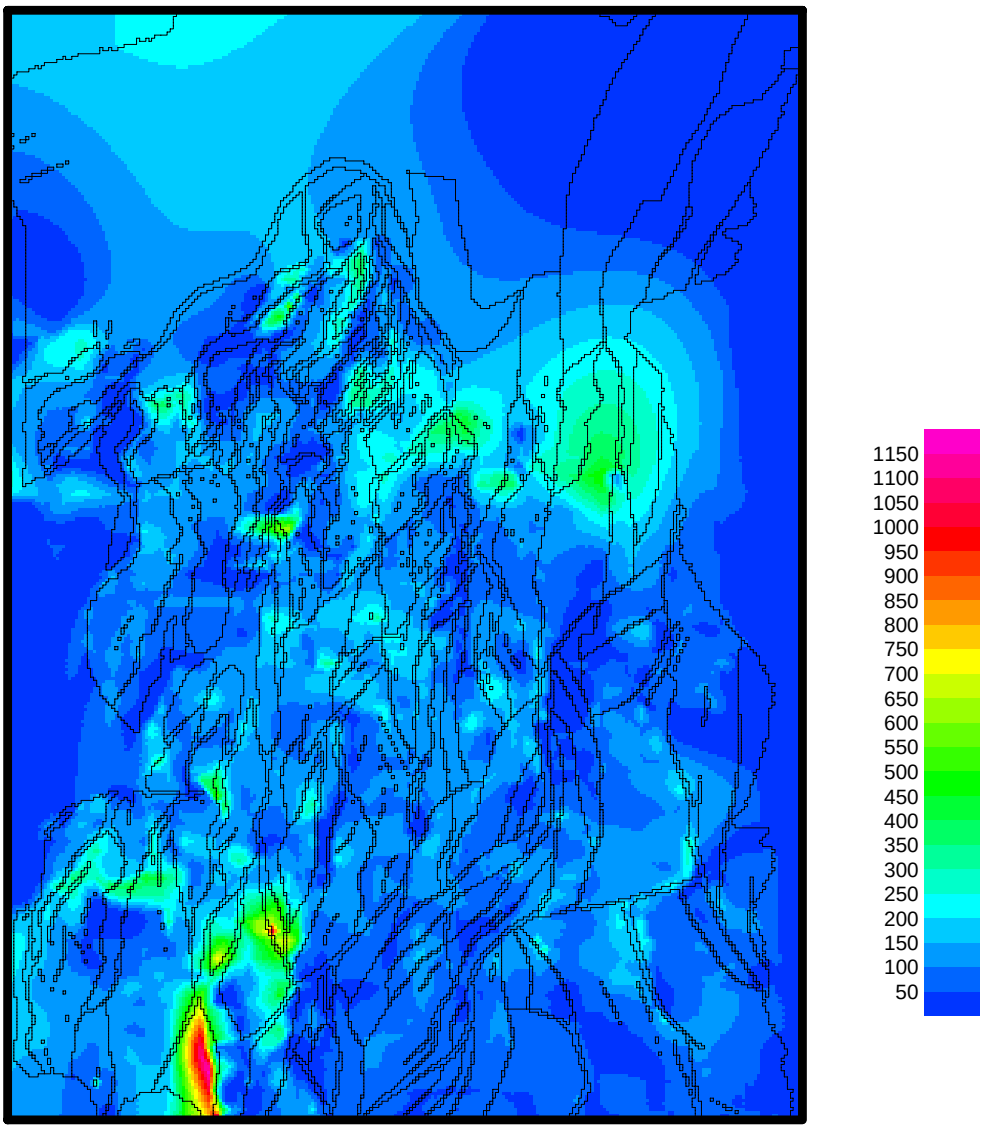

Figure 6.2: Present day thickness (m) *of the Brent Group*

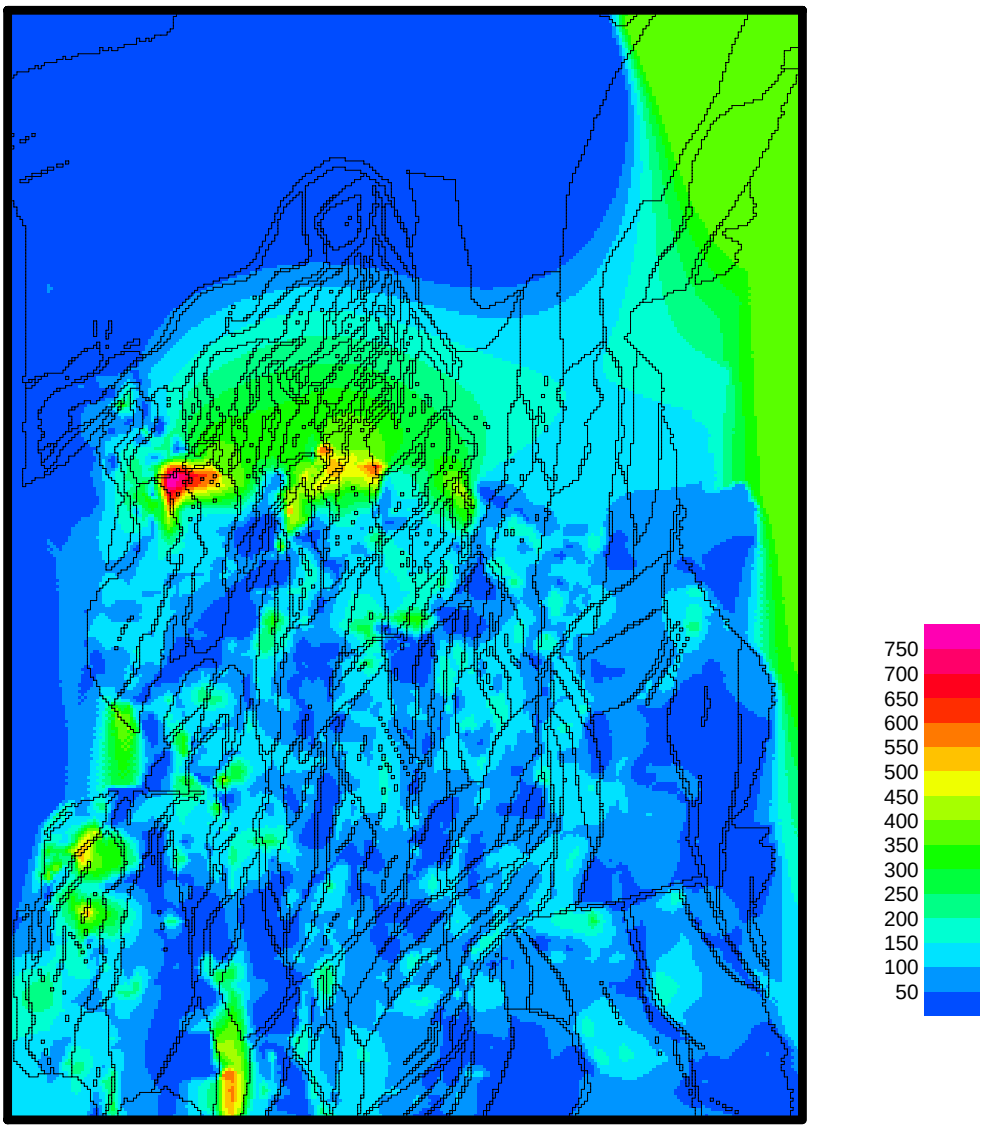

Figure 6.3: Present day thickness (m) *of the Statfjord Formation*

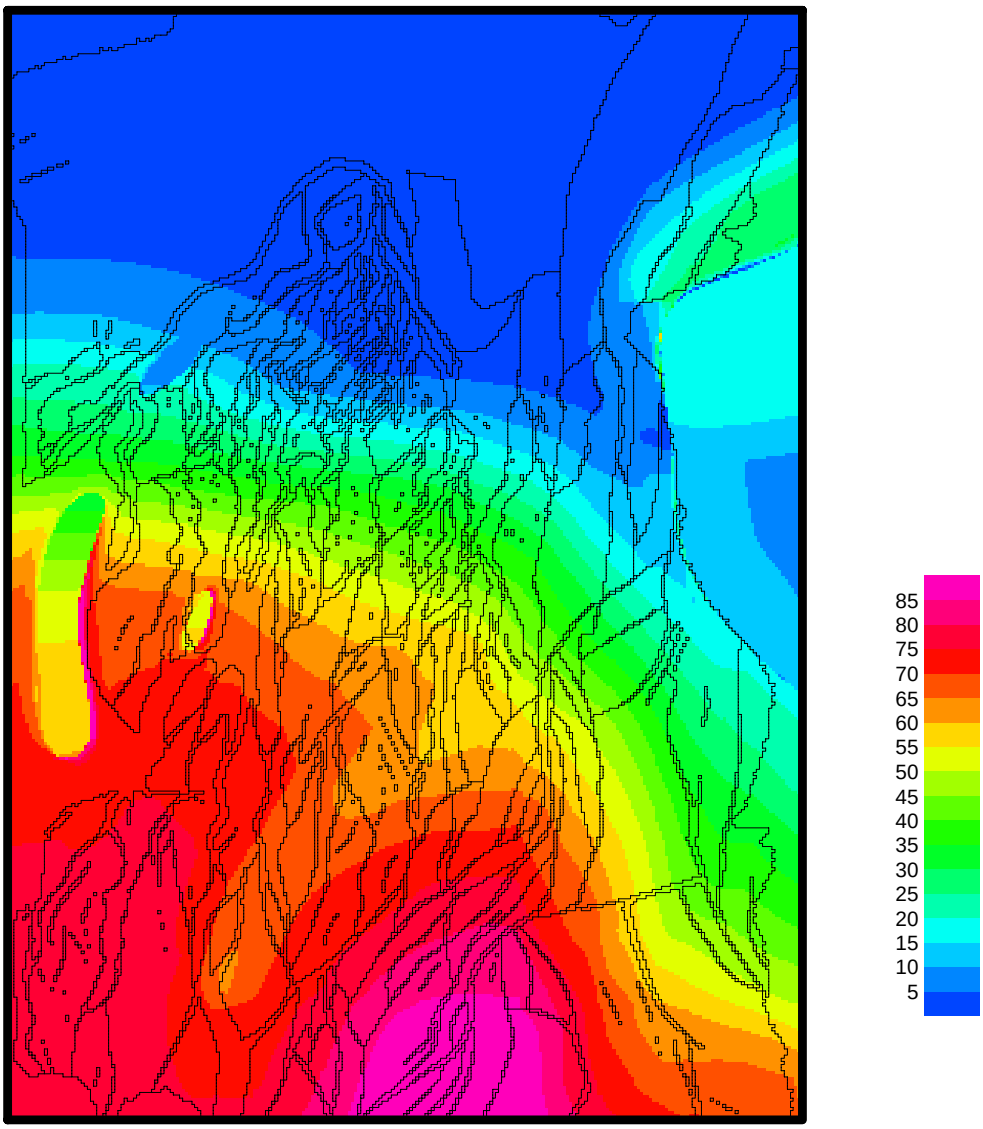

Figure 6.4: Net/gross ratio in the Brent Group

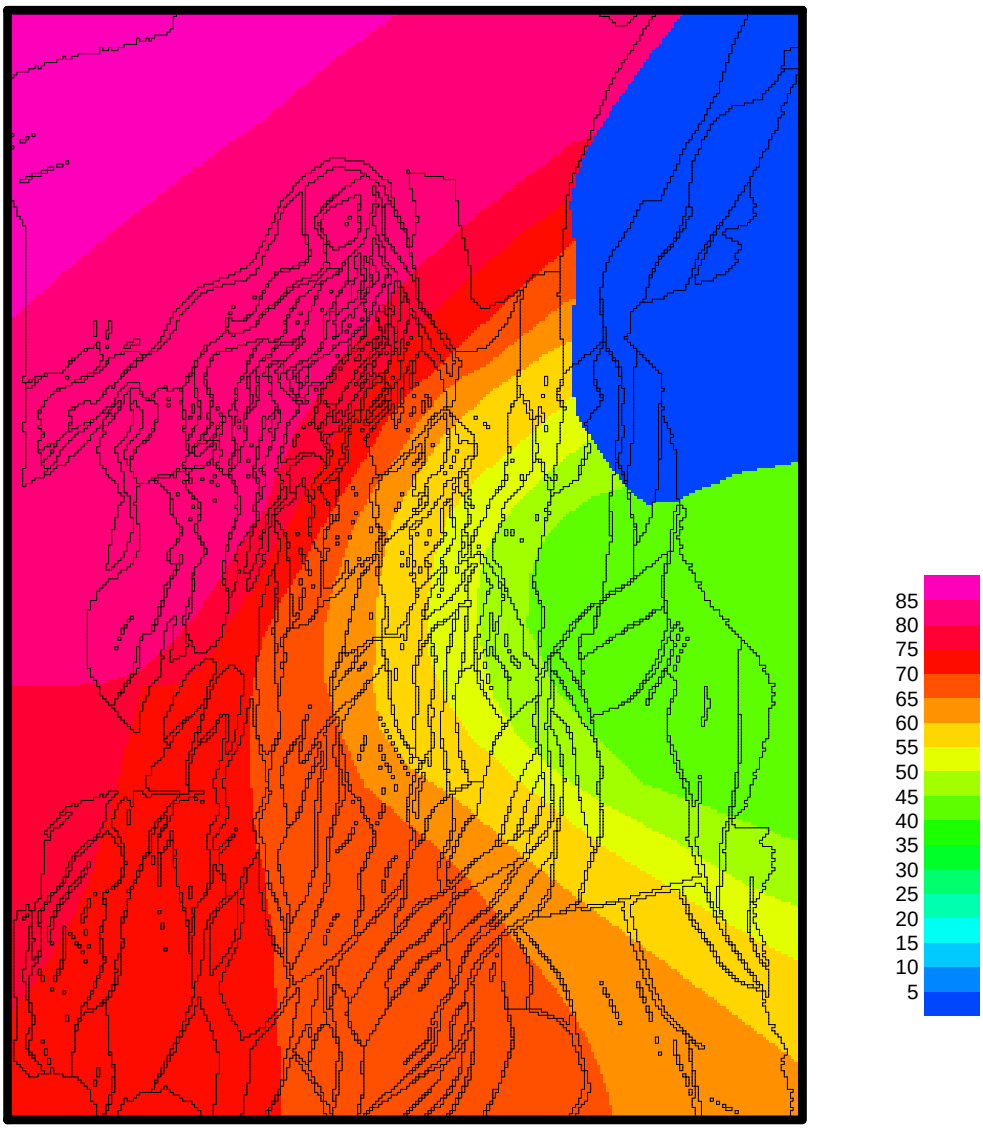

Figure 6.5: Net/gross ratio in the Statfjord Formation

Table 6.1: Parameters used for modelling generation and vertical dissipation of overpressure in the North Viking Graben. (See section 5.1 and 5.2 for an explanation of the variables)

Accumulating depth (m)	z_a	2550
Sealing depth (m)	z_s	4000
Shale sealing thickness (m)	γ	100
Salinity (ppm)	s	50000
Accumulating exponent	A	0.20
Time step (years)	Δt	1000
Diameter of quartz grain size (m)	D	0.0003
Fraction of detrital quartz	f	0.65
Temperature at which quartz cementation starts ($^\circ$C)	T_{C0}	80.0
Temperature at which quartz cementation is completed ($^\circ$C)	T_{C1}	175.0
First order leakage coefficient ($\text{bar} \cdot \text{m}^{-1}$)	σ_1	0.163
Second order leakage coefficient ($\text{bar} \cdot \text{m}^{-2}$)	σ_2	$1.02 \cdot 10^{-5}$
Porosity at seabed	ϕ_{S0}	0.50
Porosity-depth constant 1 (m)	η_1	2400
Porosity-depth constant 2	η_2	0.50
Temperature at seabed ($^\circ$C)	T_0	4.0
Temperature gradient ($^\circ\text{C} \cdot \text{m}^{-1}$)	$\frac{\partial T}{\partial z}$	0.035
Porosity not accessible for quartz cementation (Brent Group)	ϕ_{C1}	0.02
Clay coating factor (Brent Group)	C	0.5
Porosity not accessible for quartz cem. (Statfjord Formation)	ϕ_{C1}	0.02
Clay coating factor (Statfjord Formation)	C	0.5

Table 6.2: Parameters used for calculating lateral fluid flow in the North Viking Graben. (See chapter 2 for an explanation of the variables)

Percent remaining fault-transmissibility at no overlap	p	0.10
Width of fault blocks (m)	b	20.0
Porosity at seabed	ϕ_0	0.50
Rate of change in porosity versus depth (m^{-1})	c	0.00028
Porosity where the $K - \phi$ curve changes between deep and shallow relationships	ϕ_b	0.08
Permeability where the $K - \phi$ curve changes between deep and shallow relationships (mD)	K_b	0.000009

Rate of change in fault zone permeability (log) versus depth (log) for shallow faults	δ_{sh}	0.1
Rate of change in fault zone permeability (log) versus depth (log) for deep faults	δ_{de}	7.0

Table 6.3: Pressure deviation table for the North Viking Graben case study. (Br) indicates a calibration to the Brent Group, while (St) indicates a calibration to the Statfjord Formation. See Figure 6.1 for the locations of the wells.

Well	Measured overpressure (bar)	Modelled overpressure (bar)	Deviation (bar)
30/02-02 (Br)	273.1 - 281.2	284.7	3.5
30/03-02 (Br)	26.6 - 36.3	134.0	97.7
31/02-01 (Br)	1.1 - 2.6	0.0	-1.1
31/02-05 (Br)	0.0 - 2.9	0.0	0.0
31/02-08 (Br)	3.5 - 4.1	0.0	-3.5
31/03-03 (Br)	1.7 - 2.2	0.0	-1.7
34/02-04 (Br)	181.6 - 228.0	203.8	0.0
34/08-02,03 (Br)	131.4 - 137.9	180.5	42.6
34/10-23 (Br)	364.1 - 368.0	347.1	-17.0
35/03-04 (Br)	28.0 - 44.3	136.8	92.5
35/08-01 (Br)	180.6 - 188.7	182.9	0.0
35/08-02 (Br)	150.5 - 164.2	165.2	1.0
35/08-03 (Br)	163.7 - 172.4	162.4	-1.3
35/11-01 (Br)	0.0	0.0	0.0
35/11-02 (Br)	126.6 - 141.1	148.1	7.0
30/03-02 (St)	22.9 - 24.2	133.5	109.3
31/02-08 (St)	0	0.0	0.0
31/03-03 (St)	0	0.0	0.0
34/02-03 (St)	238.1 - 238.4	213.1	-25.0
34/02-04 (St)	212.3 - 212.4	201.5	-10.8
34/08-01 (St)	142.3 - 143.6	143.0	0.0
34/08-02,03 (St)	149.6 - 150.6	169.6	19.0
34/10-23 (St)	376.3 - 405.5	351.3	-25.0
35/08-01 (St)	226.5 - 245.8	178.0	-48.5

Standard deviation = 37.4

Mean deviation = 19.5

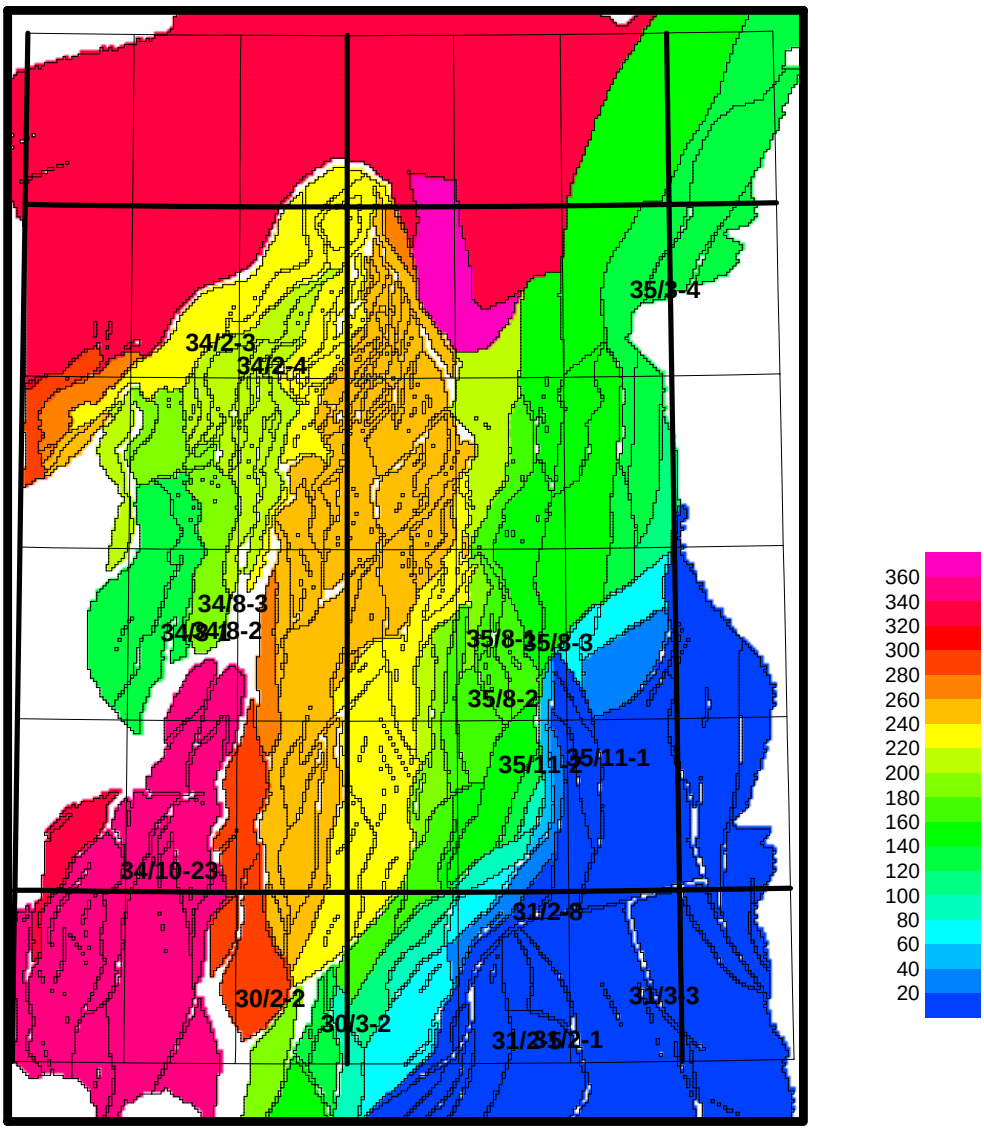

Figure 6.6: *The modelled present day overpressure* (bar) *in the Brent Group of the North Viking Graben.*

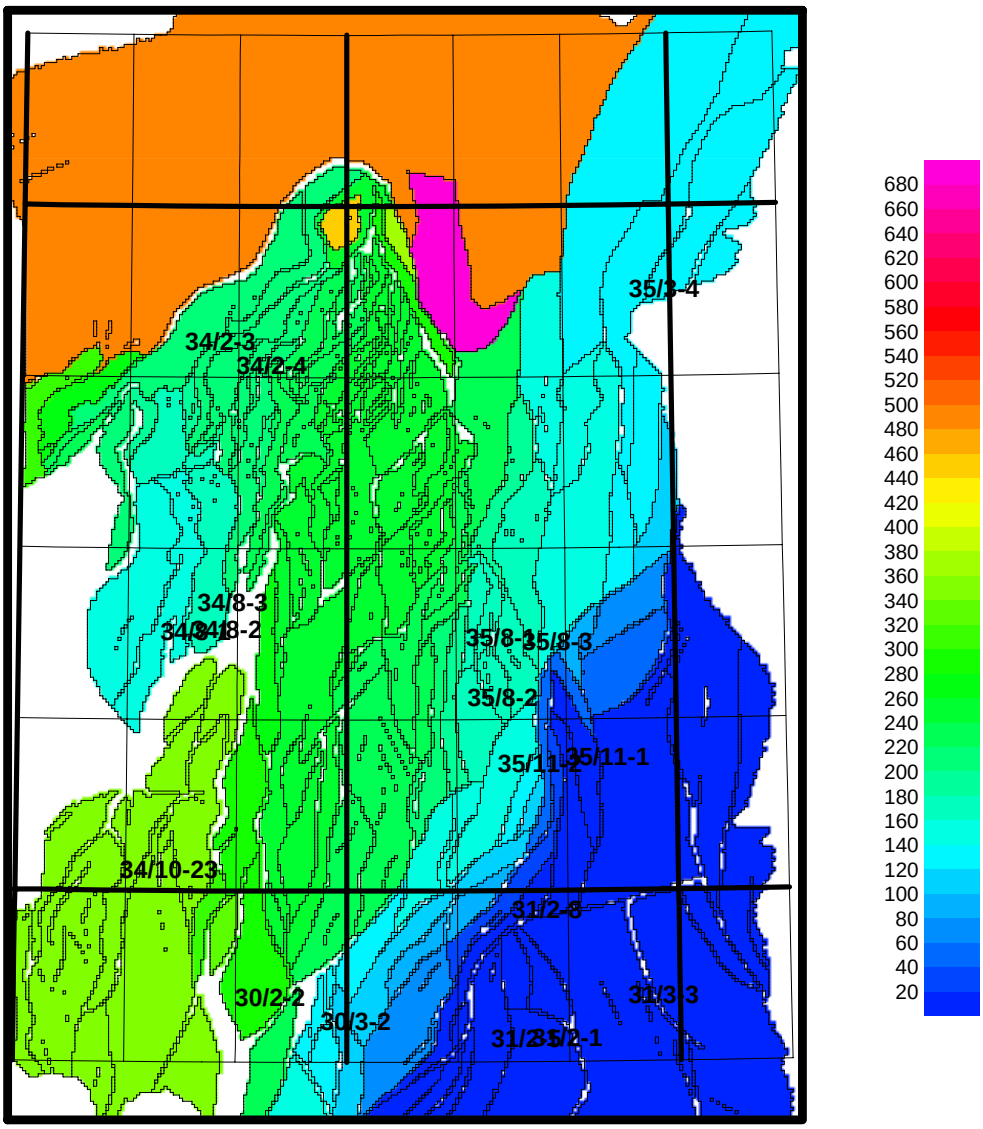

Figure 6.7: *The modelled present day overpressure* (bar) *in the Statfjord Formation of the North Viking Graben.*

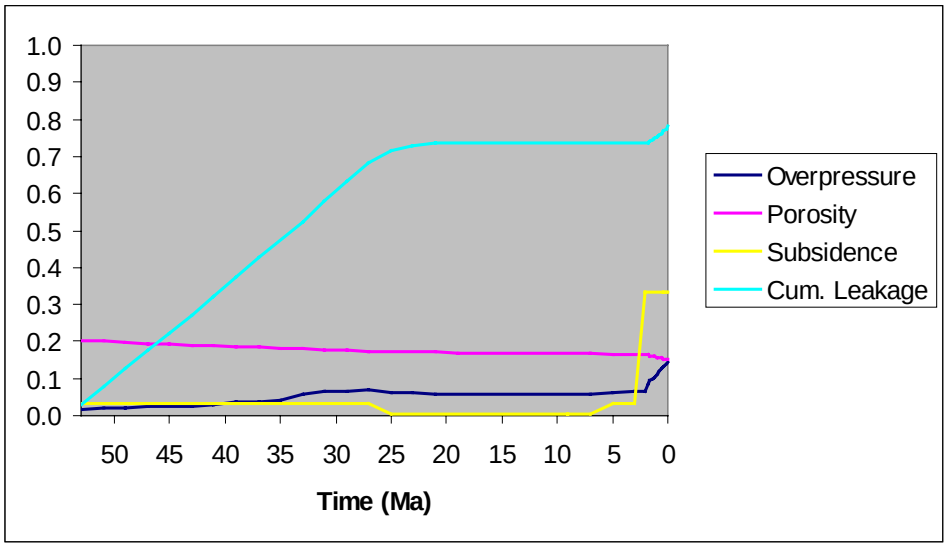

Figure 6.8: *The modelled mean overpressure* (10^4 bar), *porosity, subsidence* (10^{-3} m/years) *and cumulative hydraulic leakage* ($10^{10}m^3$) *vs. time* (Ma) *in the North Viking Graben.*

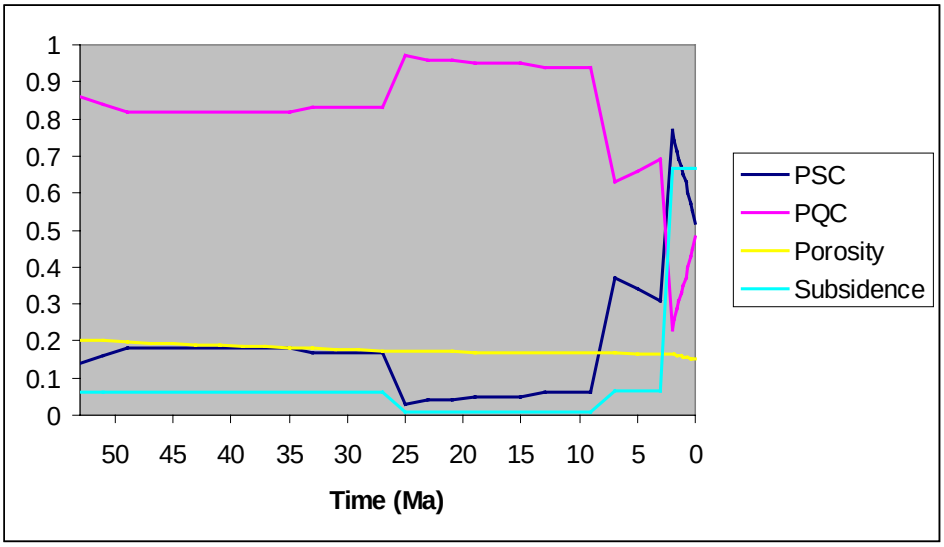

Figure 6.9: *The modelled mean porosity, subsidence* (10^{-3} m/years), *part of the overpressure generated by shale compaction* (PSC) *and part of the overpressure generated by quartz cementation* (PQC) *vs. time* (Ma) *in the North Viking Graben.*

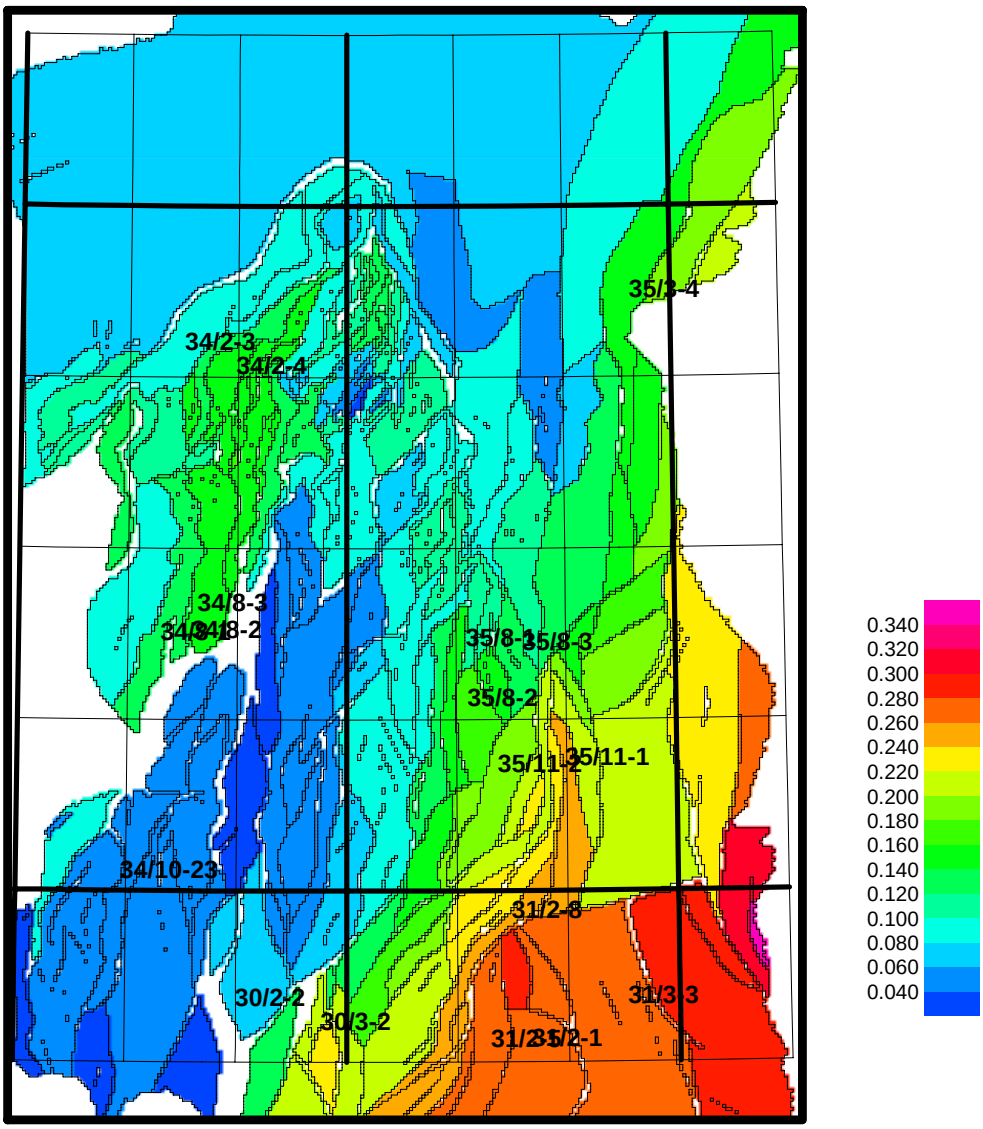

Figure 6.10: The modelled present day porosity in the Brent Group of the North Viking Graben.

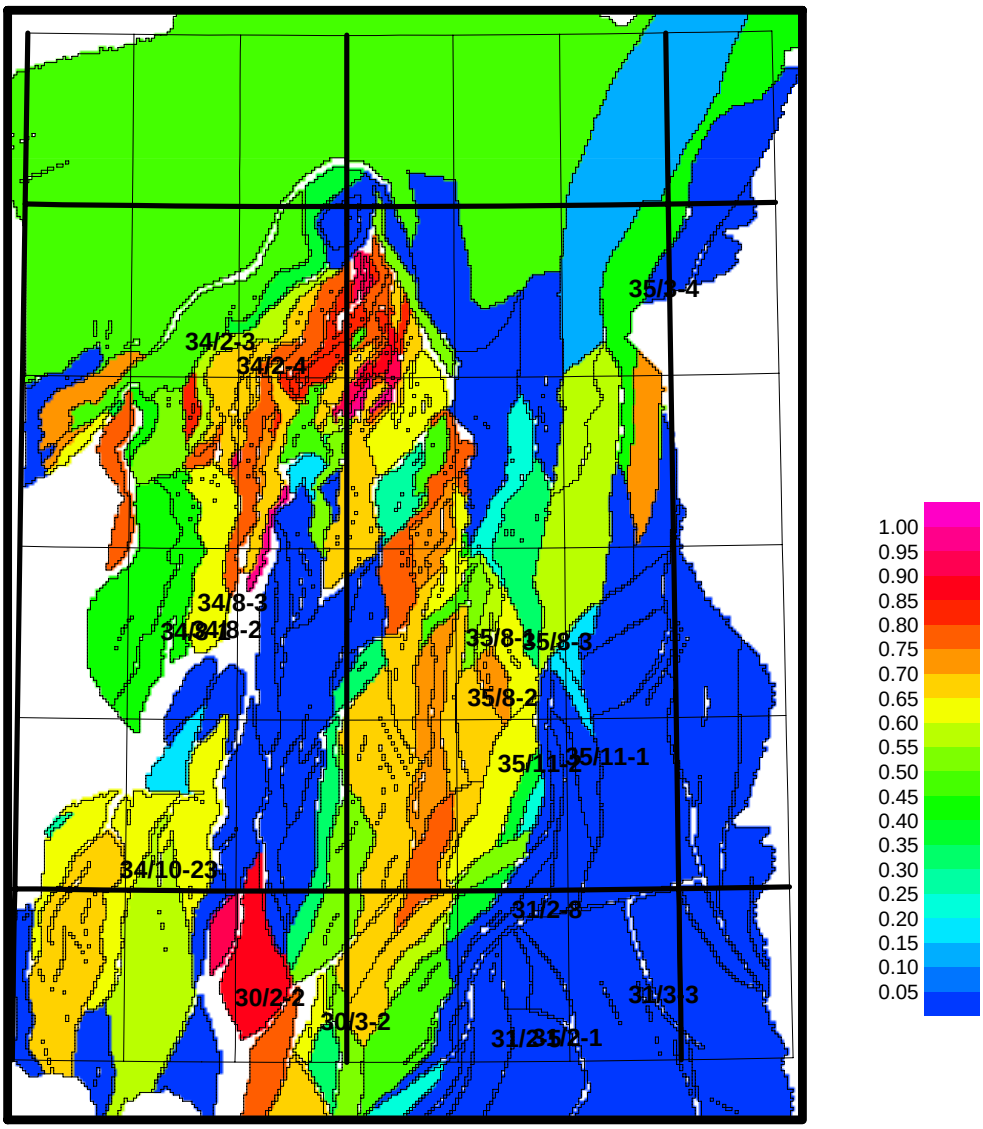

Figure 6.11: The modelled part of the overpressure generated by quartz cementation at present day in the Brent Group of the North Viking Graben.

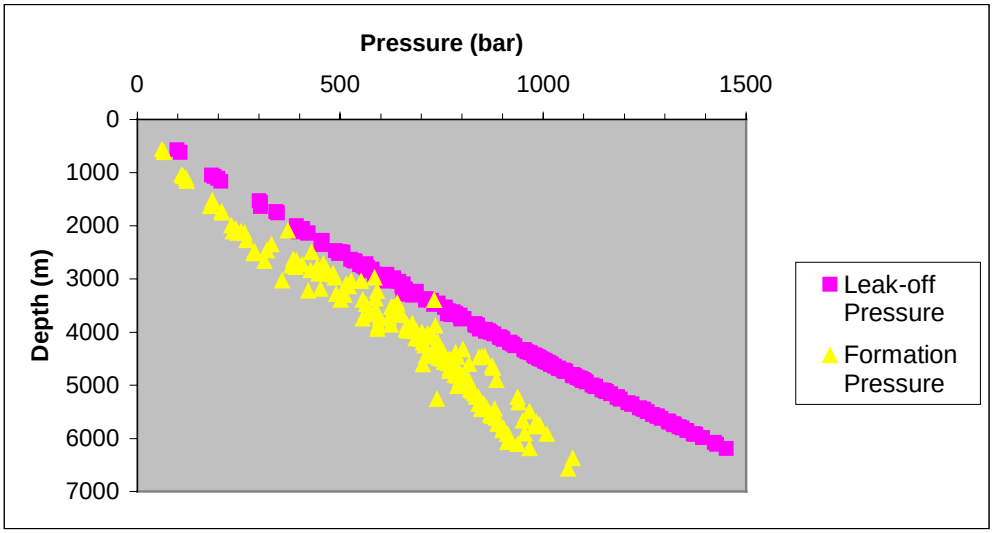

Figure 6.12: *Modelled present day formation pressures* (bar) *and leak-off pressures* (bar) *plotted versus the depth of the top points of the Brent Group pressure compartments in the North Viking Graben.*

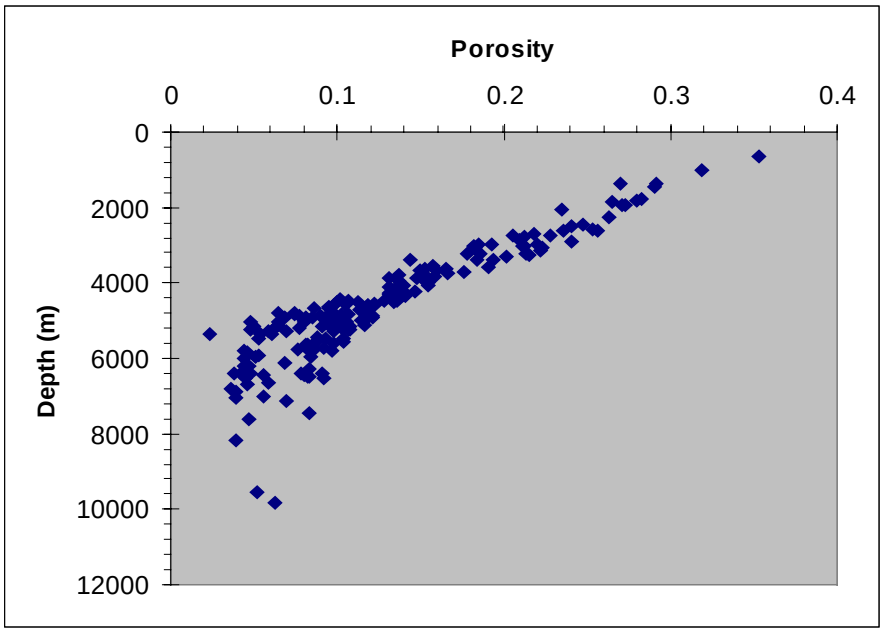

Figure 6.13: *Modelled present day mean porosities of the Brent Group compartments plotted versus the depth* (m) *in the North Viking Graben.*

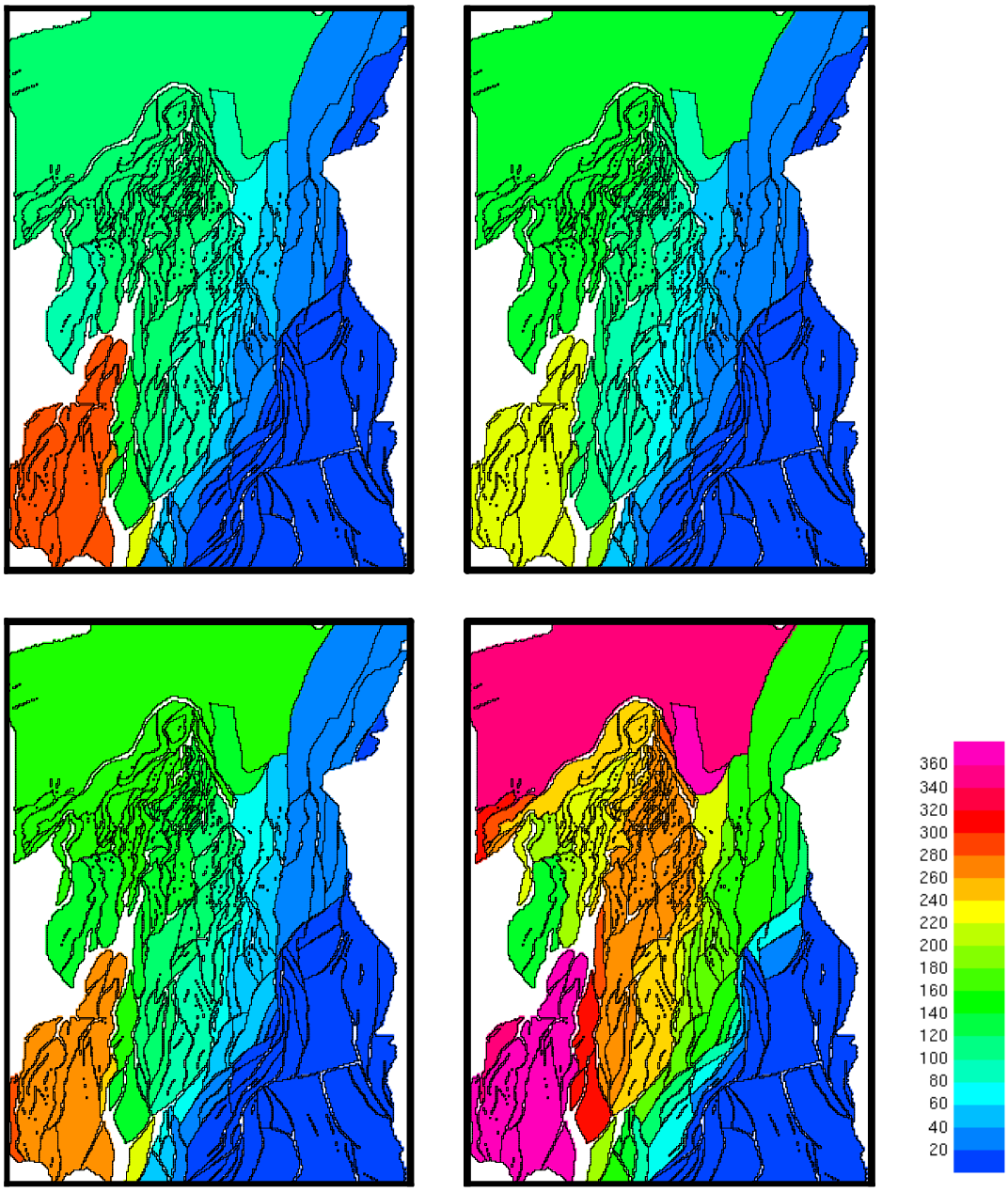

Figure 6.14: *The modelled overpressure* (bar) *in the Brent Group at* 25 Ma *(upper left),* 7 Ma *(upper right),* 2 Ma *(lower left) and present day (lower right) in the North Viking Graben.*

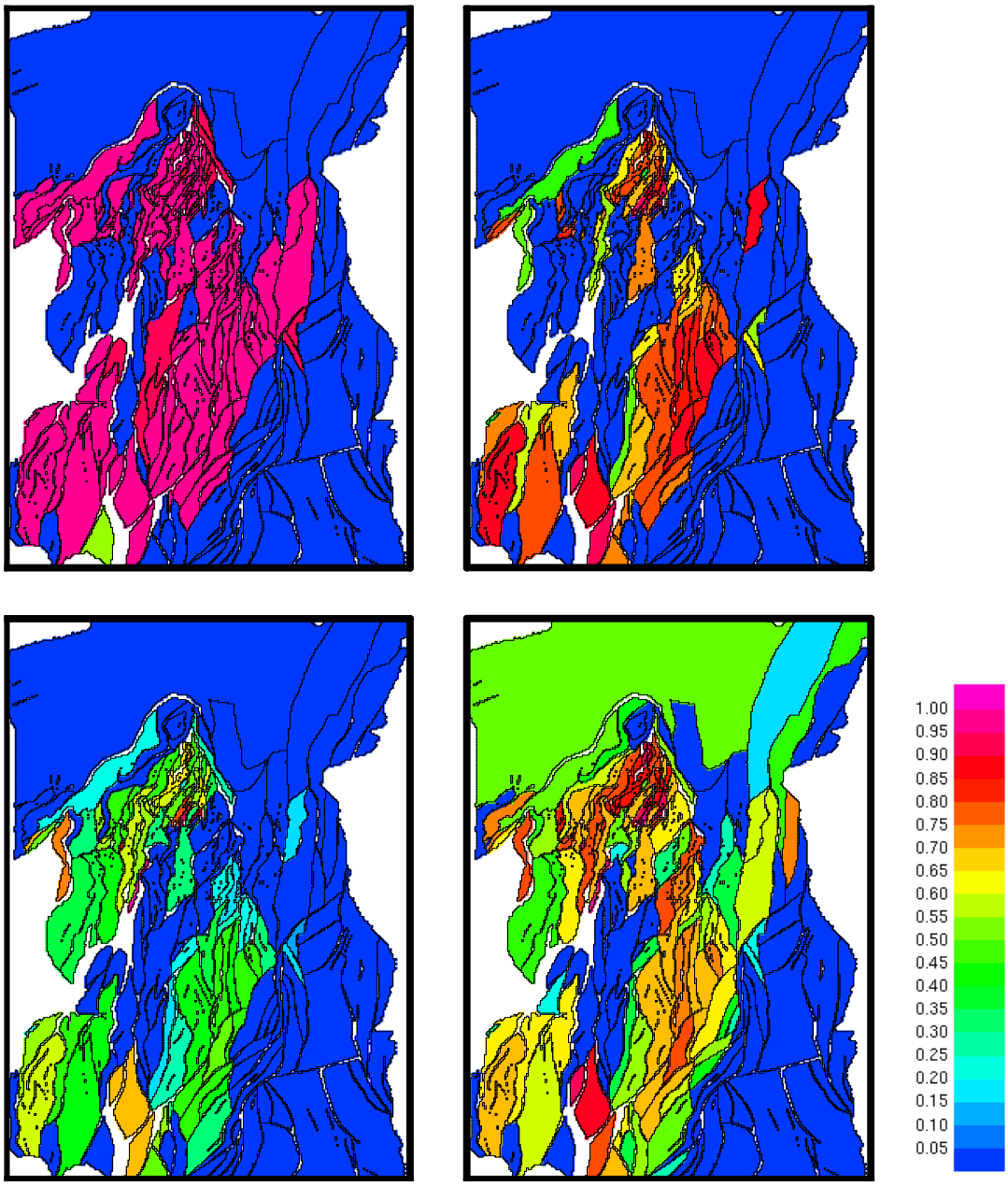

Figure 6.15: The modelled part of the overpressure in the Brent Group generated by quartz cementation at 25 Ma *(upper left),* 7 Ma *(upper right),* 2 Ma *(lower left) and present day (lower right) in the North Viking Graben.*

The modelled properties in the two compartments containing well 30/02-02 and 35/08-02 are plotted in Figure 6.16 and Figure 6.17, respectively (see Figure 6.1 for the location). The 30/02-02 Brent compartment is buried at a depth of 5200 m in average and contains a present day overpressure of about 280 bar. The modelled overpressure in well 30/02-02 increases during the 25 first million years of the simulated time. The chemical compaction is modelled to generate all the overpressure in this compartment from 25 to 10 Ma and the overpressure seems to drop during this time interval where there is no subsidence. This is due to the effect of the lateral drainage in the basin being greater than the pressure generation. The overpressure increases strongly during the Quaternary in similarity with the mean of the basin in Figure 6.8. The same pressure trend is illustrated in Figure 6.17 for the 35/08-02 compartment where the overpressure is lower due to less accumulation and a larger lateral drainage. Both the 30/02-02 and 35/08-02 compartments show the same tendency with regard to the pressure generating mechanisms. While the quartz cementation is the dominating mechanisms during the Tertiary, the importance is more equally distributed between the mechanical and chemical compaction during the rapid subsidence in the Quaternary. It is not likely that hydraulic fracturing will occur in none of the two compartments because the modelled overpressures are far below the respective leak-off pressures.

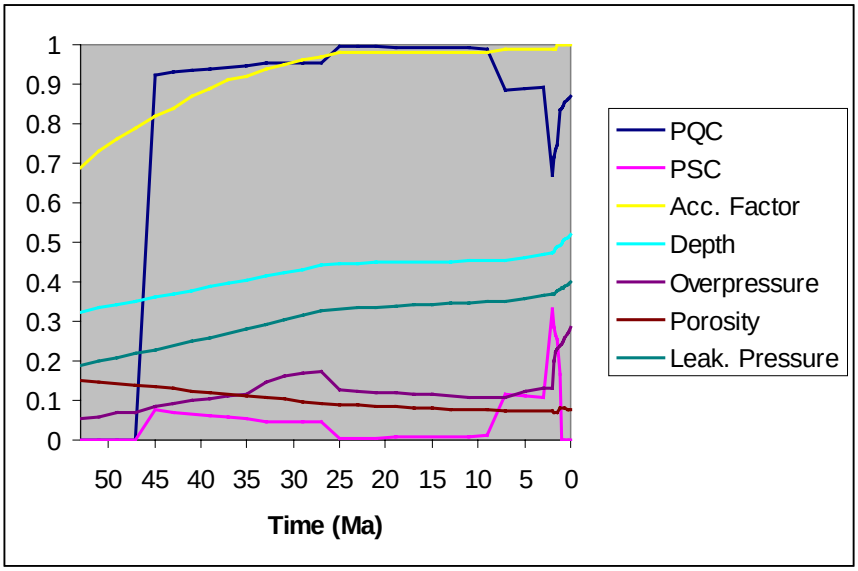

Figure 6.16: *Mean depth* (10^4m), *modelled overpressure* (10^3 bar), *porosity, part of the overpressure generated by quartz cementation* (PCQ), *part of the overpressure generated by shale compaction* (PSC), *accumulating factor and leak-off pressure* (10^3 bar) *plotted versus time* (Ma) *for the 30/02-02 compartment.*

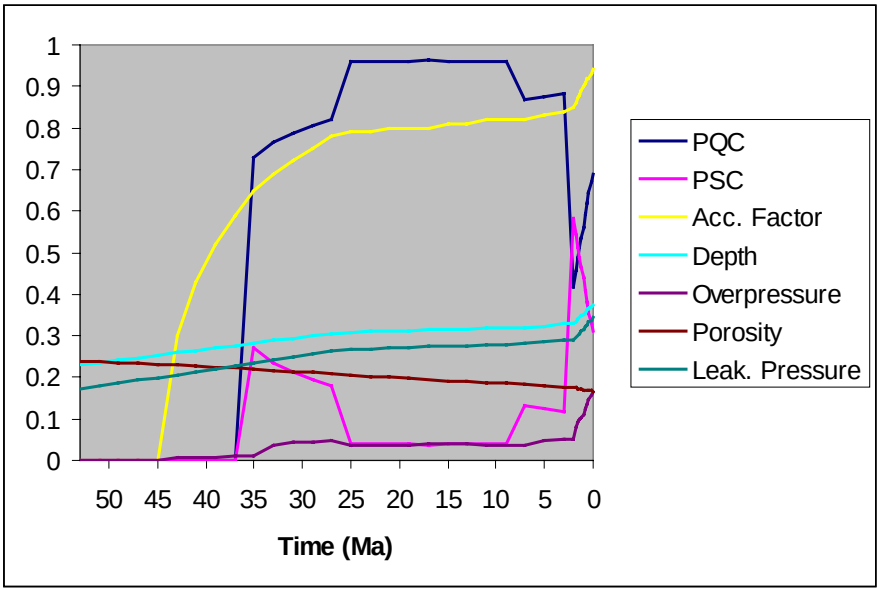

Figure 6.17: *Mean depth* (10^4m), *modelled overpressure* (10^3 bar), *porosity*, *part of the overpressure generated by quartz cementation* (PCQ), *part of the overpressure generated by shale compaction* (PSC), *accumulating factor and leak-off pressure* (10^3 bar) *plotted versus time* (Ma) *for the 35/08-02 compartment.*

Dissipation test of the modelled present day overpressure

The modelled present day overpressures in the North Viking Graben plotted in Figure 6.6 and Figure 6.7 are dissipated by running the pressure simulator with the pressure generating mechanisms turned off. The curve in Figure 6.18 shows how the modelled mean overpressure in the North Viking Graben developed the last 5 million years. If it has been possible to stop the pressure generation the model suggest that the overpressure will dissipate relatively fast. Roughly speaking the mean overpressure is halved in 1 million years according to the curve. If the previously mentioned regional drainage in the Gullfaks area was included in the study area the dissipation would have been faster. Figure 6.19 shows how the overpressures collapse after 1, 2 and 4 Myr of dissipation. The overpressures leak out relatively fast even the deeply buried compartments. Conclusively, the results indicate that the overpressure in the area is a dynamic phenomenon.

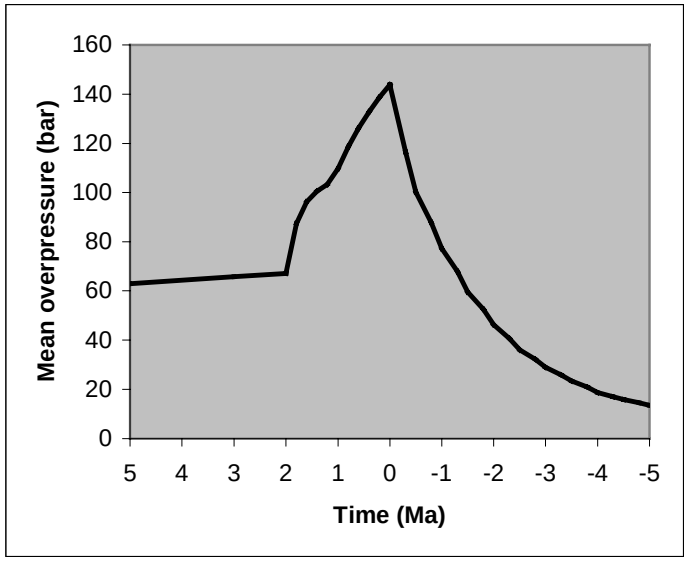

Figure 6.18: *Mean modelled overpressure* (bar) *in the North Viking Graben area during the latest* 5 million years *and* 4 million years *of dissipation.*

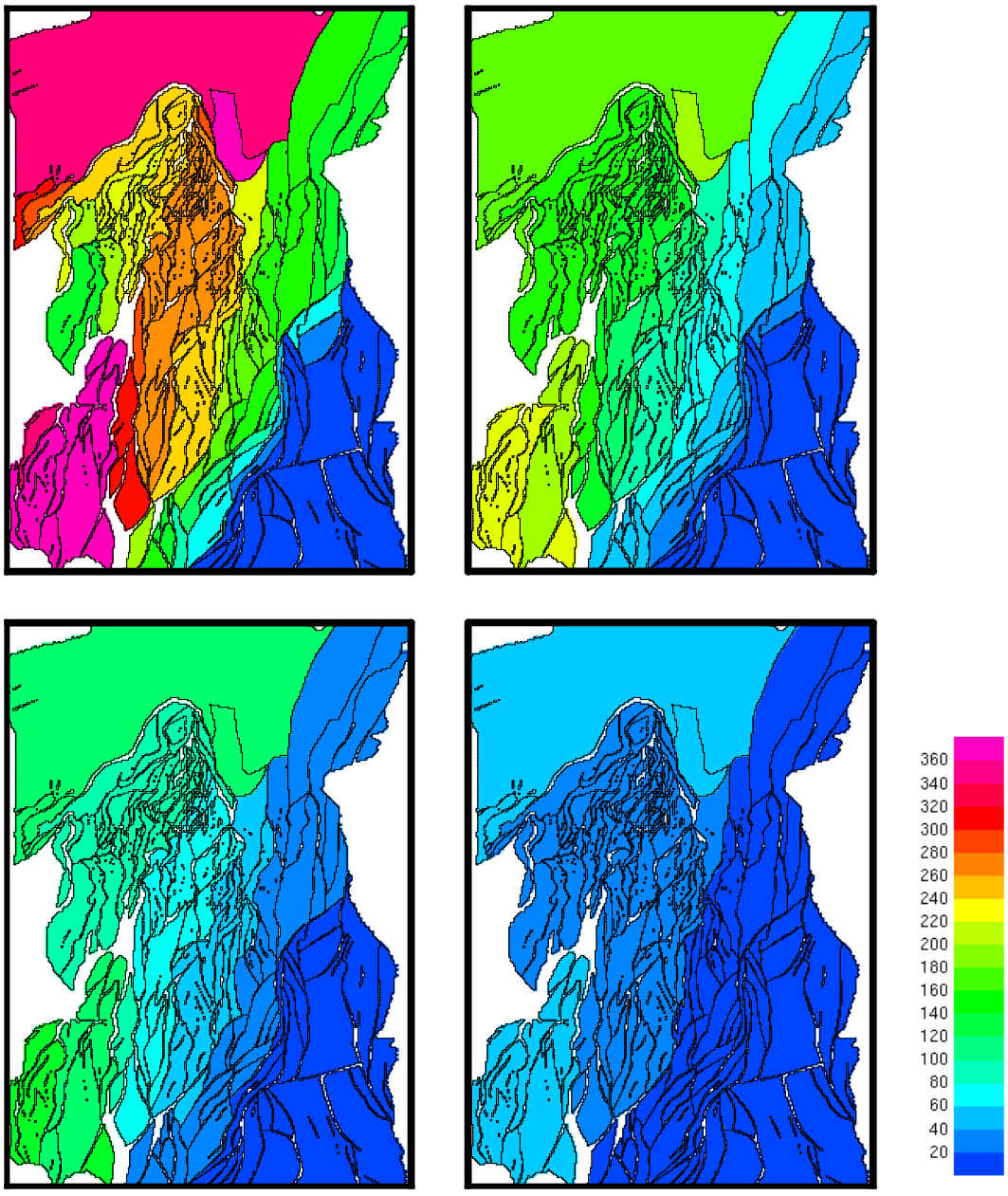

Figure 6.19: *Present day modelled overpressure* (bar) *in the Brent Group (upper left) and the distribution of overpressure after* 1 Myr *(upper right),* 2 Myr *(lower left) and* 4 Myr *(lower right) of dissipation in the North Viking Graben.*

Single layer simulation

The Statfjord Formation is removed from the model in order to study the interaction between the two layers represented. Figure 6.20 shows the modelled present day overpressure using the input from Table 6.1 and Table 6.2. Although a considerable part of the pressure generating lithologies are removed from the model together with the Statfjord Formation, the modelled overpressure in the Brent Group is considerable higher than the corresponding pressures (Figure 6.6 and Table 6.4) when the Statfjord Formation was present. Thus the cross flow between the two layers strongly influence the modelled results. Removing the deepest reservoir layer with the lowest fault permeability values did not increase the draining efficiency of the basin. This is an indication that parallel layers behave as two resistances in parallel. The resulting resistance is lower than the resistance of the individual layers. No obvious qualitative changes or distortions are made to the pressure distribution except for the fact that the modelled overpressure in general is higher. However, calibrating the Brent overpressures seems to be even more difficult than in the previous model. Tuning the overpressure in the important 35/08- and 35/11-transition zone leads to larger deviations than previously in the Gullfaks/Visund area. In addition, some area undergoing intense quartz cementation (i.e. the 30/02-02 area) is difficult to drain sufficiently. Finally, it seems that including both the Brent Group and Statfjord Formation increase the validity of the model.

Table 6.4: Pressure deviation table for the single layer simulation in the North Viking Graben.

Well	Measured overpressure (bar)	Modelled overpressure (bar)	Deviation (bar)
30/02-02 (Br)	273.1 - 281.2	371.9	90.7
30/03-02 (Br)	26.6 - 36.3	190.4	154.1
31/02-01 (Br)	1.1 - 2.6	0.0	-1.1
31/02-05 (Br)	0.0 - 2.9	0.0	0.0
31/02-08 (Br)	3.5 - 4.1	0.0	-3.5
31/03-03 (Br)	1.7 - 2.2	0.0	-1.7
34/02-04 (Br)	181.6 - 228.0	289.0	61.0
34/08-02,03 (Br)	131.4 - 137.9	230.3	92.4
34/10-23 (Br)	364.1 - 368.0	339.6	-24.5
35/03-04 (Br)	28.0 - 44.3	199.3	155.0
35/08-01 (Br)	180.6 - 188.7	249.9	61.2
35/08-02 (Br)	150.5 - 164.2	238.8	74.6
35/08-03 (Br)	163.7 - 172.4	232.0	59.6
35/11-01 (Br)	0.0	0.0	0.0
35/11-02 (Br)	126.6 - 141.1	222.9	81.8

Standard deviation = 72.1

Mean deviation = 50.7

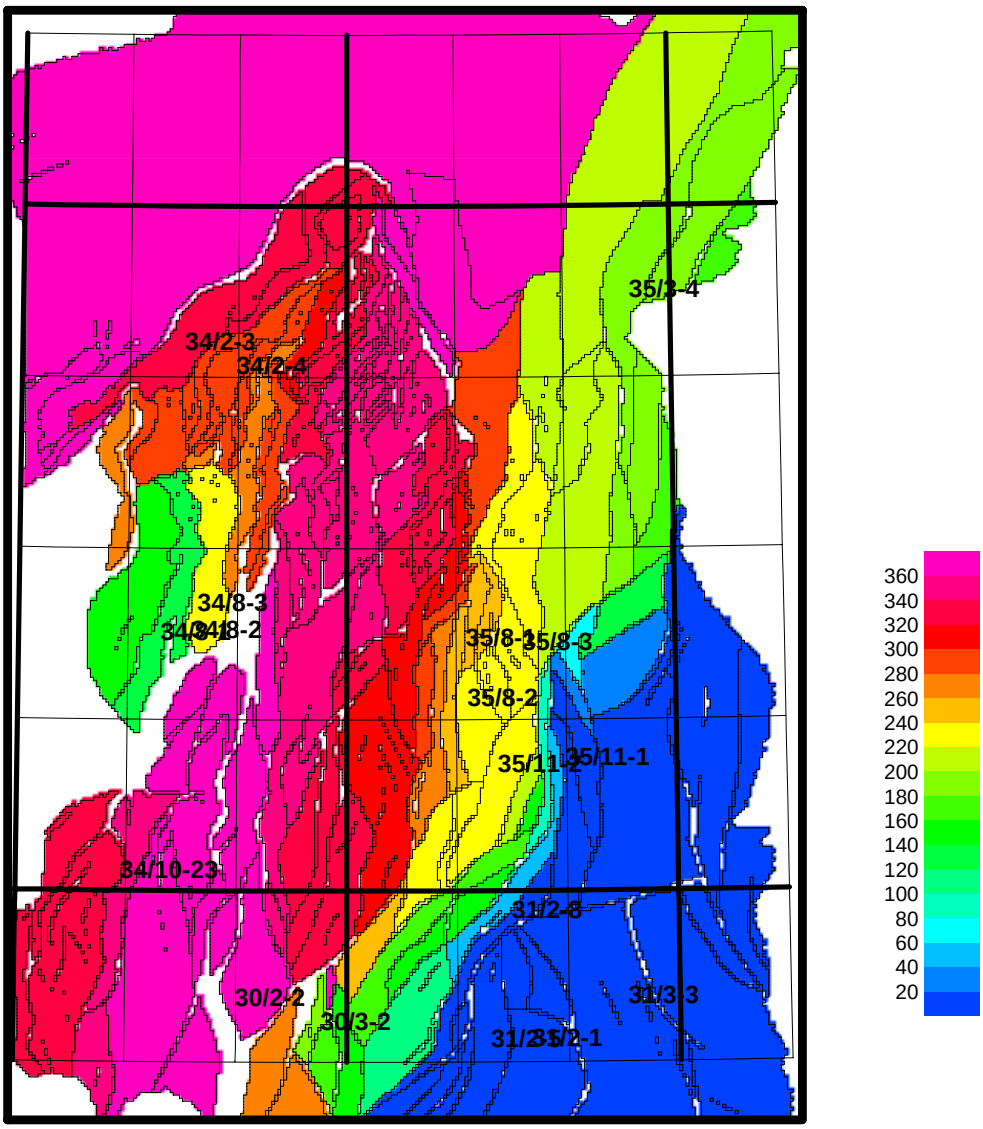

Figure 6.20: The modelled present day overpressure (bar) *in the North Viking Graben using only the Brent Group as reservoir layer.*

6.2 Pressure simulation in the Haltenbanken area

Figure 6.21 shows the location of the study area while Figure 6.22 shows the Haltenbanken area divided into pressure compartments including fault traces, exploration wells and blocks. Statoil has provided the data used in this section. Table 6.5 lists the parameters used for generating the modelled overpressure in the basin while Table 6.6 shows the parameters that describe the lateral flow. The calibrated overpressure distribution seems to be satisfactory because the mean and standard deviations between the modelled and observed overpressures equal 9.2 and 4.8 bar, respectively (see Table 6.7). In section 6.1 two pressure generation mechanisms are included – quartz cementation of the sands and shale compaction. In this section the shale compaction has been divided into two parts: The pressure generation that takes place in the over- and underlying shales (external shale compaction, abbreviated PEP) and the shale compaction that takes place within the gross part of the Jurassic Fangst Group (internal shale compaction, abbreviated PSC). It is, however, the same model that has been applied to the Haltenbanken study area and the North Viking Graben to generate overpressure caused by shale compaction.

Figure 6.24 and Figure 6.25 show the mean values of the modelled properties for the whole basin. There has been a large subsidence rate in the Pliocene. This dramatic geological event has clearly influenced the mechanisms generating the overpressure and the amount of accumulated overpressure. Since the models describing the compaction of shale are direct proportional to the subsidence rate the modelled percent external shale generated pressure (PEP) and modelled internal shale generated pressure (PSC) increase dramatically in this short period of time. The usually dominating diagenetic compaction model describing quartz cementation generates only about 10 % of the overpressure at one point of time. During the rapid subsidence the modelled overpressures in the pressure compartments increase dramatically. When the subsidence decreases the mean overpressure drops indicating that parts of the pressures were maintained by the mechanical compaction and that the overpressure is a rather dynamic phenomenon. Immediately after the rapid subsidence is finished two million years ago the mechanical compaction generates no overpressure at all according to the model. This is due to the low subsidence rate and the high overpressures which retards mechanical compaction. The mean porosity seems to develop as expected. The mechanical compaction dominates the porosity reduction until recently because the quartz cementation does not reach an intense level until the temperature in the compartments has passed about $130°C$. The reason why the rate of hydraulically leaked formation water increases after the rapid subsidence is that the quartz cementation becomes intense in the compartments that are leaking.

The modelled present day overpressure distribution in the Haltenbanken region plotted in Figure 6.26 is very satisfactory. The very narrow intermediate pressured transition zone

between the hydrostatic eastern parts and the highly overpressured western parts in the north is modelled. Between block 6506/11 and block 6506/12 one single fault defines the transition from very high overpressure to hydrostatic conditions. Even though the modelled overpressure in well 6506/12-4 is about 27 bar higher than the measured overpressure in this well the modelled distribution in this area seems to behave as expected. The measured overpressures inside the large pressure compartment covering most of the blocks 6506/12 and 6507/10 vary between hydrostatic pressure and about 60 bar of overpressure. Sub-seismic faults and hydrocarbon accumulations may explain the pressure variations inside this large cell. However, due to the apparently random locations of hydrostatic and slightly overpressured measurements it is probably the complicated geology in the area that reduces the validity of the concept of pressure compartments. In the southern parts of the study area the transition zone is wider. In spite of the modelled overpressure in well 6406/6-1 is about 25 bar higher than the observed it seems that the modelled pressure transition fulfils the expectations. Only a couple of faults surrounded of a moderate potential changes maintain the major parts of the pressure drop. Figure 6.27 shows the modelled overpressure at four points of time. The two upper plots show the overpressure distribution before the large increase in overpressure about 2 million years ago while the lower plots show the pressure distribution after this modelled increase. Modelled pore pressures and corresponding leak-off pressures for all the compartments are plotted versus depth in Figure 6.35. This plot demonstrates that roughly between 3500 m and 4500 m both hydrostatic and lithostatic pressures are modelled. It seems that the hydraulic fracturing occurring at the same depth interval prevent deeper pressure compartments from reaching the fracture pressure. The plot presented in Figure 6.35 agree very well to Statoil's observations presented by Hay and Hovland, 1993.

Figure 6.29 shows the mean depth of the pressure compartments at four points of time and gives an idea of the subsidence the latest seven million years. Although the whole region has subsided during the period the western highly pressured parts of the basin have gone through the most intense subsidence. Comparing these depth maps to Figure 6.28 reveal the strict relation between depth and modelled present day porosity. In Figure 6.36 the modelled porosities in the compartments are plotted versus depth. As illustrated in the figure all the modelled porosities fall within the area of observed porosities according to Bjørkum et al. (1998a). If data like net/gross ratio, temperature gradient, diameter of quartz grains, fraction of detrital quartz irreducible water saturation or coating factors were available on a compartment level (the values presented in Table 6.1 are used all over the study area) probably more of the outlined observed region in Figure 6.36 would have been covered by the modelled porosities.

The importance of the mechanisms that generate the overpressure varies depending on the subsidence rate, depth and pressure. Figure 6.30 shows that the chemical compaction

dominates the porosity reduction at present day. Although the porosities at the shallow eastern parts of the study area are only influenced by mechanical compaction this contribution is hardly visible due to the low accumulation values at these depths. Immediately after the rapid subsidence was completed two million years ago the mechanical compaction was more or less completely prevented due to the high overpressure as illustrated in Figure 6.31. During the rapid subsidence the opposite situation dominated the pressure situation. Figure 6.32 demonstrates how important the mechanical compaction was three million years ago. Seven million years ago the ratio between the two categories was more balanced as shown in Figure 6.33. This is however not only due to the relatively large subsidence rate. The temperature in most of the compartments was too low for an intense quartz cementation to take place. Conclusively, while the mechanical compaction is most intense at the relatively shallow depths where most of the squeezed formation fluids are allowed to escape the quartz cementation rate reach its maximum level at those depths where the overlying shales is able to seal the carriers. In addition, while the mechanical compaction is retarded by the overpressure the quartz cementation rate is governed by the precipitation rate and is not affected by the pressure.

The modelled properties in the compartment containing the 6406/2-3 compartment (see Figure 6.22 for the location) are plotted versus time in Figure 6.37 and Figure 6.38. Both the subsidence history and generating mechanisms in the 6406/2-3 compartment seem to follow the same trend as the basin. The importance of the chemical compaction is strongly reduced during the period of rapid subsidence between 10 and 3 Ma. Between 7 and 5 Ma the quartz cementation recapture some of its importance because the main parts of the sand reservoirs subside into depths that are favourable to the quartz cementation. After 5 Ma the intensity of the decrease because the deepest parts of the compartments are completely cemented. When the overlying shale sequence is modelled to be completely sealing (accumulating factor equals 1) 3 Ma the overpressure increases dramatically and struggles the external mechanical compaction (PEP). Consequently, the relative importance of the two other generating mechanisms increase until the internal shale compaction is modelled to be more or less finished 2 Ma. Only a short time interval between 2 and 3 million years ago the 6406/2-3 compartment has leaked hydraulically. After this hydraulic fracturing the modelled results plotted in Figure 6.37 indicate that the overpressure has been at least 25 bar below the leak-off pressure. Two million years is probably sufficient time for the observed hydrocarbons accumulated in the 6406/2-3 field to migrate into the trap. This is thus a plausible explanation why there are hydrocarbons in the 6406/2-3 trap in spite of the very high pressure. Equivalent plots are presented in Figure 6.39 and Figure 6.40 for the 6506/12-4 compartment and in Figure 6.41 and Figure 6.42 for the 6506/3-1 compartment. These two compartments are not discussed in detail since with the exception of that the

pressure cell containing well 6506/12-4 does not have any local maximum in the quartz cementation curve at 5 Ma the modelled geological histories are qualitative equal.

In order to support the dynamic description indicated by the modelled results a dissipation test on the study area was carried out. All the pressure-generating mechanisms were turned off and the present day pressure distribution was dissipated for about two million years. Figure 6.43 shows clearly how the overpressures drop all over the basin. Even at large depths more or less all of the overpressures have leaked out. During two million years of dissipation the mean overpressure drops from about 65 bar to below 10 bar as illustrated in Figure 6.44. Figure 6.45 shows that the modelled overpressure in the 6406/2 area drops from above 400 bar to about 50 bar in the same period. This simple test of the lateral flow strongly indicates that the nature of overpressure even at relatively large depths is a dynamic phenomenon in this area.

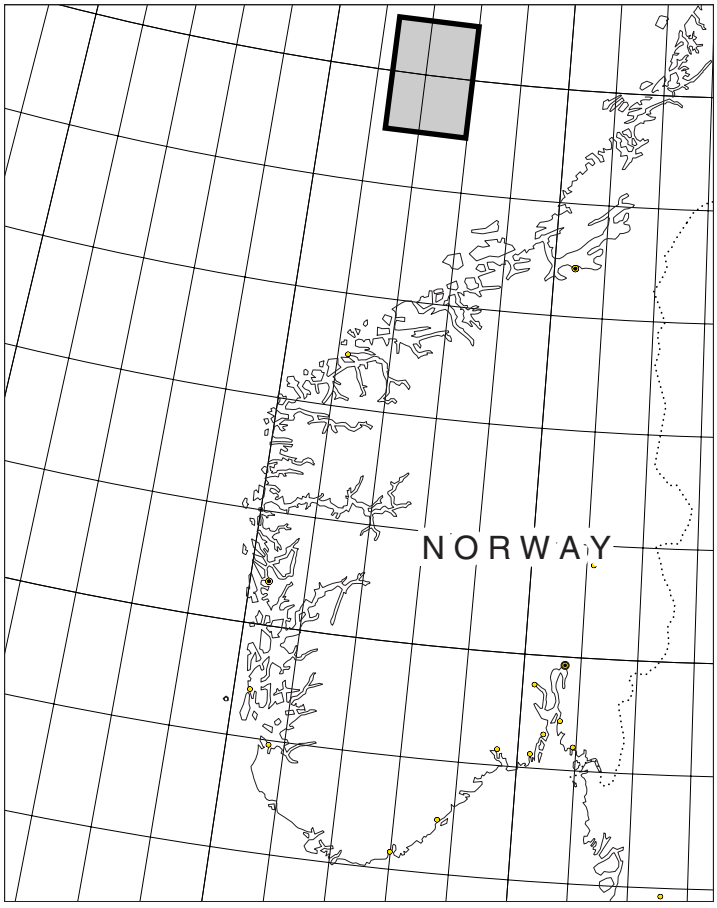

Figure 6.21: The location of the Haltenbanken study area

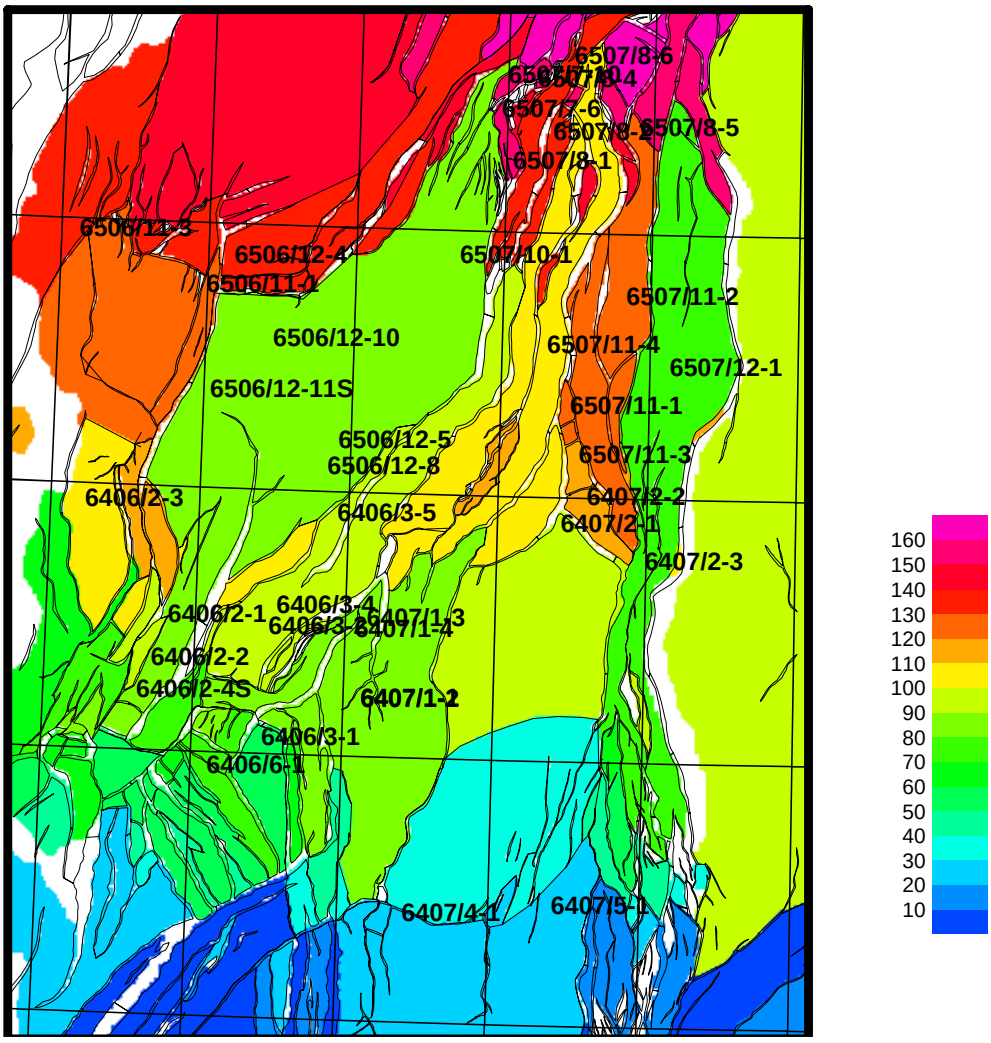

Figure 6.22: Pressure compartments, fault traces and wells in the Haltenbanken area.

Table 6.5: Parameters used for modelling generation and vertical dissipation of overpressure in the Haltenbanken area. (See section 5.1 and 5.2 for an explanation of the variables)

Accumulating depth (m)	z_a	2400
Sealing depth (m)	z_s	3500
Shale sealing thickness (m)	γ	100
Salinity (ppm)	s	50000
Accumulating exponent	A	1.0
Time step (years)	Δt	5000
Diameter of quartz grain size (m)	D	0.0003
Fraction of detrital quartz	f	0.65
Temperature at which quartz cementation starts (°C)	T_{C0}	80.0
Temperature at which quartz cementation is completed (°C)	T_{C1}	175.0
First order leakage coefficient ($\mathrm{bar} \cdot \mathrm{m}^{-1}$)	σ_1	0.160
Second order leakage coefficient ($\mathrm{bar} \cdot \mathrm{m}^{-2}$)	σ_2	$1.02 \cdot 10^{-5}$
Porosity at seabed	ϕ_{S0}	0.50
Porosity-depth constant 1 (m)	η_1	2400
Porosity-depth constant 2	η_2	0.50
Temperature at seabed (°C)	T_0	4.0
Temperature gradient ($°\mathrm{C} \cdot \mathrm{m}^{-1}$)	$\frac{\partial T}{\partial z}$	0.037
Porosity not accessible for quartz cementation (Fangst Group)	ϕ_{C1}	0.04
Clay coating factor (Fangst Group)	C	0.5
Net-gross ratio (Fangst Group)	ng	0.70

Table 6.6: Parameters used for calculating lateral fluid flow in Haltenbanken area. (See chapter 2 for an explanation of the variables)

Percent remaining fault-transmissibility at no overlap	p	0.05
Width of fault blocks (m)	b	25.0
Porosity at seabed	ϕ_0	0.45
Rate of change in porosity versus depth (m^{-1})	c	0.00039
Porosity where the $K - \phi$ curve changes between deep and shallow relationships	ϕ_b	0.10
Permeability where the $K - \phi$ curve changes between deep and shallow relationships (mD)	K_b	0.0000066

Rate of change in fault zone permeability (log) versus depth (log) for shallow faults	δ_{sh}	3.80
Rate of change in fault zone permeability (log) versus depth (log) for deep faults	δ_{de}	5.00

Table 6.7: Pressure deviation table for the Haltenbanken case study. See Figure 6.22 for the locations of the wells.

Well(s) / Block(s)	Measured overpressure (bar)	Modelled overpressure (bar)	Deviation (bar)
6406/3-1	287 - 289	281.3	-5.3
6407/6-2,3	0 - 3	4.2	0.8
6406/6-1	296	320.6	24.2
6407/2-3,6507/12-1	0 -2	0.0	0.0
6407/1-1,2,3,4	0 - 34	40.0	5.9
6506/12,6507/10,6406/2	0 - 59	13.4	0.0
6407/2-1	0	14.5	14.4
6406/3-2,4,5	3 - 10	18.5	8.8
6407/6-1,6507/12-2,3	0	0.0	0.0
6507/11-4	0	0.8	0.7
6407/2-2	0	0.0	0.0
6507/11-3	0 - 3	0.0	0.0
6507/11-1	0 - 5	0.0	0.0
6506/11-1	360	367.3	7.3
6406/2-3,5	421 - 426	419.6	-1.5
6507/8-5,11-2	0	0.0	0.0
6506/11-3	360 - 384	361.3	0.0
6506/12-4	292 - 294	321.5	27.3
6507/8-6	0	0.0	0.0
6507/8-2	4 - 5	0.0	-3.6
6507/7-6,8-1	4 - 20	0.0	-4.3
6507/7-10	7 - 9	0.0	-6.9
6507/8-4	0 - 5	0.0	0.0

Standard deviation = 8.9

Mean deviation = 4.8

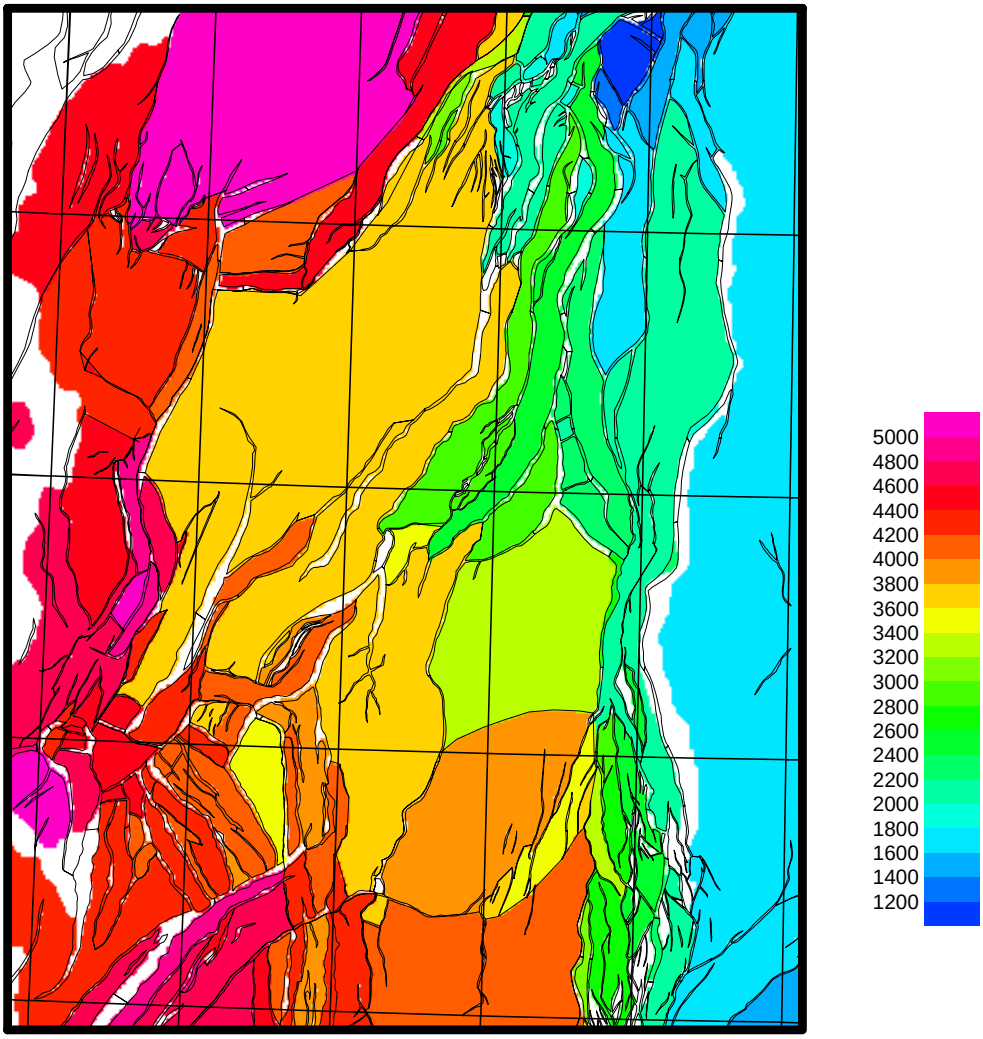

Figure 6.23: Mean depth (m) *of the pressure compartments in the Haltenbanken area.*

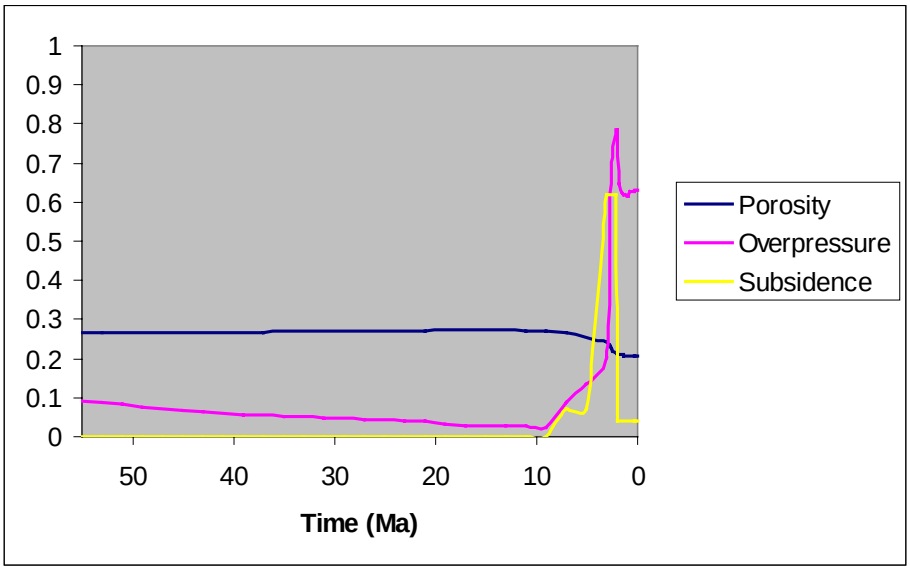

Figure 6.24: *Modelled mean porosity, overpressure* (10^4 bar) *and subsidence* (10^{-5} m/year) *in the Haltenbanken area plotted versus time* (Ma).

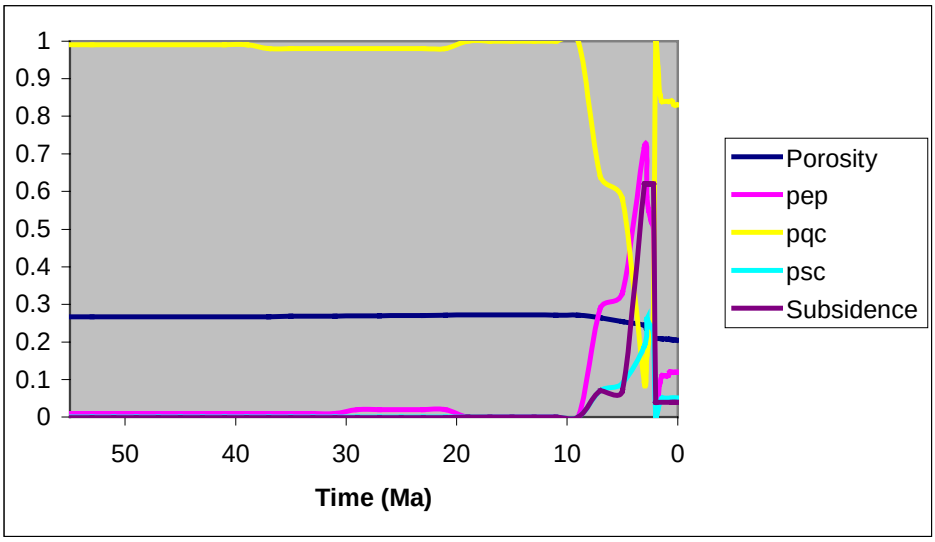

Figure 6.25: *Modelled mean porosity, part of the overpressure generated externally by shale compaction* (PEP), *part of the overpressure generated internally by shale compaction* (PSC), *part of the overpressure generated by quartz cementation* (PQC), *and subsidence* (10^{-5} m/year) *in the Haltenbanken area plotted versus time* (Ma).

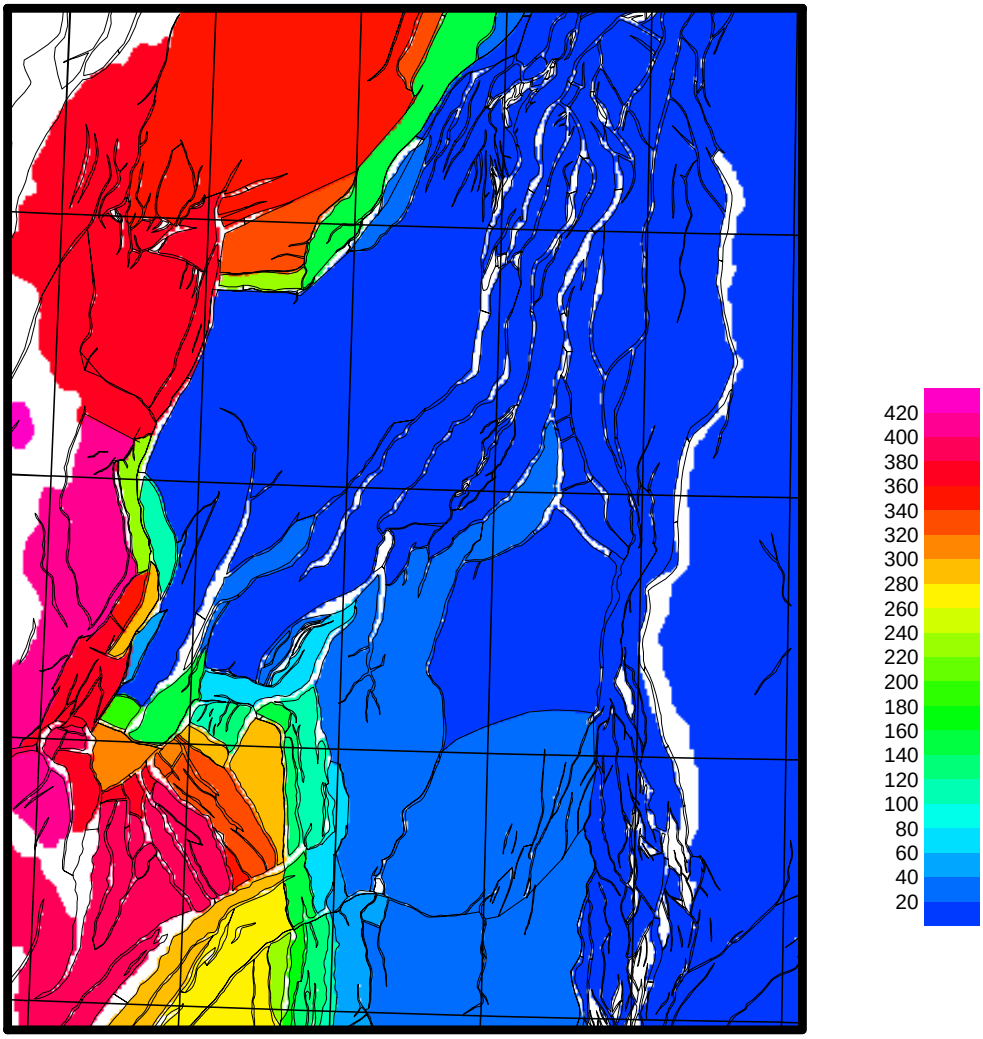

Figure 6.26: Modelled present day overpressure (bar) *in the Haltenbanken area.*

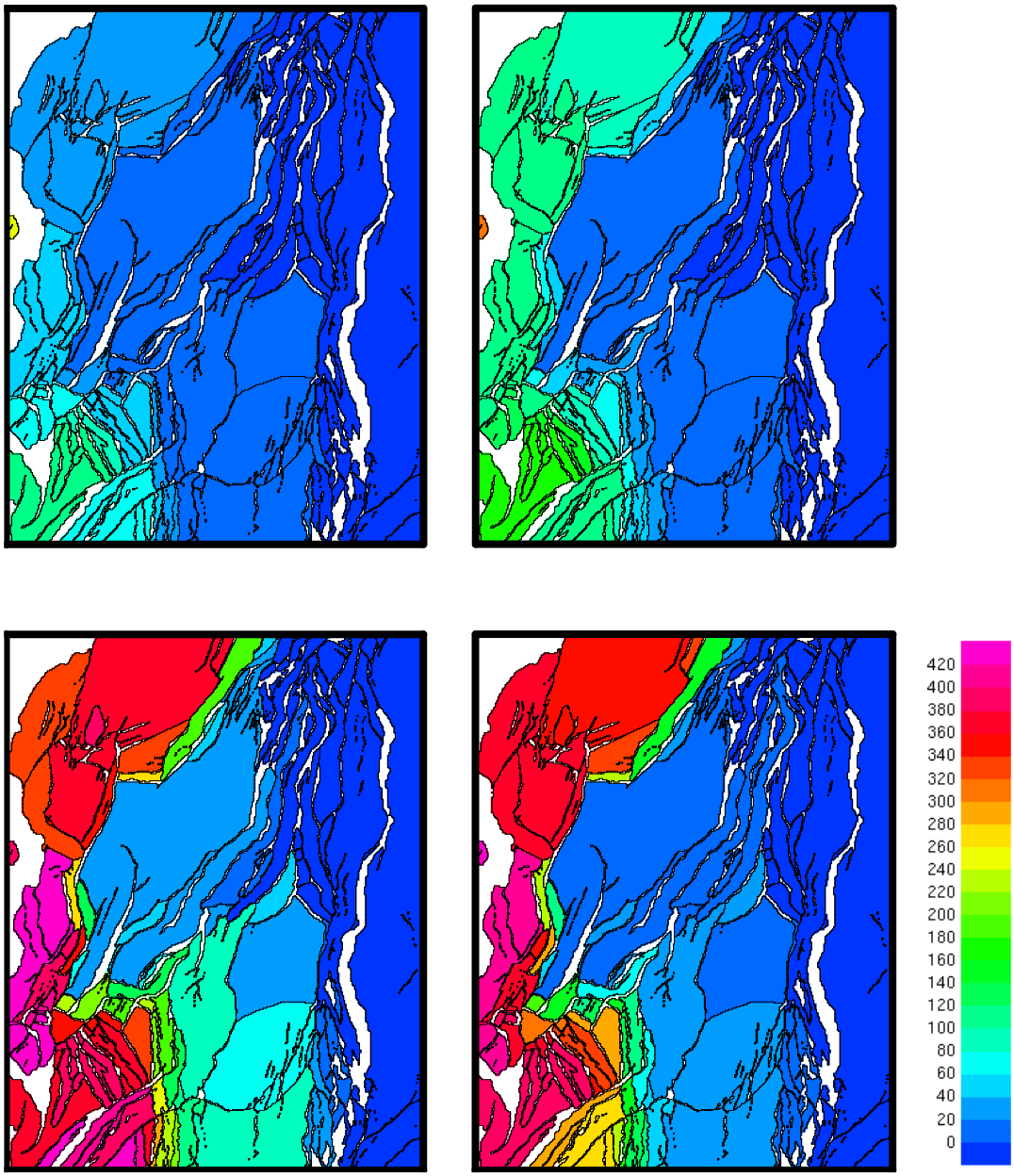

Figure 6.27: *Modelled overpressure* (bar) *at* 7 Ma *(upper left)*, 3 Ma *(upper right)*, 2 Ma *(lower left) and present day (lower right) in the Haltenbanken area.*

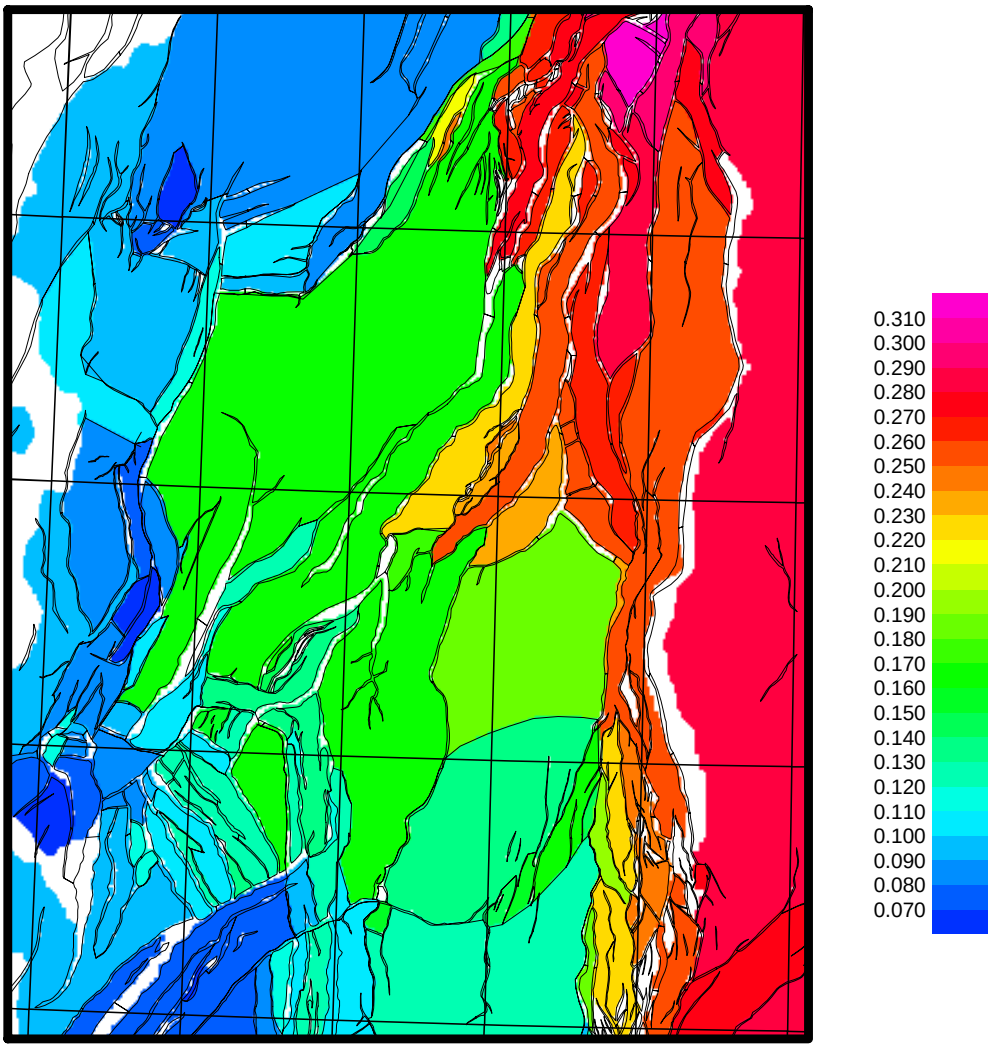

Figure 6.28: Modelled present day porosity in the Haltenbanken area.

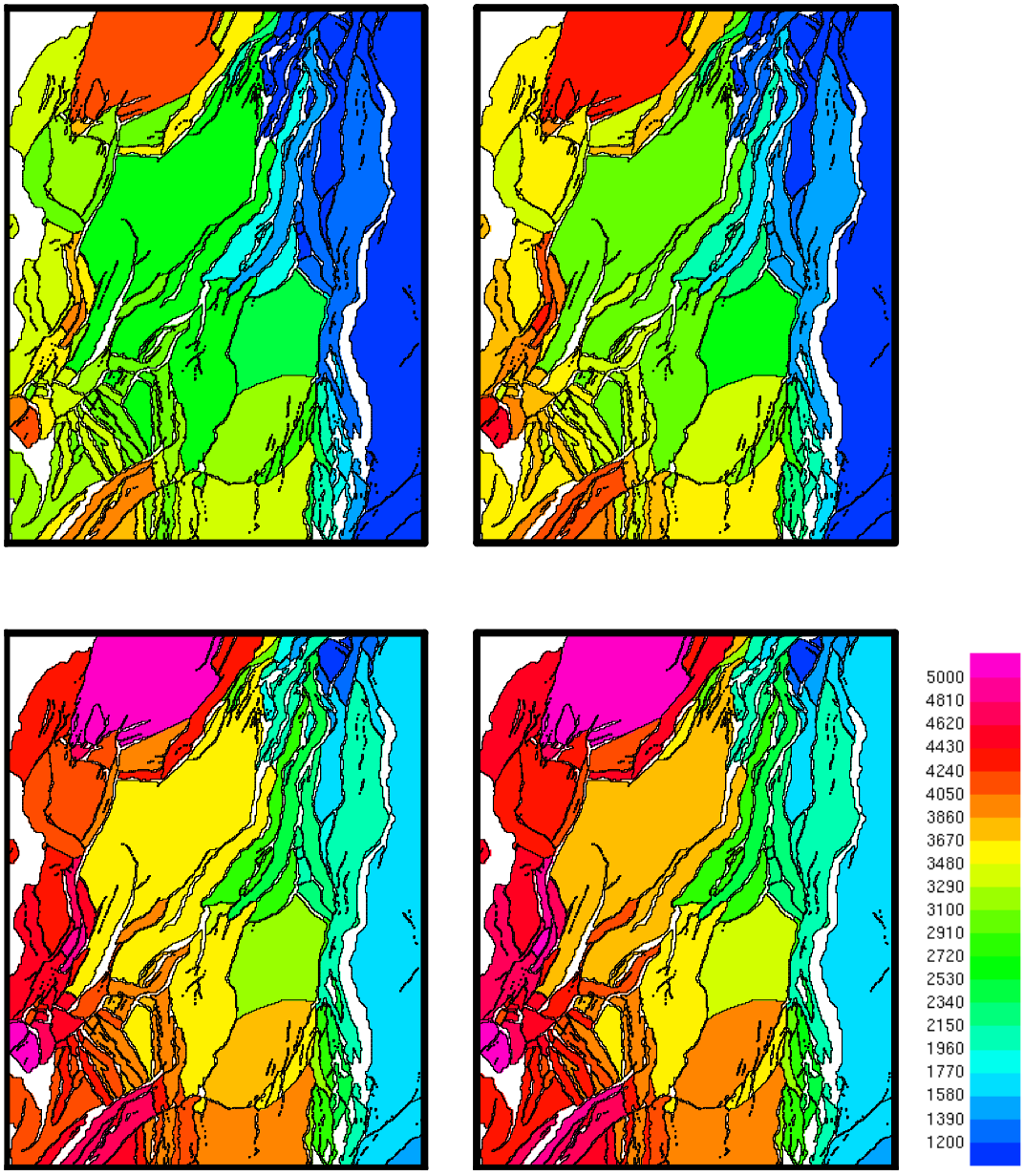

Figure 6.29: *Mean depth* (m) *of the pressure compartments at* 7 Ma *(upper left)*, 3 Ma *(upper right)*, 2 Ma *(lower left) and present day (lower right) in the Haltenbanken area.*

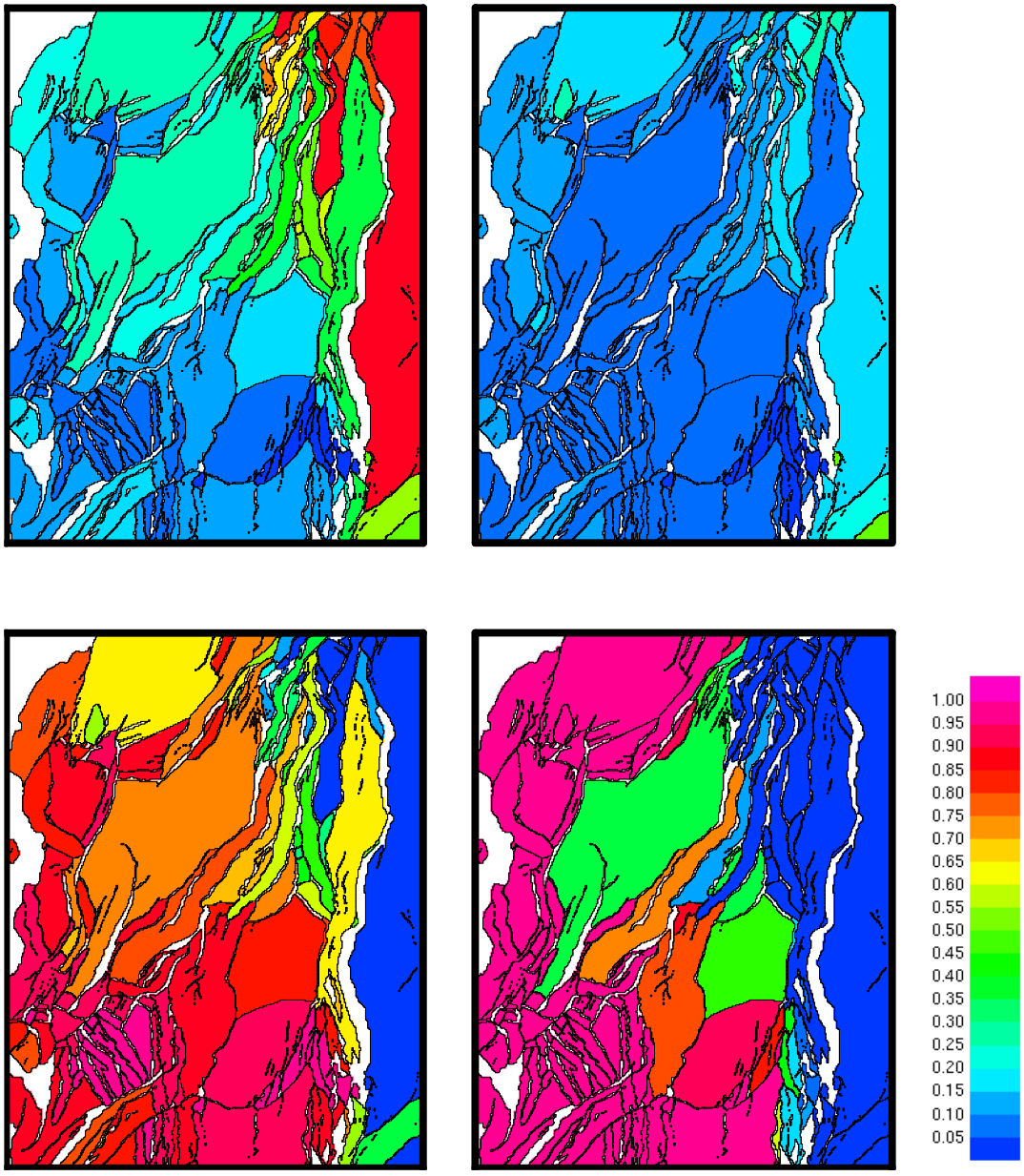

Figure 6.30: *Part of the generated overpressure caused by external shale compaction (upper left), internal shale compaction (upper right) and quartz cementation (lower left) at present day. Part of the generated overpressures that are accumulated (lower right) in the compartments of the Haltenbanken area.*

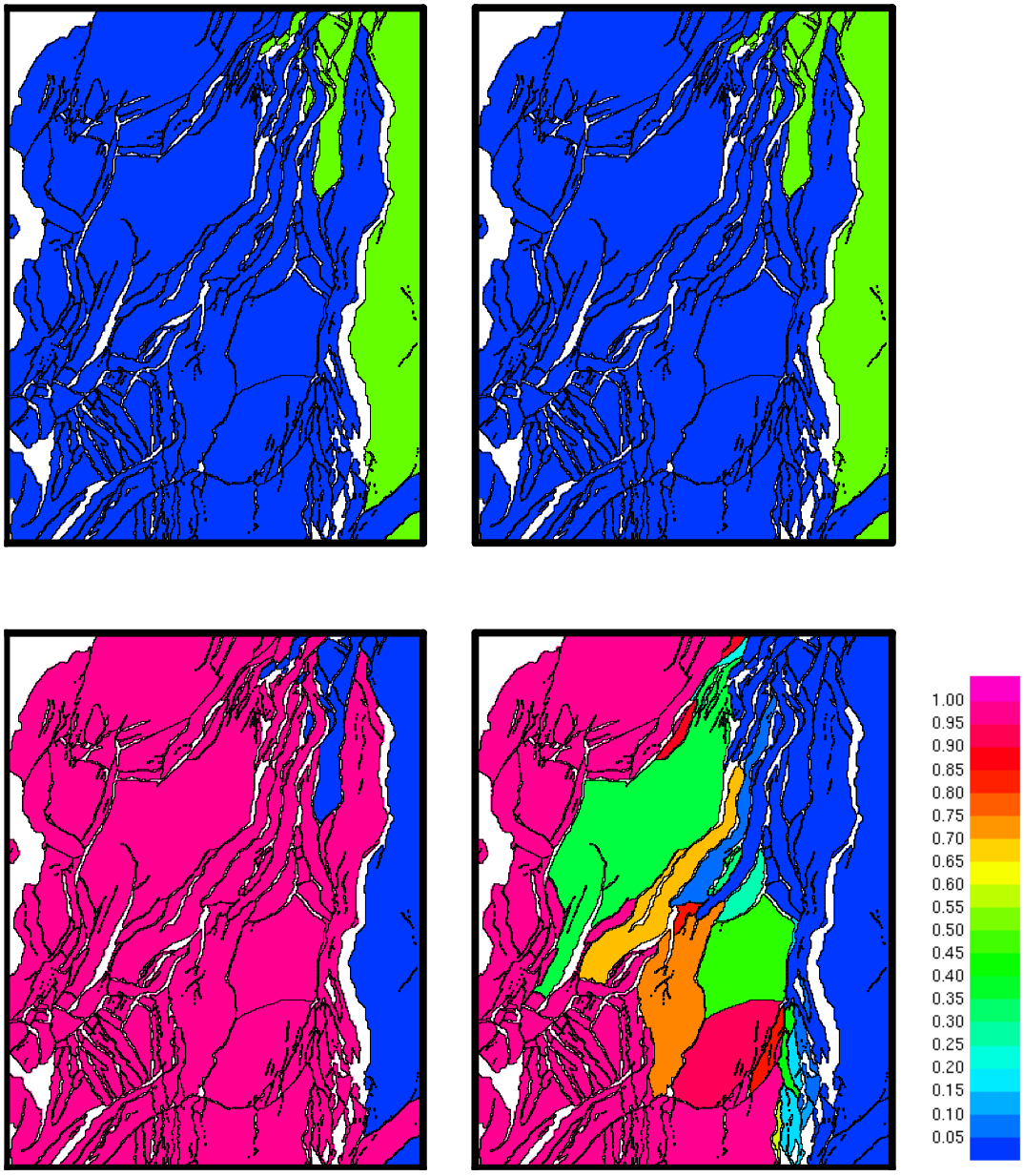

Figure 6.31: *Part of the generated overpressure caused by external shale compaction (upper left), internal shale compaction (upper right) and quartz cementation (lower left) at* 2 Ma. *Part of the generated overpressures that are accumulated (lower right) in the compartments of the Haltenbanken area.*

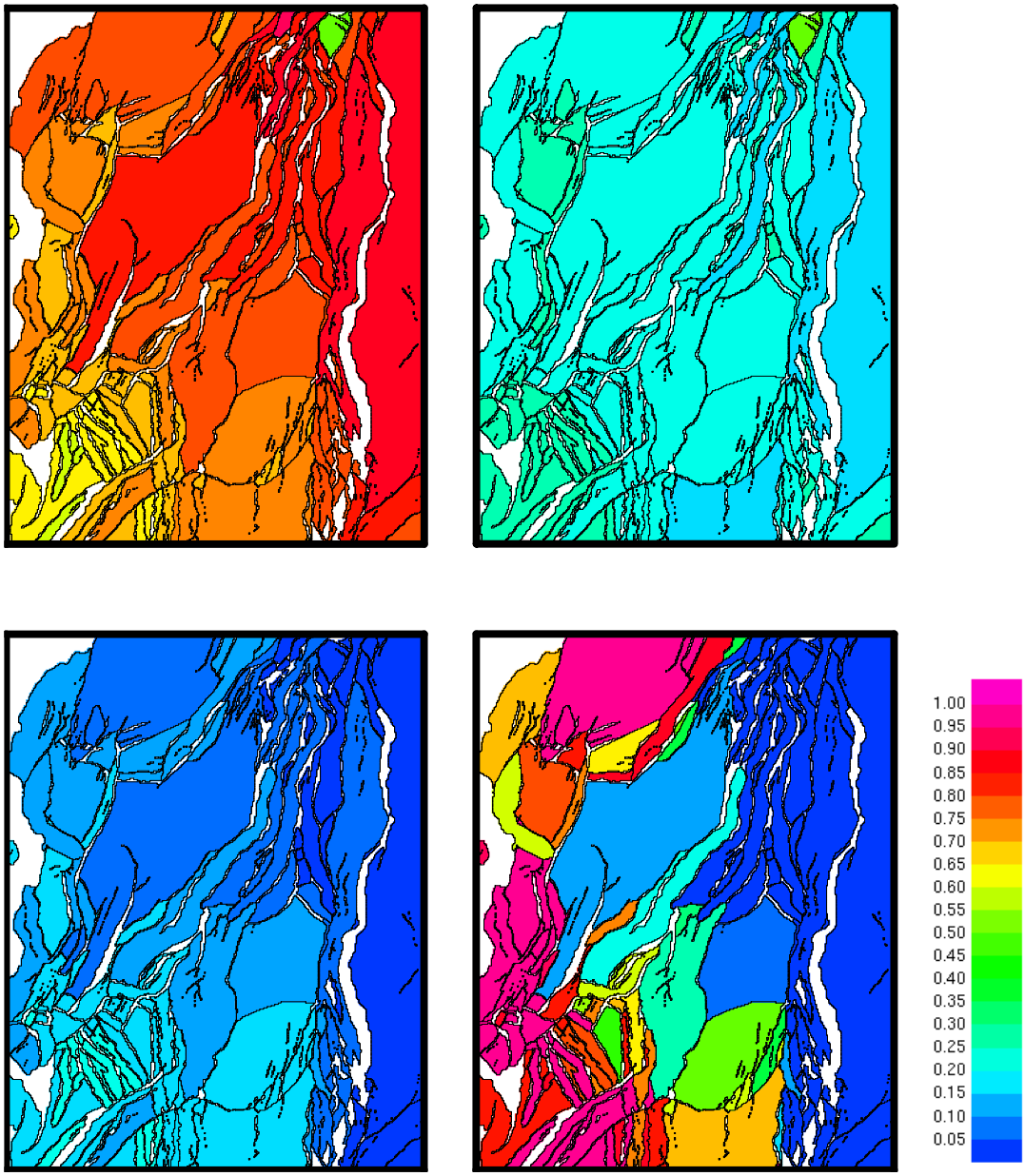

Figure 6.32: *Part of the generated overpressure caused by external shale compaction (upper left), internal shale compaction (upper right) and quartz cementation (lower left) at* 3 Ma. *Part of the generated overpressures that are accumulated (lower right) in the compartments of the Haltenbanken area.*

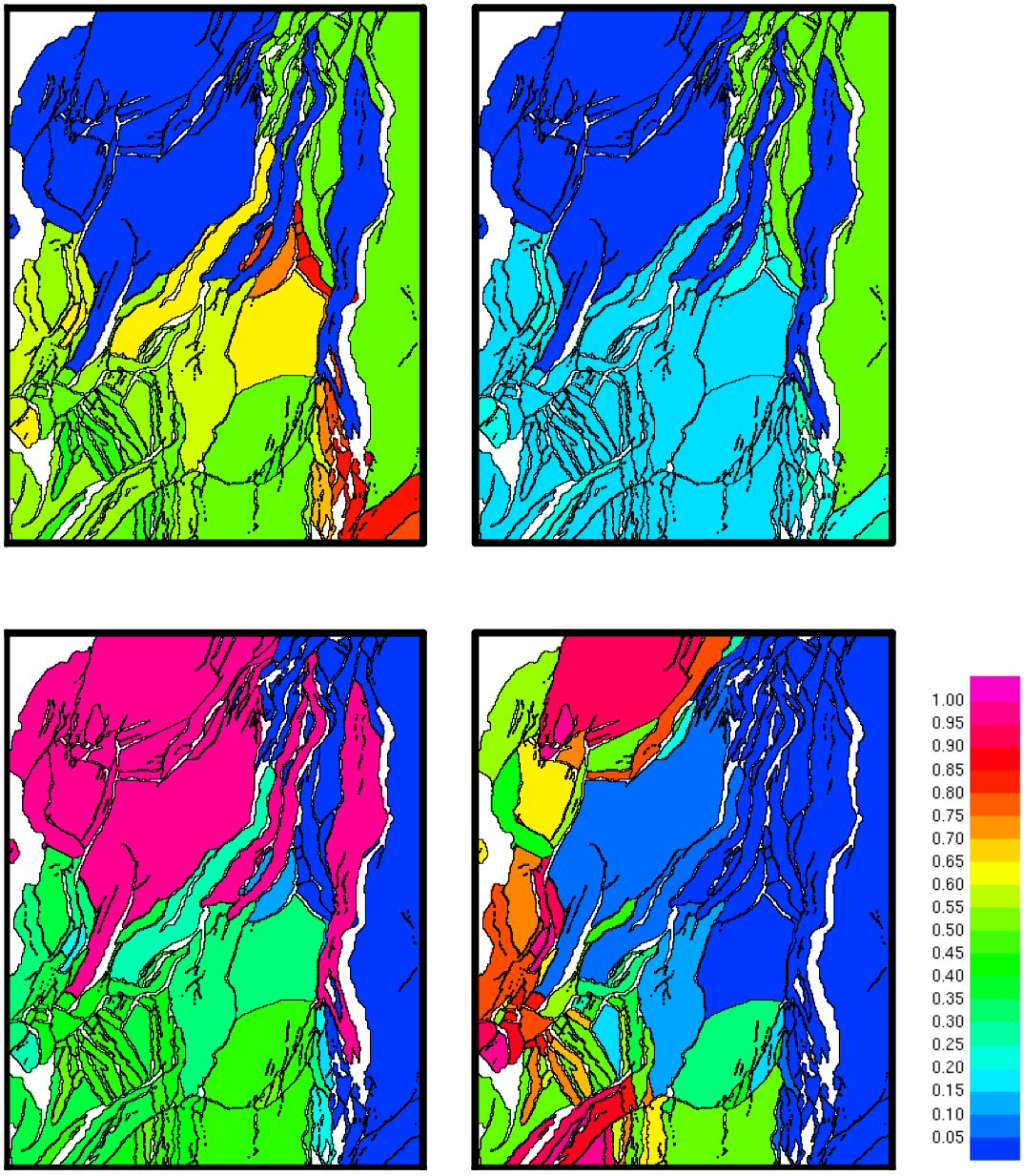

Figure 6.33: *Part of the generated overpressure caused by external shale compaction (upper left), internal shale compaction (upper right) and quartz cementation (lower left) at* 7 Ma. *Part of the generated overpressures that are accumulated (lower right) in the compartments of the Haltenbanken area.*

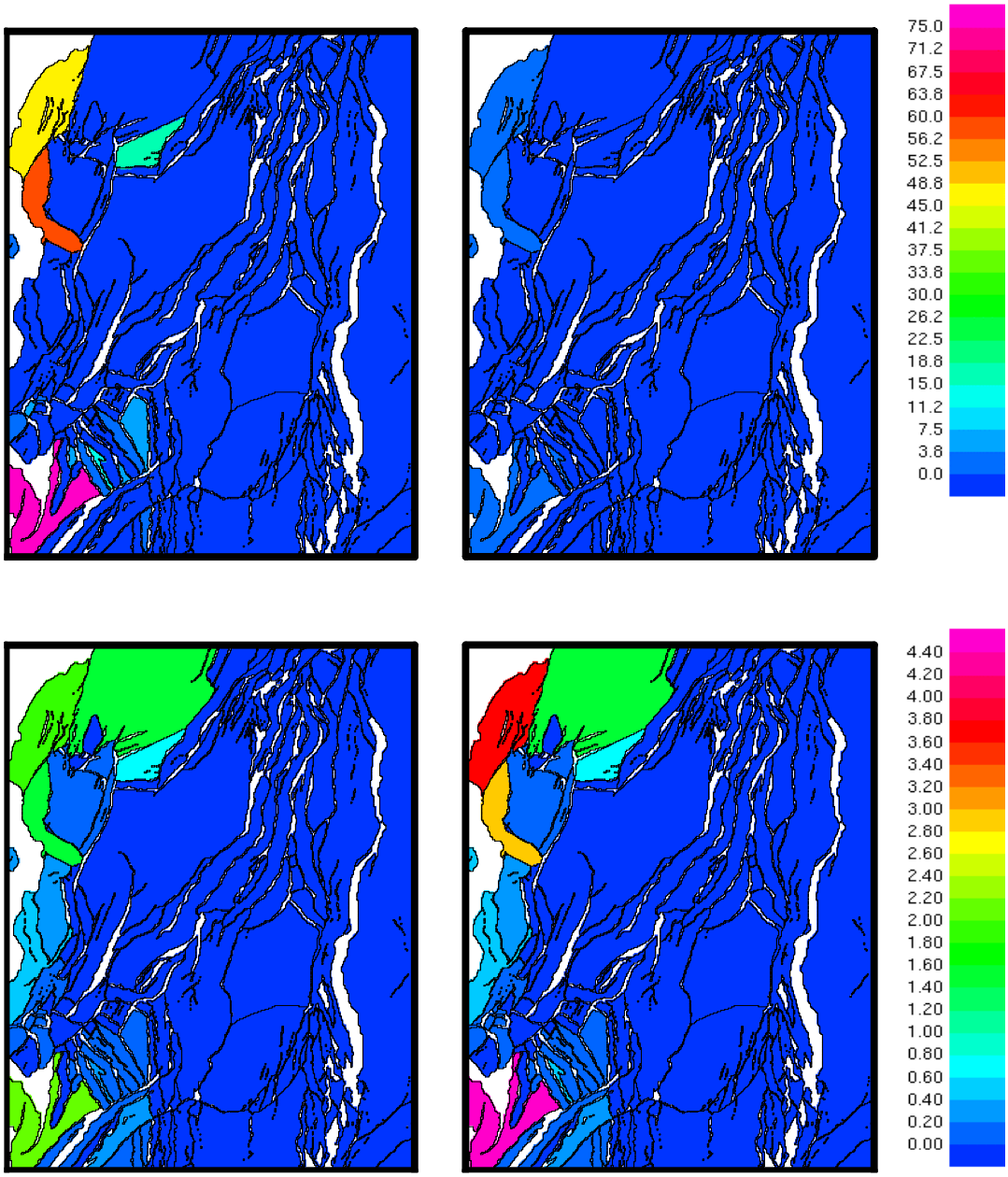

Figure 6.34: *Modelled cumulative hydraulic leakage in the Haltenbanken area at* 7 Ma (*upper left,* 10^4 m^3), 3 Ma (*upper right,* $10^4 m^3$), 2 Ma (*lower left,* $10^7 m^3$) *and present day* (*lower right,* $10^7 m^3$). *The upper scale ranges from* 0 *to* $7.5 \cdot 10^5$ m^3 *while the lower scale ranges from* 0 *to* $4.4 \cdot 10^8 m^3$.

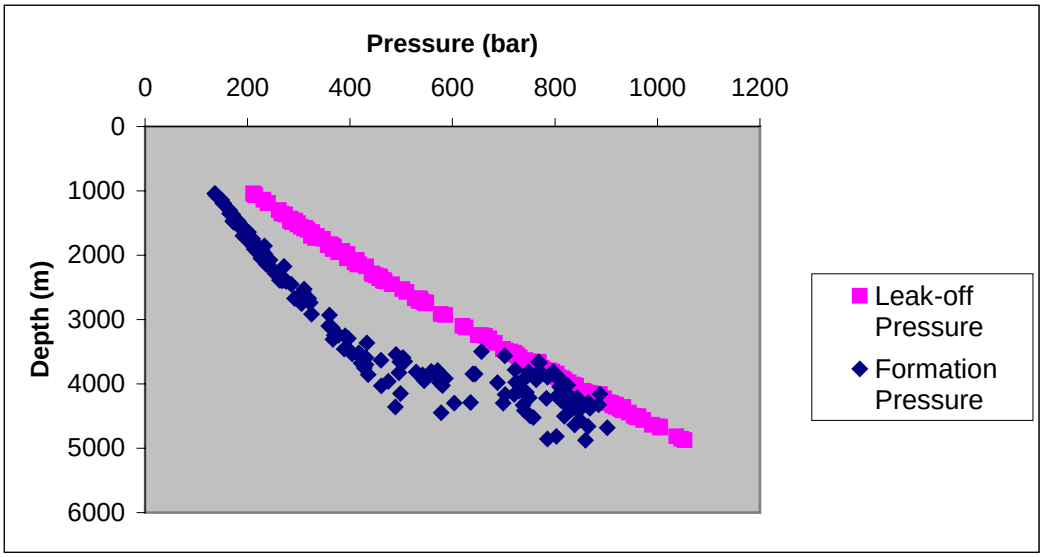

Figure 6.35: *Modelled present day formation pressures* (bar) *and leak-off pressures* (bar) *plotted versus the depth of the top points of the pressure compartments in the Haltenbanken area.*

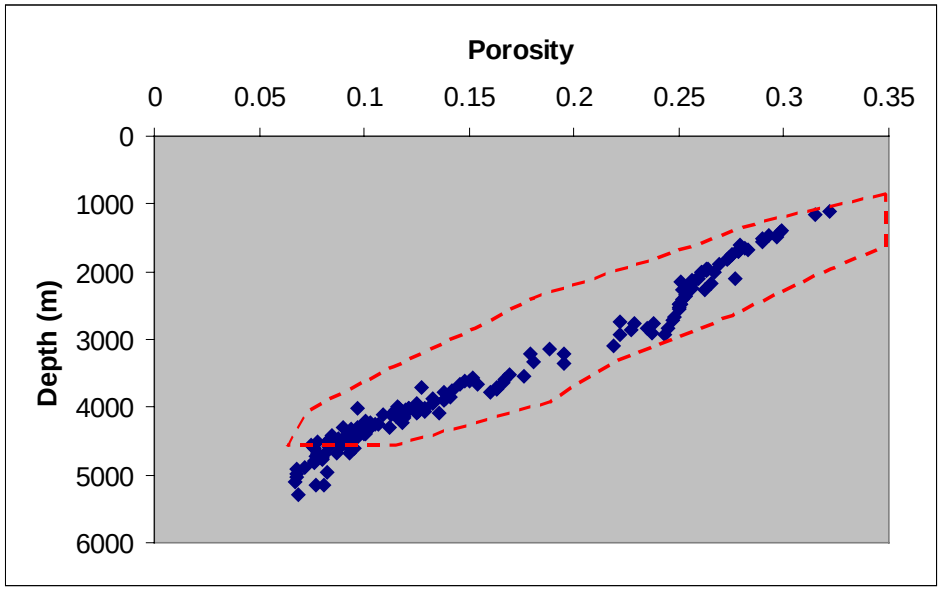

Figure 6.36: *Modelled present day mean porosities of the compartments plotted versus the depth* (m) *including the enveloped area of observed porosities (freehand plot after Bjørkum et al. (1998a)).*

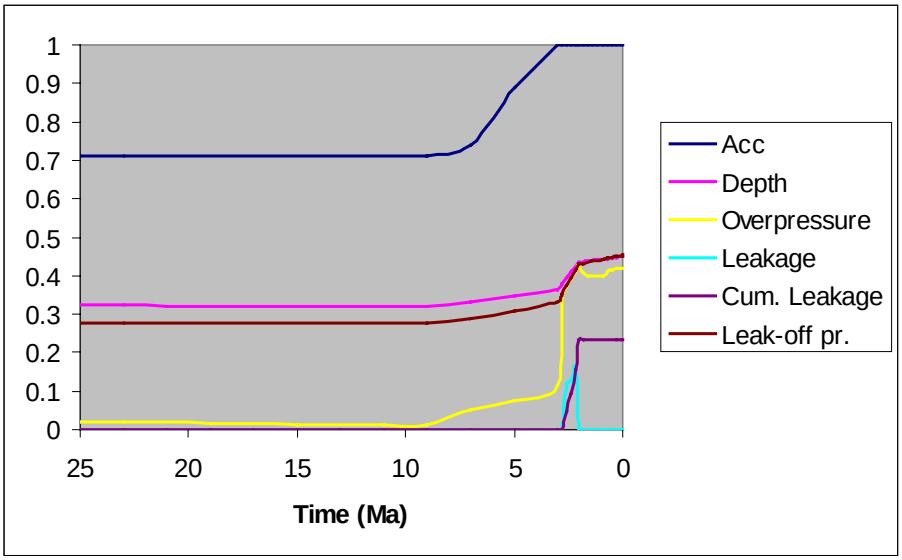

Figure 6.37: *Modelled accumulating factor, mean depth* (10^4 m), *overpressure* (10^4 bar), *leakage* ($2 \cdot 10^2 m^3$/year), *cumulative leakage* ($10^8 m^3$) *and leak-off pressure* (10^4 bar) *plotted versus time* (Ma) *in the 6406/2-3 compartment.*

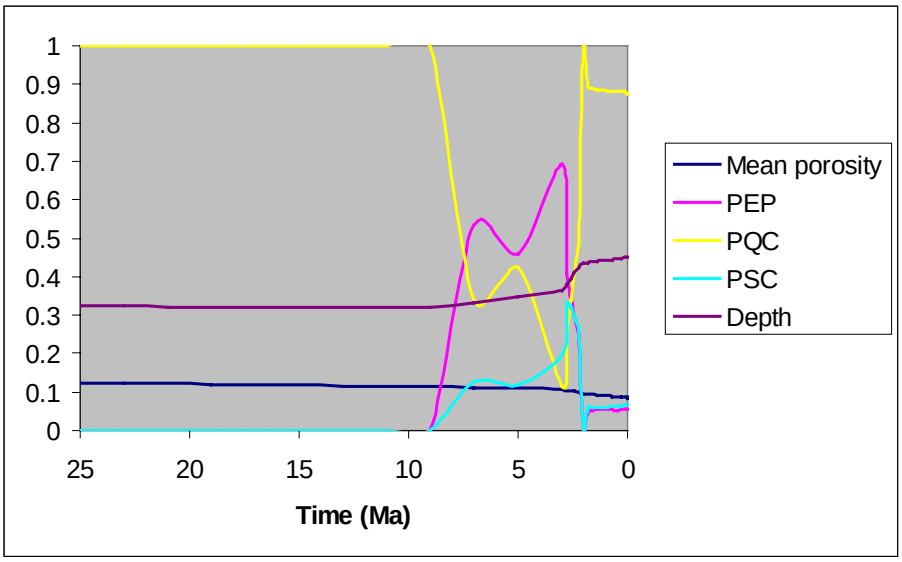

Figure 6.38: *Modelled mean porosity, part of the overpressure generated by external shale compaction* (PEP), *part of the overpressure generated by internal shale compaction* (PSC), *part of the overpressure generated by quartz cementation* (PQC) *and mean depth* (10^4 m) *plotted versus time* (Ma) *in the 6406/2-3 compartment.*

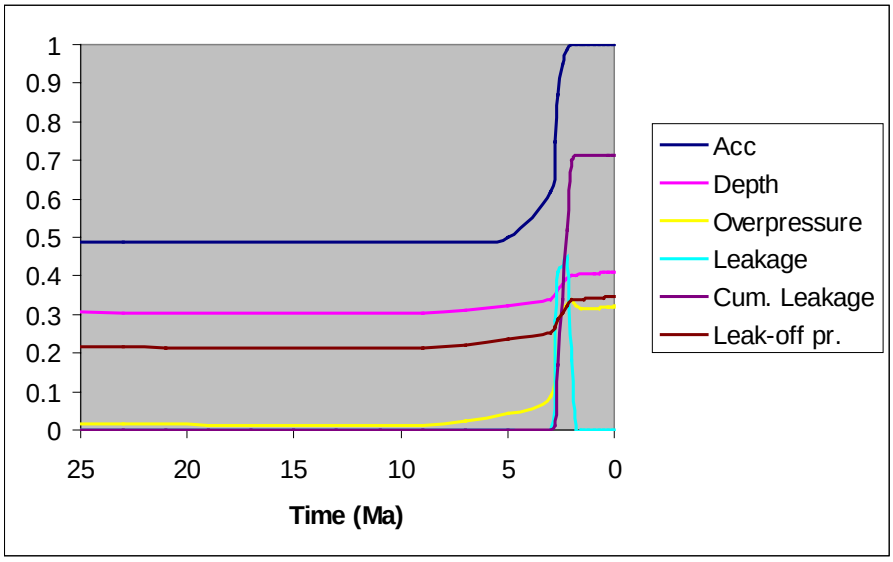

Figure 6.39: *Modelled accumulating factor, mean depth* (10^4 m), *overpressure* (10^4 bar), *leakage* ($2 \cdot 10^2 m^3$/year), *cumulative leakage* ($10^8 m^3$) *and leak-off pressure* (10^4 bar) *plotted versus time* (Ma) *in the 6506/12-4 compartment.*

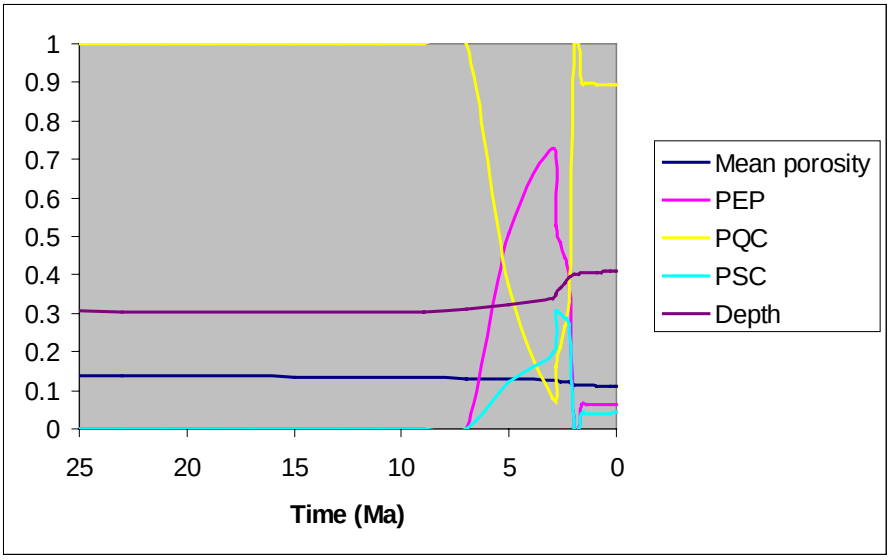

Figure 6.40: *Modelled mean porosity, part of the overpressure generated by external shale compaction* (PEP), *part of the overpressure generated by internal shale compaction* (PSC), *part of the overpressure generated by quartz cementation* (PQC) *and mean depth* (10^4 m) *plotted versus time* (Ma) *in the 6506/12-4 compartment.*

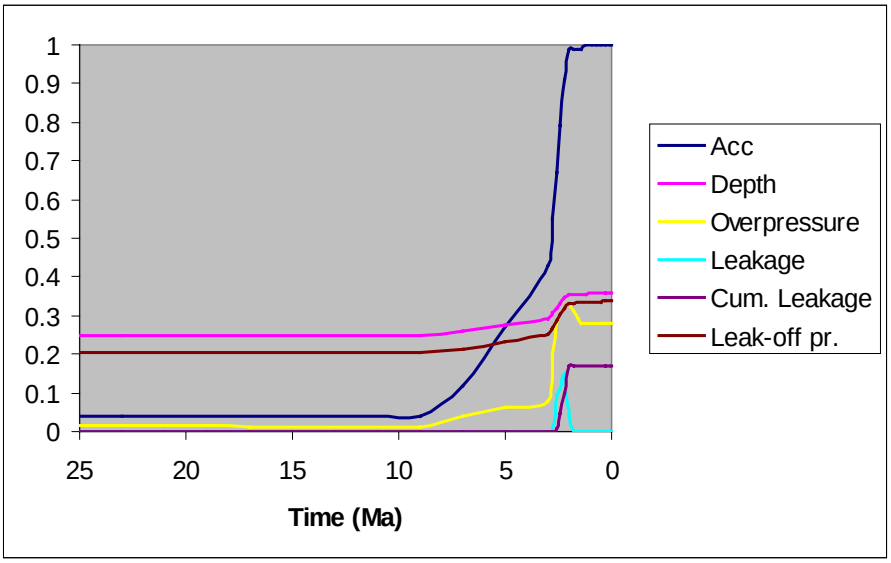

Figure 6.41: *Modelled accumulating factor, mean depth* (10^4 m), *overpressure* (10^4 bar), *leakage* ($2 \cdot 10^2 m^3$/year), *cumulative leakage* ($10^8 m^3$) *and leak-off pressure* (10^4 bar) *plotted versus time* (Ma) *in the 6406/3-1 compartment.*

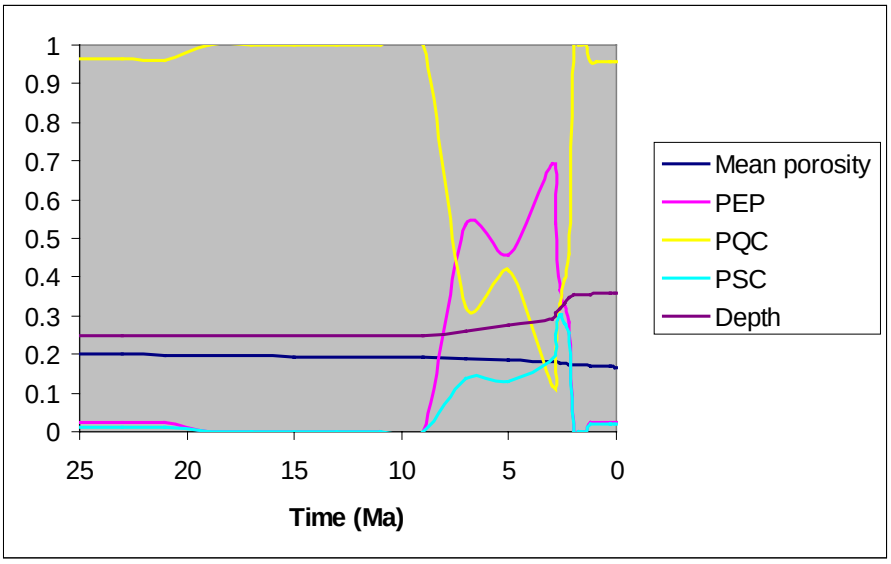

Figure 6.42: *Modelled mean porosity, part of the overpressure generated by external shale compaction* (PEP), *part of the overpressure generated by internal shale compaction* (PSC), *part of the overpressure generated by quartz cementation* (PQC) *and mean depth* (10^4 m) *plotted versus time* (Ma) *in the 6406/3-1 compartment.*

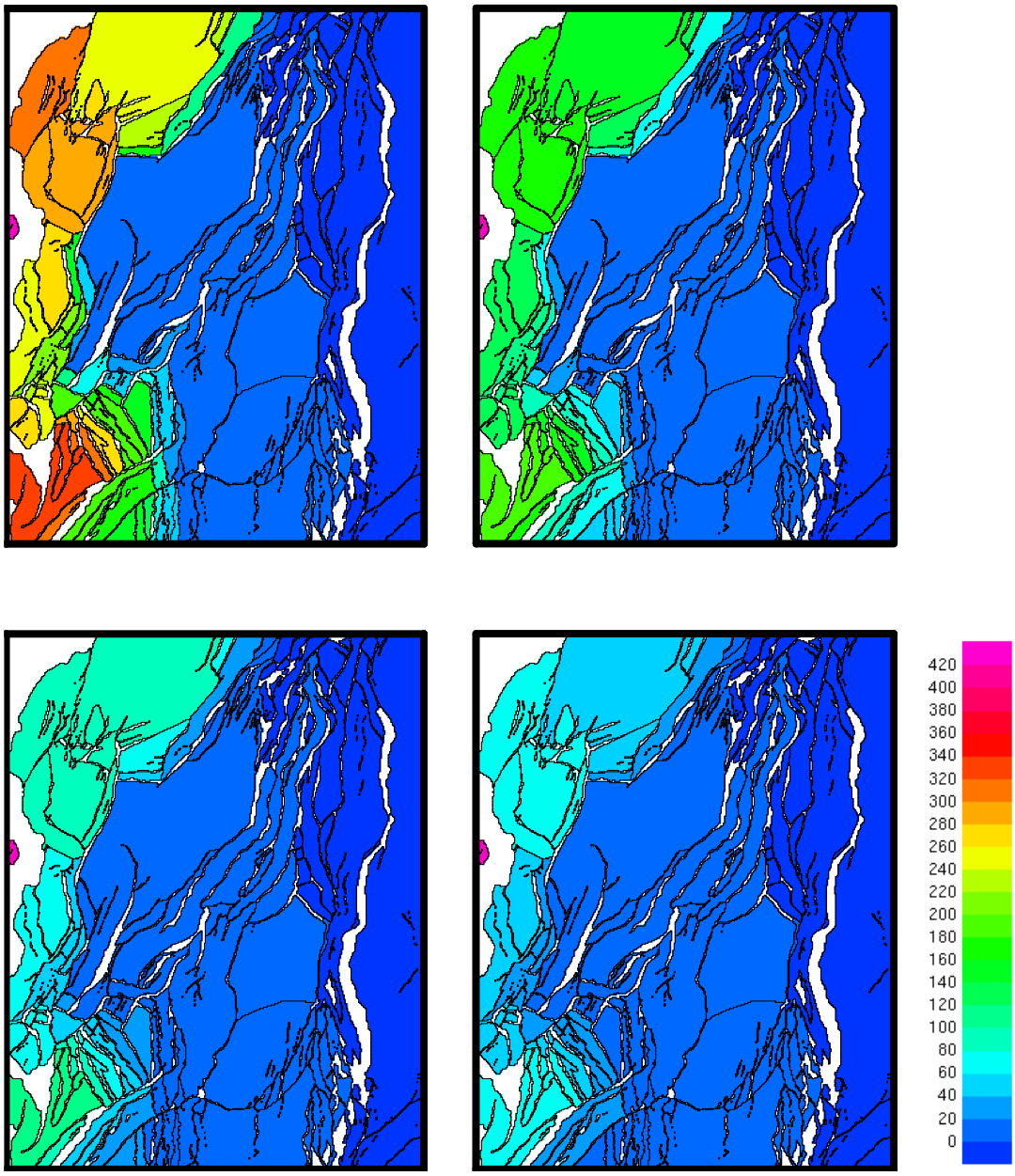

Figure 6.43: *Modelled distribution of overpressure* (bar) *after* 0.1 Myr *(upper left)* 0.7 Myr *(upper right),* 1.3 Myr *(lower left) and* 1.9 Myr *(lower right) of dissipation in the Haltenbanken area.*

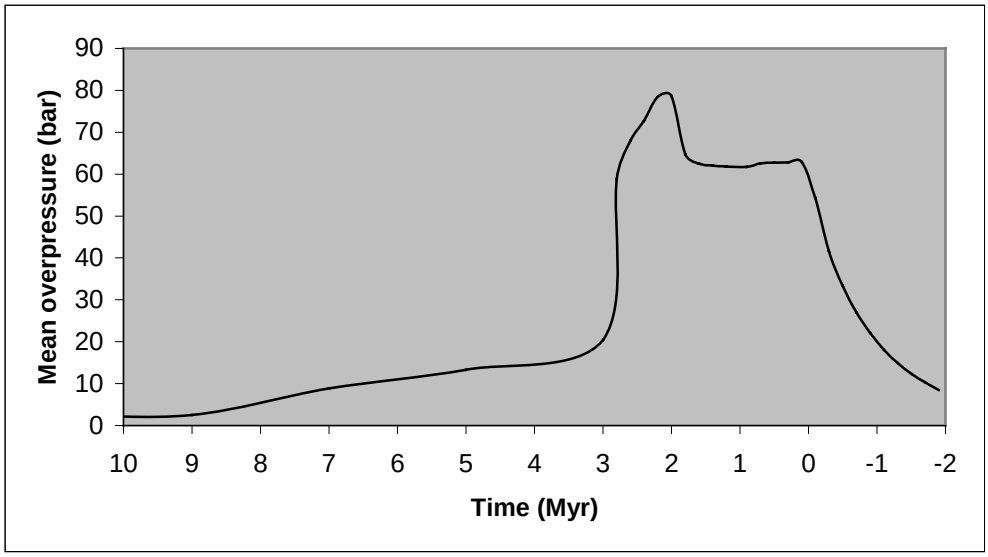

Figure 6.44: The modelled mean overpressure (bar) *in the Haltenbanken area during the last* 10 million years *and during* 2 million years *of dissipation.*

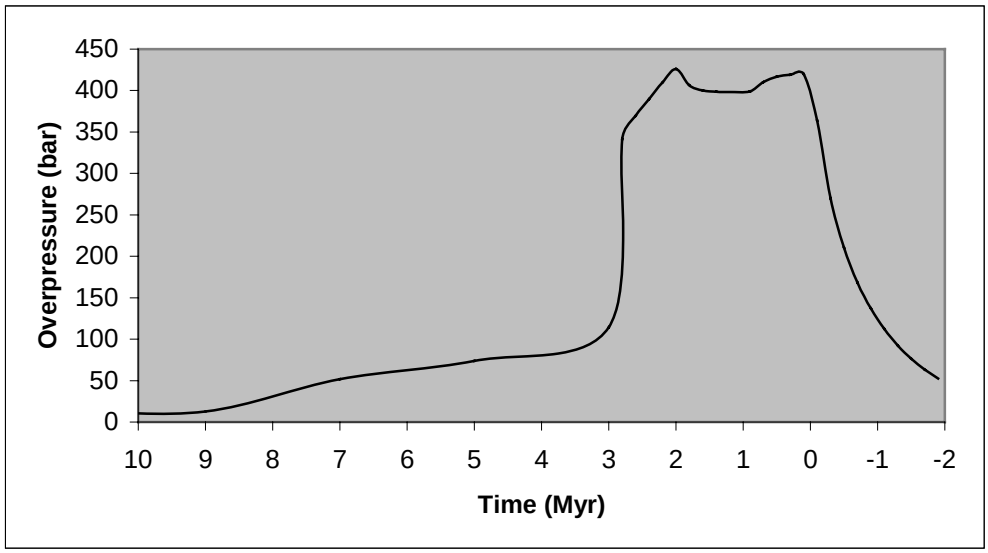

Figure 6.45: The modelled overpressure (bar) *in the 6406/2-3 compartment during the last* 10 million years *and during* 2 million years *of dissipation.*

7. Discussion and conclusions

The ability to consistently and correctly predict pressures is critically dependent upon including all processes relevant to pressure in the model and providing accurate values of the critical parameters (Waples, 1998). The model describing the lateral fault connectivity seems to work satisfactorily to all the models and concepts presented in this thesis. The observed present day overpressures are matched using stationary models, dynamic models, models including boundary compartments and models generating the overpressures within the pressure compartments. The case studies presented in chapter 6, which are based upon generation and dissipation of overpressure on a geological time scale, suggest that the overpressure is a dynamic phenomenon. If this is a real description of the nature of the overpressure, the present day pressure distribution in a modelled basin is very sensitive to the lateral fault transmissibilities. Consequently, the pressure may be calibrated satisfactorily to the observed present day pressures even though the model does not include all relevant processes related to generation and dissipation of overpressure.

The fact that the modelled fault permeabilities from three of the studies vary several orders of magnitudes at different depths (Figure 7.1) leads to the relevant question whether the presented methodology implemented in the PRESSIM simulator contains sufficient parameters to match the observations or is able to reconstruct a likely geological description of the basin. There are 18 and 8 parameters introduced in chapter 2 and 5 describing the pressure generation and dissipation models, respectively. Input data as subsidence rate, faults throws depth- and isopach-maps are more or less completely decisive for the large-scale fluid flow in the basin. 15 of the 18 parameters that describe the generation part of the modelling are to a certain extent constrained by observed or measured values. The model estimating the fault block permeability offers some degree of freedom. Since only 3 of the 8 parameters are loosely constrained the modeller is allowed to adjust the permeability-depth relation to the individual basin. Although it is possible to drain the basin completely or charge it with high overpressures by changing the fault block permeabilities, the ratios between all the lateral fault connectivities are essentially determined by the contact area across the faults rather than the fault block permeabilities. Thus the calibration is primarily concerned with adjusting the model in accordance to the characteristics of the basin.

The modelled fault block permeabilities in the North Viking Graben for the studies presented in chapter 2 and 6 are plotted in Figure 7.1. Although the identical present day data were used in the two studies the permeability values vary several orders of magnitude at depths below 4000 m. Porosity reduction and subsequent generation of overpressure in all the pressure compartments are modelled in chapter 6. The mean porosity is modelled to

decrease approximately 5 % during the simulation according to Figure 6.8. Thus large amounts of formation water has to be drained laterally. This explains the need for the relatively high fault block permeabilities compared to the pressure modelling carried out in chapter 2 where constant porosities are used. It is difficult or impossible to compare the fault block permeability values beyond these obvious differences in methodology. It is thus more relevant to discuss the differences between the modelled fault properties in the North Viking Graben and in the Haltenbanken, which at some depths differ by up to two orders of magnitude. Apparently, this is a rather big difference comparing two basins that do not have very different geological histories. The depth distributions in the basins are very different. While the deepest parts of the Haltenbanken basin are buried about 5000 m at the edge of the study area the North Viking Graben that are buried down to 8000 m influence the fluid flow differently. It is necessary to drain very deep parts of the basin in order to match the observed overpressures. Thus the dominating faults are buried at different depths in the two basins. Figure 7.1 shows that the fault permeabilities between 10^{-6} mD and 10^{-8} mD correspond to the depths of the important faults in both basins. The ages of the faults are roughly the same. This is an indication that kinematic effects as fault diagenesis, which primarily depend upon time and temperature, are more relevant than the stress dependent relation (4, chapter 2) used in the description of the lateral fault connectivity. At depths above 3500 m the faults in the North Viking Graben tend to be more sealing than in the Haltenbanken. In addition to the fault permeabilities the accumulating zone is modelled to introduce sealing effects at shallower depths (Figure 7.2). At these depths the North Viking Graben model has two layers that gradually continue into the partly leaking accumulating zone. The formation water drains more easily towards the flank in a two-layer model than in a single-layer model because the pore water can alternate between the Brent Group and Statfjord Formation in order to find the escape route. The single layer test run in section 6.1 confirms this effect. It is thus not a surprise that the modelled fault zone permeabilities in the North Viking Graben are calibrated to be significant lower than the corresponding permeabilities modelled in the single layer Haltenbanken study.

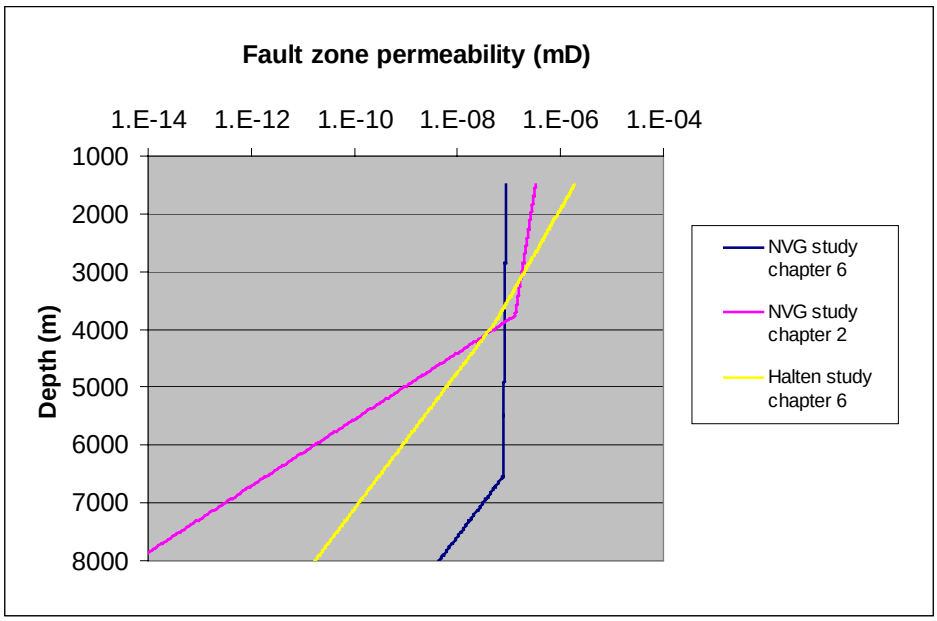

Figure 7.1: *Modelled fault zone permeabilities* (mD) *vs. depth* (m) *in the presented studies*

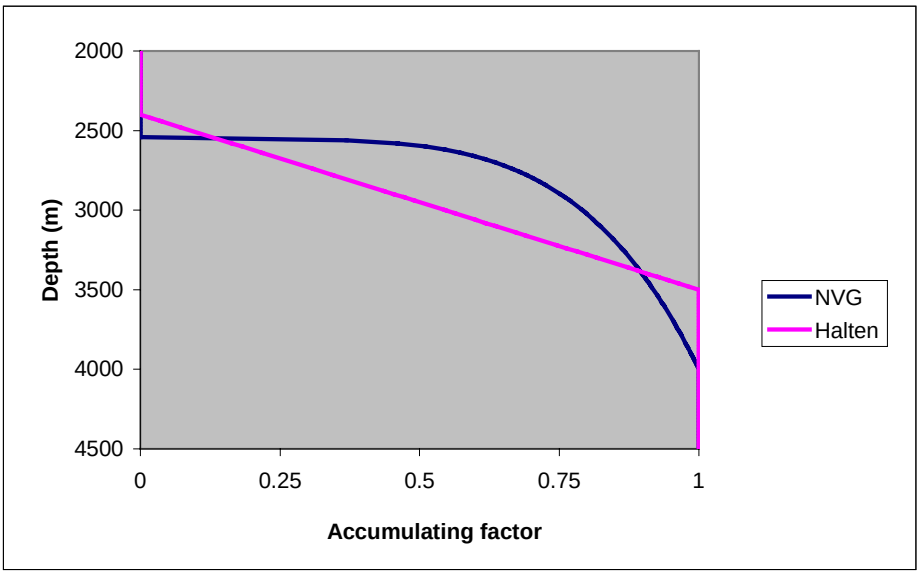

Figure 7.2: *Modelled accumulating zones in the North Viking Graben and Haltenbanken studies*

The simple model estimating the sealing effects of shales represents two important simplifications. Firstly, it is not necessary to carry out the computer intensive vertical flow calculations in the shales. Secondly, the model estimates the sealing effects of the accumulating zone introduced in chapter 5 without assuming a specific flow regime. The vertical leakage is calibrated together with the lateral dissipation to match the observed overpressure, because there is no way to calibrate this flow directly. The modelled accumulating curves in Figure 7.2 correspond well to the observed overpressures in the North Viking Graben and Haltenbanken area. Both basins have large variations in the overpressures between 2500 m and 4000 m. The rapid increase in the modelled accumulating factor in the Haltenbanken area (Figure 7.2) probably reflects a narrow transition zone for the overpressure distribution in the basin (Figure 6.26). The shales are able to confine overpressure on a geological time scale if the permeability approaches 10^{-21} mD – 10^{-23} mD (Deming, 1994, He and Corrigan, 1995). The concept of the accumulating zone is compared to Darcy flow in chapter 5. Results from the North Viking Graben showed that most of the estimated shale permeabilities fall within the confining interval (Figure 5.7 and Figure 5.8). The estimated shale permeabilities vary approximately one order of magnitude with depth. These variations are most likely caused by different pressure response from the different pressure compartments. Conclusively, the accumulating zone introduced is a well suited for estimating vertical fluid flow on a basin scale due to its simplicity, flexibility and ability to match the observed overpressures.

The fact that the description of the lateral flow is able to match the observed overpressures both in a static present day model and in a forward dynamic model does not mean that the different models are able to calibrate any present day pressure distribution. The overpressure is modelled to be dynamic and thus the present day description of the fault properties is very important in calibrating the present day overpressure distribution. Apparently, it seems more important to refine the lateral fault description rather than to model the geological history. This is, however, not the case because in parts of the basin where the quartz cementation is intense the temperature- and porosity-histories are very important for the present day pressure generation. Most applications in basin modelling (hydrocarbon migration) require the pressure distribution through time in order to be able to make optimal predictions. It is necessary to do forward modelling to indicate which mechanisms have generated the excess pressure and to know the nature of it. In addition, mechanisms generating overpressure not included in the methodology may require the geological history if included in the future. Additional sources for the pressure will probably not change the modelled pressure distribution or the main conclusions considerably. The changes in the modelled generation will probably be compensated by increased lateral dissipation, increased hydraulic leakage and decreased mechanical compaction.

In similarity to the 1D maturity modelling, which has become common tool for explorationists, the uncertainty of the simple temperature model used in the PRESSIM simulations is large (Waples, 1998). However, increasing both the surface temperature and the temperature gradient by 1°C only cause minor changes to the modelled overpressures in the North Viking Graben study presented in section 6.1. Thus the derived methodology is not very sensitive to the uncertainties in the modelled temperature.

The concept of pressure compartments following the faults in the basin seems to fulfil its expectations. Firstly, the number of pressure cells or grid blocks is minimised to the lowest possible number. This simplification prepares the way for including pressure simulations into basin simulators without dramatic increasing the running time. Secondly, there is no need for a time consuming and routine work representing the faults by a regular grid since the pressure compartments are defined in accordance with the geological conditions and not a numerical grid. This is possible since the transmissibility model used estimates effective permeabilities between the pressure compartments and not permeability reducing factors. Usually there are small variations in the overpressures measured in a pressure compartment and therefore the pressure is calibrated to match a relatively short interval. However, sometimes there exist large differences between the measured overpressures in a compartment and there are no mapped faults from seismic between the measurements indicating a seal. These pressure differences may be caused by a complex structure of the geology that is not covered using the concept of pressure compartments. Another plausible explanation may be that sub-seismic faults, in similarity to the faults revealed by seismic, are barriers to lateral flow. In this case a regular grid of sub-seismic faults, which are less sealing than the faults constituting the compartments, can be added to the basin. It is then possible to model local variations within the pressure cells. A third explanation is that the permeability inside the compartments is too low to admit a free flow. In this case the assumptions backing up the concept of pressure compartments do not hold. The 6506/12 area in the Haltenbanken region presented in section 6.2 is a good candidate for further work on this topic. In this area one big pressure compartment contain several exploration wells where the observed overpressures range from 0 to 60 bar. However, for the cases studied in this thesis it seems that the pressure compartment approach works well. Based upon a 2D model from the Central North Sea, Darby et al. (1998) claim that the fluid flow must be generally restricted by poorly permeable faults. These observations support the view that the faults play an important role in the distribution of overpressure.

The results from the two case studies presented in chapter 6 strongly support the view that the overpressure is a dynamic phenomenon. The curves describing the mean modelled overpressure in the basins (Figure 6.18 and Figure 6.44) seem to decrease exponentially if the generation mechanisms are omitted. In the North Viking Graben the mean overpressure is approximately halved every 1 Myr of dissipation, while the corresponding halving time

in the Haltenbanken area the dissipation is approximately 0.5 Myr. The formation water has to dissipate across more and deeper faults in the North Viking Graben study than in the Haltenbanken model. In addition, width of the intermediate pressured transition zone in the Haltenbanken study is in general narrow compared to the corresponding zone in the North Viking Graben (Figure 6.6, Figure 6.7 and Figure 6.26). Although the fault zone permeability in the Haltenbanken is modelled to be significant lower at large depths (Figure 7.1) the dissipation is not reduced considerably because most of the faults are buried above these depths. The sum of these features explains the differences in the dissipation speed. If the models deduced describe the generation and dissipation realistically, the dynamic nature of the overpressure explains why it is important to calibrate the lateral fluid flow in order to achieve a good match between the observed and measured overpressures in a basin. In addition, the rapid pressure equalisation emphasises the importance of the correct timing of the pressure generation. There exists large variations between different empirical porosity-depth models both for sands, shales and carbonates (e.g. Giles et al, 1998). However, there is a unique trend that the porosity is reduced with the increasing depth. Thus large amounts of low compressible pore fluid has to be drain either laterally or vertically out of the sediments during subsidence. These massive flows are may be the best indication that the overpressure is a dynamic phenomenon.

The gradual transition from high overpressures to hydrostatic pressure slows down the dissipation process. If a considerable rapid change in overpressure occurs in one pressure compartment, e.g. as a result of production of hydrocarbons, the dissipation rates accross its bounding faults will increase. If a pressure compartment has sufficiently high transmissibilities to its neighbouring pressure cells, the lateral dissipation can influence the pressure development even on a production time scale. Thus it may be possible to calibrate the fault transmissibility flow pattern based upon basin modelling and subsequently apply the results to production case studies to investigate the influence of a possible active aquifer providing natural pressure support. There has been considerable discussion within the software and modelling industries about the possibility of linking fluid-flow models with reservoir simulators (Waples, 1998). The results from the simulation of basin scale flow of formation water should be used as boundary conditions for the traditional reservoir simulations. Thus the effect of the natural pressure support from the basin to oil and gas production could be evaluated. Based upon the results achieved in this thesis, further research should be carried out on this topic.

The methodology deduced in chapter 5 provides the ability to model hydraulic leakage. The results from the two case studies in chapter 6 indicate that the probability for hydraulic leakage to occur is largest at the bottom of the accumulating zone. It is possible to accumulate overpressures close to the lithostatic pressures because the generation of

overpressure is relative intense while the lateral dissipation and leak-off pressures are sufficient low. Below the accumulating zone the reduction in porosity seems to be too low for the formation pressures to reach the high leak-off pressures at large depths. Only a small number of the modelled formation pressures exceed the estimated leak-off pressures in the case studies. This is a clear indication of that hydraulic leakage in one pressure cell tends to prevent similar leakage in the pressure compartments nearby due to fairly high lateral connectivities. Thus the methodology presented in this thesis provides an ability to test which prospects that may and may not have been exposed to hydraulic leakage. This is a very useful tool in exploration because hydraulic fracturing and subsequent leakage of hydrocarbons is a large source of uncertainty regarding the prospectivity in overpressured oil- and gas provinces.

The lateral transmissibility model introduced in this thesis seems to predict a satisfactory basin-wide pressure distribution for different methodologies. The description of the lateral connectivity has been relevant both to a reservoir simulator using boundary cells (chapter 2), to a least square solution of the static conditions between pressure compartments (chapter 3) and to the dynamic modelling using the forward Euler technique (chapters 5 and 6). The predictability of the lateral connectivity model has even survived the RGTM-algorithm, which converts the lateral flow between pressure compartments into flow in a regular grid. An obvious conclusion based on these results is that the fault throw and depth to fault to a large extent govern the lateral flow and pressure distribution in a sedimentary basin. However, only the geometrical properties of the faults are used in order to estimate the flow conditions across the faults. The microstructural and petrophysical properties of fault rocks from siliclastic hydrocarbon reservoirs of the North Sea are closely related to the effective stress, temperature and sediment composition at the time of deformation, as well as their post-deformation stress and temperature history (Fisher and Knipe, 1998). Simple models estimating the effects of clay smearing, granulation and diagenesis of the fault materials should be implemented and tested in order to reduce the uncertainties regarding the paleo-transmissibilities. The permeability of fault rocks can vary by over six orders of magnitude, depending on the extent to which the porosity reduction processes have operated (Fisher and Knipe, 1998). Conclusively, the simple model describing the lateral fault transmissibilities seems to estimate a useful common denominator for all these processes. However, further work should be carried out modelling the fault transmissibilities based upon the fault sealing processes. By including the fundamental fault processes into the numerical modelling of basin scale fluid flow it is possible to differentiate the fault transmissibilities in spite of equal geometric properties. This would hopefully lead to an even better calibration of the present day pressure distribution and a better description of the sealing capacities of the faults through time. In addition, more insight into which processes that cause the accumulation of overpressure at the different parts of the basin will be achieved.

In this thesis the mechanisms generating overpressure are categorised into either mechanical or chemical compaction. Empirical porosity depth curves for sands and shales model the mechanical porosity reduction while quartz cementation handles the chemical compaction. It is however, questionable whether mechanical compaction of shales takes place at great depths. Katsube et al. (1998) claim a clear petrophysical distinction between diagenetically altered and unaltered shales. Based upon data from four different basins (Katsube et al., 1998) it seems that the mechanical compaction more or less disappears below a critical depth of burial between 2 km and 3 km depth, approximately. Similarly, Skar et al. (1998) conclude that density log data from the Cretaceous shales on the Halten Terrace offshore Norway do not support compaction disequilibrium as the sole cause for overpressuring below 3-4 km depth. Alternative models for chemical reactions and fluid flow in shales should be obtained in order to improve the knowledge of how the shales influence the large scale fluid flow in the basin. The results from the simulations in this thesis indicate that quartz cementation in average is the dominating pressure generating mechanism unless there is a very rapid ongoing subsidence. In contradiction to the mechanical compaction the quartz cementation is not stress dependent, because it is assumed that quartz precipitation and not dissolution is the rate limiting process. This is a realistic assumption because the formation water is silica saturated. In most cases this is the reason why the chemical compaction is modelled to be the dominating pressure generating mechanism at the depths where this process is intense. At very large depths (below 5 km) the quartz cementation process in the sands is completed and other mechanisms are allowed to dominate the generation and maintenance of the overpressure. If the pore pressure in other sedimentary rocks should be modelled (e.g. chalk) correspondingly mechanical or chemical porosity reducing models have to be provided. In addition, models estimating the pressure generation caused by hydrocarbon maturation should be included to the PRESSIM simulator to stipulate the effect on pressure generation caused by this process.

The models, concepts and ideas introduced and implemented in this thesis are applied to the water phase only. This is not an extensive simplification because water is the phase that dominates the pressure dissipation even in basins containing large amounts of hydrocarbons. Integrating the PRESSIM simulator into a more advanced basin simulator handling three phases may change the overpressures. Accumulations of hydrocarbons cause an additional contribution to the overpressure due to the lower densities compared to the water. In a water-wet reservoir the overpressure in the hydrocarbon phase relative to the water phase is balanced at the fluid interface (Bjørkum et al., 1998b). It is, however, debated whether a water-wet reservoir has a continuos water phase (Clayton, 1999). Overpressure in the hydrocarbon column may thus be disregarded when considering hydrofracturing of water-wet systems. On the other hand, the presence of hydrocarbons

reduces the part of fluid available for diffusional transport of silica and may retard and/or prevent the generation of overpressure caused by quartz cementation. The presence of hydrocarbons has been found to preserve porosity only in sandstones having atypically low stylolite densities (Bjørkum et al., 1998a). Thus the model describing chemical compaction will hardly be influenced if hydrocarbon phases are included in the model.

The numerical algorithm that solves the equations describing the pressure dissipation works satisfactorily on the studies presented in this thesis. Although the simulator often chops the time steps to the order of 1000 years, which is small compared to the geological time scale, it is not obvious that an implicit and more advanced numerical solution method will increase the time steps and thus reduce the execution time. As already mentioned in this thesis, the models describe the overpressure to be a dynamic phenomenon. The algorithms modelling the fluid flow thus have to use small time steps in order to describe the large and quickly changing fluxes between the pressure compartments. The explicit solution technique ensures a rapid and comprehensive feedback among the various processes, provided that the stability problems are overcome (Waples, 1998). If new models generating overpressure are included or case studies suggesting extremely fast lateral dissipations cause the explicit solution method to fail, an implicit solver should be implemented in order to find a converging method.

Bibliography

BALDWIN B, BUTLER C O: Compaction Curves. AAPG Bulletin Vol. 69, April 1985.

BJØRKUM P A, NADEAU P H: Temperature controlled porosity/permeability reduction, fluid migration and petroleum exploration in sedimentary basins. APPEA Journal, Vol. 38, Part 1, 1998.

BJØRKUM P A, OELKERS E H, NADEAU P H, WALDERHAUG O, MURPHY W M: Porosity prediction in quartzose sandstones as a function of time, temperature, depth, styolite frequency and hydrocarbon saturation. AAPG Bulletin Vol. 82, No. 4, April 1998.

BJØRKUM P A, WALDERHAUG O, NADEAU P H: Physical constraints on hydrocarbon leakage and trapping revisited. Petroleum Geoscience, Vol. 4, 1998.

BJØRLYKKE K, HØEG K: Effects of burial diagenesis on stresses, compaction and fluid flow in sedimentary basins. Marine and Petroleum Geology, Vol. 14, No. 3, 1997.

BORGE H, SYLTA Ø: 3D modelling of fault bounded pressure compartments in the North Viking Graben. Energy, exploration and exploitation. Vol. 16, No. 4, 1998.

BOUR O, LERCHE I, GRAULS D: Quantitative models of very high fluid pressure: the possible role of lateral stress. Terra Nova, Vol. 7, No. 1, 1995.

BREDEHOEFT J D, DJEVANSHIR R D, BELITZ K R: Lateral fluid flow in a compacting sand-shale sequence: South Caspian Basin. AAPG Bulletin Vol. 72, No. 4, April 1988.

CLAYTON C: Discussion: 'Physical constraints on hydrocarbon leakage and trapping revisited' by P. A. Bjørkum et al. Petroleum Geoscience, Vol. 5, 1999.

DARBY D, HASZELDINE R S, COUPLES G D: Pressure cells and pressure seals in the UK Central Graben. Marine and Petroleum Geology Vol. 13, No. 8, 1996.

DARBY D, HASZELDINE R S, COUPLES G D: Central North Sea overpressures: insight into fluid flow from one- and two-dimensional basin modelling. In: DÜPPENBECKER S J, ILIFFE J E (eds) Basin modelling: Practice and progress. Geological Society, London, Special Publications 141, 1998.

DEMING D: Factors necessary to define a pressure seal. AAPG Bulletin Vol. 78, No. 6, June 1994.

FISHER Q J, KNIPE R J: Fault sealing in siliclastic sediments. In: JONES G, FISHER Q J, KNIPE R J (eds) Faulting, fault sealing and fluid flow in hydrocarbon reservoirs. Geological society, London, Special Publications 147, 1998.

GILES M R, INDRELID S L, JAMES D M D: Compaction – the great unknown in basin modelling. In: DÜPPENBECKER S J, ILIFFE J E (eds) Basin modelling: Practice and progress. Geological Society, London, Special Publications 141, 1998.

GILES M R, McNUTT J F, JONG M C, KUKLA P, INDRELID S L, KRAAIJEVANGER H, BEYNON G V: Overpressure and their prediction: A review. Extended abstract volume, Geofluids II, 97. Second international conference on fluid evolution, migration and interaction in sedimentary basins and orogenic basins. Edited by Henry et al, 1997.

GORDON D S, FLEMINGS P B: Generation of overpressure and compaction-driven fluid flow in a Plio-Pleistocene growth-faulted basin, Eugene Island 330, offshore Louisiana. Basin Research Vol. 10, No. 2, 1998.

HALL P L: Physical and chemical aspects of the development of overpressuring in sedimentary environments. Clay minerals Vol. 29, No 4, 1994.

HANSEN S: A compaction trend for Cretaceous and Tertiary shales on the Norwegian Shelf based on sonic transit times. Petroleum Geoscience, Vol. 2, 1996.

HAY S, HOVLAND M: Petroleum leakage and seepage in the Haltenbanken region. BP-Statoil alliance. Internal Statoil report 93058422, August 1993.

HE Z, CORRIGAN J: Factors necessary to define a pressure seal: Discussion. AAPG Bulletin Vol. 79, No. 7, July 1995.

HERMANRUD C, TEIGE G M G, VIK E, PAASCH B, WENSAAS L, BOLÅS H M N: Overpressures in shales – do we know what they are and why they are there? – Overpressures in petroleum exploration; Proc. Workshop, Pau, April, 1998. – Bull. Centre Rech. Elf Explor. Prod., Mem. 22, 1998.

HERMANRUD C, WENSAAS L, TEIGE G M G, VIK E, NORDGÅRD BOLÅS H M, HANSEN S: Shale porosities from well logs on Haltenbanken (Offshore mid-Norway) show no influence of overpressuring. Abnormal pressures in hydrocarbon environments. AAPG Memoir 70, 1998.

KATSUBE T J, BLOCH J, COX W C: The effect of diagenetic alteration on shale pore-structure and its implications for abnormal pressures and geophysical signatures. – Overpressures in petroleum exploration; Proc. Workshop, Pau, April, 1998. – Bull. Centre Rech. Elf Explor. Prod., Mem. 22, 1998.

KNIPE R: Faulting processes and fault seal. NPF Special Publication 1. Norwegian Petroleum Society (NPF), 1992.

KOOI H: Insufficiency of compaction disequilibrium as the sole cause of high pore fluid pressures in pre-Cenozoic sediments. Basin Research Vol. 9, No. 3, September 1997.

LAMBERT J D: Numerical methods for ordinary differential systems. John Wiley & Sons, 1991.

LUO X, VASSEUR G: Contributions of compaction and aquathermal pressuring to geopressure and the influence of environmental conditions. AAPG Bulletin, Vol. 76, 1992.

LUO X, VASSEUR G: Sealing efficiency of shales. Terra Nova, Vol. 9, No. 2, 1997.

MANN D M, MACKENZIE A S: Prediction of pore fluid pressures in sedimentary basins. Marine and Petroleum Geology Vol. 7, February 1990.

NEUZIL C E: How permeable are clays and shales ? Water Resources Research, Vol. 30, No. 2, February 1994.

NEUZIL C E: Abnormal pressures as hydrodynamic phenomena. American Journal of Science, Vol. 295, June 1995.

OSBORNE M J, SWARBRICK R E: Mechanisms for generating overpressure in sedimentary basins: A reevaluation. AAPG Bulletin, Vol. 81, No. 6, June 1997.

RIVENÆS J C: A computer simulation model for siliclastic basin stratigraphy. A dissertation for the fulfilment of requirements for the degree of Doktor Ingeniør. The Norwegian Institute of Technology, University of Trondheim, 1993.

ROBINSON A, GLUYAS J: Model calculations of loss of porosity in sandstones as a result of compaction and quartz cementation. Marine and Petroleum Geology, Vol. 9, June 1992.

ROGERS P S Z, PITZER K S: Volumetric Properties of Aqueous Sodium Chloride Solutions. Journal of Physical Chemistry. Ref. Data, Vol. 11, No. 1, 1982.

SKAR T, VAN BALEN R, HANSEN S: Overpressuring in Cretaceous shales on the Halten Terrace, offshore mid-Norway: Nature and causes. – Overpressures in petroleum exploration; Proc. Workshop, Pau, April, 1998. – Bull. Centre Rech. Elf Explor. Prod., Mem. 22, 1998.

SMITH D A: Theoretical considerations of sealing and non-sealing faults. AAPG Bulletin, Vol. 50, February 1966.

STANDING M B: Petroleum Engineering Data Book. The Norwegian Institute of Technology. The University of Trondheim, 1974.

SWARBRICK R E, SCHNEIDER F: Introduction to special issue on overpressure research. Marine and Petroleum Geology, Vol. 16, No. 4, 1999.

WALDERHAUG O: Kinetic modelling of quartz cementation and porosity loss in deeply buried sandstone reservoirs. AAPG Bulletin, Vol. 80, No. 5, May 1996.

WANGEN M: Modeling porosity evolution and cementation of sandstones. Marine and Petroleum Geology, Vol. 15, No. 5, 1998.

WAPLES D W: Basin modelling: how well have we done?. In: DÜPPENBECKER S J, ILIFFE J E (eds) Basin modelling: Practice and progress. Geological Society, London, Special Publications 141, 1998.

WILKINSON M, DARBY D, HASZELDINE R S, COUPLES G D: Secondary porosity generation during deep burial associated with overpressure leak-off: Fulmar Formation, United Kingdom Central Graben. AAPG Bulletin, Vol. 81, No. 5, May 1997.

YANG Y, APLIN A C: Influence of lithology and compaction on the pore size distribution and modelled permeability of some mudstones from the Norwegian margin. Marine and Petroleum Geology, Vol. 15, No. 2, 1998.

YARDLEY G: Can lateral transfer explain the high pressures in the Central North Sea? – Overpressures in petroleum exploration; Proc. Workshop, Pau, April, 1998. – Bull. Centre Rech. Elf Explor. Prod., Mem. 22, 1998.

YASSIR N: Overpressuring in compressional stress regimes – causes and detection. – Overpressures in petroleum exploration; Proc. Workshop, Pau, April, 1998. – Bull. Centre Rech. Elf Explor. Prod., Mem. 22, 1998

Appendix A The SEMI secondary migration program

SEMI is a program for performing multi-layer, secondary migration of oil and gas along decompacted maps in 3 dimensions. Input data are read from grid files and fault trace files. The main migration work is performed using a ray-tracing procedure to simulate what is considered to be a very fast drainage migration from one or more source rocks into their nearest traps. Thereafter, spillage of oil and/or gas is modelled from deeper traps into shallower traps, depending on whether each trap can hold the hydrocarbons that migrate into it or not. Secondary migration losses are computed during the ray tracing according to volumes lost in dead-ends and microtraps, in addition to the required saturation of the porespace of the migration stringers. These saturation requirements are computed from Darcy permeability and relative permeability relationships.

SEMI accounts for cracking of oil and gas within traps, GOR, oil and gas density changes caused by changes in pressures and temperatures. Gas and oil leakage through the cap-rock can be modelled to be caused by leakage and/or hydraulic leakage.

Migration is performed along decompacted layers through time, and the carrier topography may change during subsidence, e.g. basin inversion. Migration considers buoyancy only within each pressure compartment, while several fault type behaviours may be set for migration between pressure compartments, including juxtaposition sealing and low-permeability faults. Pinchouts (stratigraphic traps) are accounted for.

The SEMI program is developed at SINTEF Petroleum Research and is used to calculate the transmissibilities between the pressure compartments according to the models presented in this thesis.

Appendix B The PRESSIM pressure simulator

The PRESSIM simulator was developed parallel to the work presented in this thesis in order to test and verify different models and concepts. The simulator has been coded in C and has been executed on both PC and Unix platforms.

PRESSIM performs single- and multi-layer generation and dissipation of overpressures through geological time based upon the concept of pressure compartments. Two different models for generation of overpressures are implemented. One of the models estimates shale undercompaction while the other models quartz cementation. It is possible to use these two generation mechanisms together or separately. PRESSIM is able to use an arbitrary connectivity model for the pressure compartments.

A forward Euler technique is used for solving the system of linear equations that describes the flow pattern in the basin. Since this simple numerical method is an unstable method an automatic time step chopper is implemented to the dissipation algorithm in order to automatically stabilise the simulations.

The PRESSIM simulator reads input data from three different files. A data file contains information about the size of the compartments, time intervals to be simulated, mean depths, mean thicknesses of reservoirs, shale drainage thicknesses and depths to the top and bottom points in the compartments. An input file contains the values of the parameters that describe the generation models. The transmissibility file describes the connectivities between the pressure compartments. The SEMI simulator described in Appendix A can provide all these three files.

PRESSIM provides information about modelled pressure, shale draining efficiency, generating mechanisms and hydraulic leakage both at compartment- and at basin-scale. SEMI (Appendix A) is able to plot the modelled properties for all the compartments while a spreadsheet is sufficient to visualise the rest of the modelled results. In addition, a log-file is created by PRESSIM in order to monitor and examine the simulations.

Appendix C Estimation of overpressure

The measured/observed overpressures presented in this thesis are estimated by subtracting the hydrostatic pressure from the RFT (repeated formation test) measurements of the formation pressures. Thus there exist two sources of uncertainties; the RFT measurements and the estimation of the weight of the overlying pore water.

Figure C.1 shows the RFT measurements of the Brent Group in the 34/08-01 well in the North Viking Graben region. The large number of measurements and the relatively small variations of formation pressures at a given depth indicate that the uncertainties in the RFT pressures are low. Most of the plotted measurements are taken in formations that are characterised to have either very good permeability or good permeability. If the reservoir contains more tight rocks as shales there will not be a more or less unique trend in the formation pressure versus the depth as in Figure C.1. The uncertainty regarding the RFT measurements is of the order of 1 bar for the permeable reservoirs.

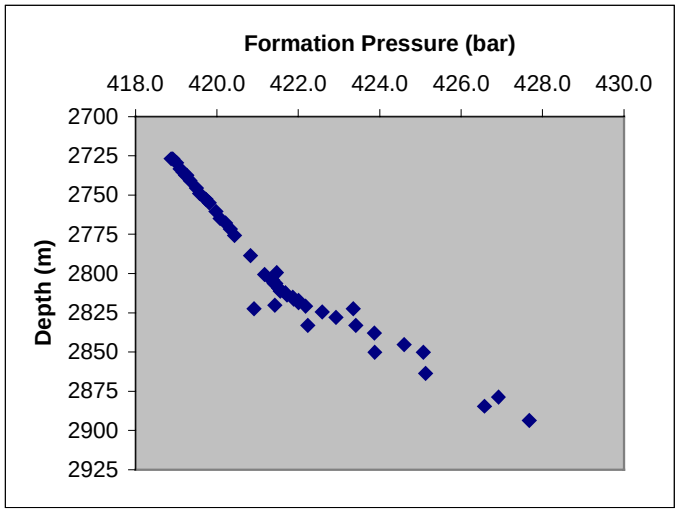

Figure C.1: RFT measurements from the Brent Group in the 34/08-01 well

The density of the formation water varies in a basin, mainly due to changes in the salinity. It is necessary to find representative mean value of the hydrostatic gradient in order to estimate the overpressure. Depending on the salinity the hydrostatic gradient will vary between 0.098 and 0.104 $kg \cdot m^{-2} \cdot s^{-2}$. If the hydrostatic gradient can be estimated within the accuracy of 0.005 $kg \cdot m^{-2} \cdot s^{-2}$ the calculation of the hydrostatic pressure at 4000 m includes an uncertainty of 20 bar. Conclusively, the overpressures estimated from the very accurate RFT measurements are infested with an uncertainty of the order of 10 bar.

Appendix D Mathematical deductions

Appendix D.1 Effective drainage depths

This appendix shows the way of thinking and deductions of the effective drainage depths listed in Table 5.4. Figure D.1 illustrates the six different sealing categories where the position of the top and mean depths of the pressure compartments relative to the modelled accumulating and sealing depths decides the effective drainage depth.

Practically, all pressure compartments are thinner than the accumulating zone. This means that the compartments follow the sequence of sealing categories 1-2-3-5-6 outlined in Figure D.1. However, to avoid this unlikely error the sequence 1-2-4-5-6 is included in the PRESSIM simulator. Two principles are followed suggesting an effective drainage depth for the six different categories. Firstly, the sealing depth shall be representative compared to the top- and mean depths of the pressure compartment. Secondly, the effective sealing depth shall never increase when a pressure compartment subside from one sealing category to the next as outlined in Figure D.1.

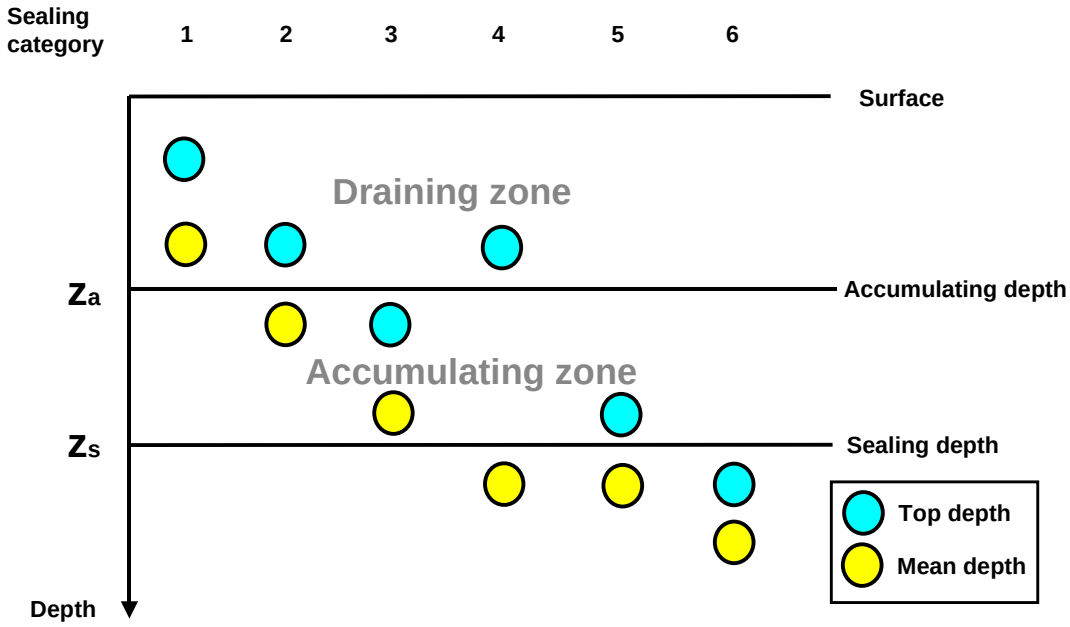

Figure D.1: Schematic outline of the six conditions between top- and mean depths and the accumulating zone.

The categories 1 and 6 are the two simplest instances. If both the top- and mean depths are less than the accumulating depth, no overpressure will be accumulated and the sealing depth can be defined to equal the accumulating depth (D.1). Similarly, if both the top- and mean depths are larger than the sealing depth all the flux into the cell will be accumulated and the drainage depth can be defined to be equal to the sealing depth (D.2).

$$z_{eff,1} = z_a \tag{D.1}$$

$$z_{eff,6} = z_s \tag{D.2}$$

If both the top- and mean depths are located within the accumulating zone, the mean of these to depths is used as the draining depth (D.3).

$$z_{eff,3} = \frac{z_t + \bar{z}}{2} \tag{D.3}$$

If the upper parts of the compartment lie above the accumulating depth and the main parts within the accumulating zone (category 2 in Figure D.1), the accumulating depth is probably representative for the vertical sealing properties of the cell. To account for the parts within the accumulating zone the half of the difference between the mean- and accumulating depth is added and then weighted with the fraction $\left(\frac{\bar{z} - z_a}{\bar{z} - z_t}\right)$ as outlined in (D.4).

$$z_{eff,2} = z_a + \left(\frac{\bar{z} - z_a}{2}\right)\left(\frac{\bar{z} - z_a}{\bar{z} - z_t}\right) \tag{D.4}$$

The effective sealing depth of the compartment in category 5 is defined in the same manner as Equation (D.4). The sealing depth is chosen to be the principal drainage depth because the main parts of the compartments lie below the sealing depth. Half the difference between sealing- and top depth weighted with the fraction $\left(\frac{z_s - z_t}{\bar{z} - z_t}\right)$ is subtracted to account for the parts located in the accumulating zone as shown in (D.5).

$$z_{eff,5} = z_s - \left(\frac{z_s - z_t}{2}\right)\left(\frac{z_s - z_t}{\bar{z} - z_t}\right) \tag{D.5}$$

If a pressure compartment is extremely thick (i. e. $(\bar{z} - z_t) > (z_s - z_a)$), the subsidence will follow the category order 2-4-5 in Figure D.1. To ensure that the effective draining depth of this possible, although unlikely, sequence is monotonously increasing during subsidence the effective depth is define to gradually change from $z_{eff,2}(\bar{z} = z_s)$ to $z_{eff,5}(z_t = z_a)$. The mathematical expression for this case is written in (D.6).

$$z_{eff,4} = \frac{\bar{z} - z_s}{\bar{z} - z_a + z_s - z_t} \cdot z_{eff,2}(\bar{z} = z_a) + \frac{z_a - z_t}{\bar{z} - z_a + z_s - z_t} \cdot z_{eff,5}(z_t = z_s) \quad \text{(D.6)}$$

Appendix D.2 Estimating shale permeabilities from accumulation efficiency

The deduction and the assumptions made to derive the shale permeability (5.5) from the simplified vertical flow model (5.4) are presented in this appendix. The Darcy flow out of a pressure compartment is given by (D.7). $\tilde{A}$ denotes the area of the pressure compartment and ΔL the length from the top of the reservoir to the top of the accumulating zone. The potential inducing the Darcy flow, ΔP, equals the modelled overpressure within the pressure compartment because there is hydrostatic conditions at the top of the accumulating zone.

$$\frac{\Delta V}{\Delta t} = \frac{\tilde{A}k}{\mu} \cdot \frac{\Delta P}{\Delta L} \quad \text{(D.7)}$$

The compressibility of the formation water is given by (D.8). Note that $\Delta\tilde{V}$ and $\Delta\tilde{P}$ denotes changes in pore volume and pressure, respectively, within the pressure compartments, while ΔV and ΔP in (D.7) relate to the flux out of the compartments.

$$\tilde{c} = \frac{1}{\tilde{V}} \cdot \frac{\Delta\tilde{V}}{\Delta\tilde{P}} \quad \text{(D.8)}$$

The model introduced in section 5.1 estimating sealing efficiency can be written as equation (D.9) where ΔV denotes the part of the incoming water leaking while $\Delta\tilde{V}$ is the part remaining in the pressure compartments.

$$\Delta V = \frac{(1 - f_A)}{f_A} \Delta\tilde{V} \quad \text{(D.9)}$$

The formation water that vertically escapes from the pressure compartments has to flow through the overlying low-permeable shales from the depth *z* to the accumulating depth z_A. Equation (5.4) can be reorganised to denote this thickness using known variables as shown in (D.10).

$$\Delta L = z - z_a = (z_s - z_a)\, f_A^{1/A} \tag{D.10}$$

Substituting (D.10) and (D.9) into (D.7) yields (D.11).

$$\frac{(1-f_A)}{f_A}\Delta\tilde{V} = \frac{\tilde{A}k}{\mu}\cdot\frac{P(z)-P(z_a)}{(z_s-z_a)\, f_A^{1/A}}\Delta t \tag{D.11}$$

The overpressure at the accumulating depth $P(z_a)$ equals zero by definition because all excess pressure is drained at the top of the accumulating zone. $P(z)$ denotes the overpressure in the pressure compartments, $\tilde{P}$. Reorganising (D.11), substituting (D.8) and incrementing the time and space variables result in the integrable expression (D.12).

$$(1-f_A)\left(f_A\right)^{\frac{1-A}{A}}\tilde{c}\tilde{V}d\tilde{P} = \frac{\tilde{A}k}{\mu}\cdot\frac{P}{(z_s-z_a)}dt \tag{D.12}$$

This differential equation is separable on the pressure dissipation time scale (i.e. the variables can be regarded as constant within the intervals of integration). Integrating from time t_1 to t_2 including the resulting pressure increase from P_1 to P_2, applying $\tilde{V} = h\tilde{A}\phi$ and solving for the permeability *k* Equation (D.13) is achieved. The pressure P can be integrated with respect to the differential $d\tilde{P}$ because $dP = d\tilde{P}$.

$$k = \frac{(1-f_A)\left(f_A\right)^{\frac{1-A}{A}}\tilde{c}h\phi\mu\left(z_s-z_a\right)\left(\ln p_2 - \ln p_1\right)}{t_2 - t_1} \tag{D.13}$$

It is important to point out that the permeability estimate (D.13) is not an exact deduced permeability that without more ado can be used in Darcy flow calculations. The assumption (D.9) is made to establish a link between a low permeable sealing layer and the sealing efficiency introduced in chapter 5. Equation (D.13) is used to verify that the corresponding shale permeabilities are not far off the expected values for shales that are sealing on a geologic time scale. The estimated permeabilities are not used in fluid flow calculations performed by the PRESSIM simulator.

Appendix D.3 Shale compaction and pressure generation

The difference between the two porosity-depth curves (5.14) and (5.15) is assumed to flow out of the shales into the sands if no overpressure retards this process. Thus at depth *z* the maximum amount of shale induced formation water is given by (D.14). Most of this water will never contribute to pressure build-up because nothing is accumulated in the reservoirs above the accumulating zone (Figure 5.4) and only parts of the volume within the accumulating zone. Differentiating (D.14) with respect to *z* the continuous shale compaction contribution during subsidence (D.15) is given and clearly illustrates the deduction of (5.16)

$$V(z) = 2\gamma\tilde{A}\left[\phi_p(z) - \phi_h(z)\right] \tag{D.14}$$

$$dV = 2\gamma\tilde{A}\left[\phi_p'(z) - \phi_h'(z)\right]dz \tag{D.15}$$

The increase in overpressure is calculated using the compressibility definition (5.7) multiplied with the stress dependency factor (5.17) as outlined in (D.16). Reorganising and integrating (D.16) from the depth z_0 to z_1 results in (D.17).

$$dP = \frac{dV}{\tilde{c}V}\cdot f_\sigma = \frac{2\gamma\left[\phi_p'(z) - \phi_h'(z)\right]}{\tilde{c}h\phi}\cdot\left(\frac{P_L - P_H - P}{P_L - P_H}\right)dz \tag{D.16}$$

$$\int_{P_0}^{P_1}\frac{dP}{P_L - P_H - P} = \frac{2\gamma}{\tilde{c}h\phi(P_L - P_H)}\int_{z_0}^{z_1}\left[\phi_p'(z) - \phi_h'(z)\right]dz \tag{D.17}$$

Carrying out the integration and solving the expression with respect to P_1 results in the expression (D.18), which is identical to the increase in overpressure given by Equation (5.18).

$$\begin{aligned} P_1 &= (P_L - P_H) - (P_L - P_H - P_0)e^{-\chi} \\ \chi &= \frac{2\gamma}{\tilde{c}h\phi(P_L - P_H)}\left[\left(\phi_p(z_1) - \phi_h(z_1)\right) - \left(\phi_p(z_0) - \phi_h(z_0)\right)\right] \end{aligned} \tag{D.18}$$